THE UNIVERSITY of EDINBURGH

Title	Sizes of HII regions in external galaxies
Author	Coulson, Iain M.
Qualification	PhD
Year	1980

Thesis scanned from best copy available: may contain faint or blurred text, and/or cropped or missing pages.

Digitisation Notes:

- Pag.64 missing from original.

THE SIZES OF HII REGIONS

IN EXTERNAL GALAXIES

Iain M. Coulson

Ph.D.
University of Edinburgh
1980

DECLARATION

Unless otherwise stated or referenced,
the work in this thesis is my own.

Iain M. Coulson.

ABSTRACT

Calibrated photographs in the light of Hα and [NII] have been obtained for ten southern spiral galaxies, primary amongst them being M83 (NGC 5236) for which there are six plates, four from the United Kingdom 48" Schmidt Telescope (UKST) and two from the Anglo-Australian Telescope (AAT). The HII regions in these galaxies are identified and measured with the automatic plate measuring machine, COSMOS, at the Royal Observatory, Edinburgh.

The sizes of the HII regions are determined from the measured profiles suitably deconvolved by the instrumental profile as given by the stellar intensity profiles. The dimensions obtained are a function of the assumed intrinsic intensity profiles of the HII regions. The assumption that these are gaussians leads to a systematic difference in the determined sizes and could systematically affect the value of H_o, the Hubble Constant.

The correct choice of intrinsic intensity profile is defined as that which removes the systematic effect. For M83 this is found to be an exponential decay profile. The dimensions of the HII regions are derived and the resulting size distribution is found to be well fit by a Poisson function, the parameterisation of which is proposed as a distance indicator. It is shown to be free from effects due to selection by brightness and represents the 'giant' HII regions that define the spiral arms.

Other galaxies studied also have HII region size distributions that could be fit by Poisson functions.

A comparison of the HII region size distributions of M33 and M83 gives a distance for the latter of about 4 Mpc and an estimate of H_0 of 80 km s^{-1} Mpc^{-1}.

CONTENTS

CHAPTER 1

INTRODUCTION

In 1929 Hubble discovered that galaxies were in general receding from us at velocities proportional to their distances from us. The search for the value of this constant of proportionality, the Hubble Constant, H_o, has been one of the most stimulating goals of astronomy, encompassing many varied astronomical disciplines, including, at a quite critical stage, the sizes of HII regions.

It is accepted that only the velocities and distances of galaxies free from local disturbances i.e. those partaking of the "pure Hubble flow", should be used in the calculation of H_o. Their velocities are obtained from the redshifts of lines in their spectra (Humason *et al.* 1956). Their distances are derived by a step by step procedure (Sandage and Tammann 1974a, b, c, d, 1975a, b, van den Bergh 1975a, de Vaucouleurs 1978a, b, c, d) based on the Principle of the Uniformity of Nature (Hubble 1936) (see Appendix A), according to which objects of apparently similar nature are assumed similar in all other aspects. In particular, differences in apparent brightness or size amongst a group of objects assumed to have similar brightnesses or sizes, may be attributed to differences in their distances from us. Knowledge of one distance leads to knowledge of the others.

The problems and uncertainties inherent in the use of the Principle are outlined in Appendix A.

Until recently, measurements of the sizes of HII regions in external galaxies have been made from photographic plates, by eye, in a fashion similar to that described here in Ch. 4-3. Such "eyeball" work has been done here also, for comparative purposes. However, such techniques are relatively primitive in comparison with other steps in the hierarchy of steps towards determining H_o, so more objective measurements were initiated that involved the use of plate measuring machines (Hodge 1976a, Kennicutt 1979a, b).

In this thesis I have tried to make more precise the definition of 'diameter' as applied to HII regions. Although the sizes of HII regions may be intuitively obvious when one studies photographs of nearby galactic examples, or may be exceedingly well-defined in theoretical modelling, from photographic material they must ultimately be derived from the light intensity profiles of the images. Such profiles of HII regions in distant galaxies are particularly subject to seeing and other smearing effects that have been examined and quantified here. The diameters thus derived should prove to be more useful in producing a distance indicator than those derived from 'eyeball' measurements.

While almost all previous workers concerned with HII regions in galaxies beyond the Local Group have restricted their measurements to the largest few in any galaxy, I have obtained dimensions for all identified HII

regions in the galaxies studied in order to derive size
distributions for each galaxy. Such distributions exist
for members of the Local Group and a comparison via the
parameters of such distributions should be less prone
to the statistical flukes that may influence the current-
ly popular mean-of-the-largest-three statistic.

For this work, the COSMOS automatic plate measur-
ing machine was used to measure photographic material ob-
tained with the UK 48" Schmidt and Anglo-Australian 3.9
metre reflecting telescopes. All three machines are
examples of frontier technology. With such powerful as-
sistance it is hoped to be able to put the determination
of the sizes of HII regions on the objective footing re-
quired of such a crucial step in the process of deriving
H_o.

CHAPTER 2

THE PRIMARY DISTANCE INDICATORS

The sizes of HII regions are used as distance in-
dicators at a particularly crucial step in the hierarchy
of calculations that leads eventually to H_o. Preceding
their use are the basic trigonometrical calculations that
define the scale of our immediate neighbourhood in space,
the calculations of the distances of the nearest stars
in our own Galaxy, and the calibrations of their various
properties that are used to determine the distances of
the nearest galaxies. These steps are to be described
here in Chapter 2.

HII regions, together with other secondary indi-
cators, are used to extend the distance scale from the
nearby galaxies to those further afield where galaxian
parameters can be calibrated and from where the distance
scale can be extended to the limits of the observable
Universe.

Chapter 2, then, illustrates the foundations upon
which rest the HII region size calibration and the rest
of the distance scale.

2.1   *Historical Measurements*

By observing the shadow of the Earth during a
lunar eclipse Aristarchus of Samos (310-233 B.C.) was
able to express the distances to the Sun and Moon in
terms of the Earth's radius. Later, Eratosthenes (276-

195 B.C.) determined the circumference of the Earth with
some simple geometry by observing the apparent position
of the Sun from two places at, essentially, the same time.
And he got a value not too different from that used today.
Thus the relative distances determined by Aristarchus
could be converted to absolute ones and the scaling of our
particular corner of the Universe was complete.

It was not until the heliocentric solar system
theories of Copernicus (1473-1543) and Kepler (1571-1647),
however, that distances to the other planets were deter-
mined. Their other properties, principally their masses,
became calculable from the laws of motion of Galileo (1564-
1642) and Newton (1642-1727).

Using the Earth's orbit about the Sun as a base-
line, distances to the nearer stars can be calculated by
trigonometrical parallax, though for more distant stars,
the techniques become more statistical, relying often on
an assumption that stars of similar spectral properties,
say, have similar luminosities - an application of the
Principle of the Uniformity of Nature (Appendix A).

There is one (hypothetical?) circumstance that
allows the distance to a group of stars to be determined
even if they lie beyond the domain of normal trigonometri-
cal methods; that is when the stars in a cluster can be
assumed to be moving uniformly through space. The Hyades
open cluster is assumed to behave like this and the Con-
vergent Point method has been applied to it. This method
is described shortly. Traditionally it is this determina-
tion that forms the basis of the hierarchy of steps leading

to H_o.

2.2 *The Distance to the Hyades*

The stars in a cluster moving uniformly through space will appear to converge upon a single point in the sky, called the convergent point. Measurements of proper motions and radial velocities of the member stars lead to a distance for the cluster (see for instance Wayman *et al.* 1965).

This method has been applied most often to the Hyades. Van Bueren (1952) obtained a distance modulus of 3.03 ± 0.06, Wayman *et al.* (1965) obtained 3.05 ± 0.09, Hodge and Wallersten (1966) 3.42 ± 10%, Corbin *et al.* (1975) 3.19 ± 0.04, Hanson (1975) 3.42 ± 0.19, Murray and Harvey (1976) 3.04 - 3.07. Van Altena (1974) reviewed the work till that time and together with a series of parallax calculations derived a distance modulus of 3.21 ± 0.09. The need for so many calculations of this distance merely underlines the uncertainties involved; like those of membership of the group, and the position, if not the very existence, of the convergent point itself (Clube 1974).

Independent determinations of the distance to the Hyades, like those of van Altena above, and of Anthony-Twarog and Demargue (1977), who observed binary stars in the cluster, seem to be necessary, and seem also to support the trend towards the higher value for the modulus, that is of about 3.3.

Clearly there are uncertainties even in this, the first step in the hierarchy, and an independent cluster

distance would be useful. The Sco-Cen association is the next group of stars most suitable for this method, but the uncertainties are equally large (Bertiau 1958).

2.3   *Zero Age Main Sequence (ZAMS) Fitting*

The ZAMS is a line in the H-R, or magnitude-colour, diagram representing the positions of stars of different masses that have completed their initial collapse, but have not yet started hydrogen burning (Blaauw 1963). Assuming, in accordance with the Principle of the Uniformity of Nature, that the ZAMS for all clusters younger than the Hyades (aged 10^9 years) are identical, and this means unaffected by differences in chemical composition, then sliding their M_V, B-V plots parallel to the m_V axis until they match the plot for the Hyades along the ZAMS gives their distance moduli with respect to the Hyades (Blaauw *et op. cit.*, Johnson *et al.* 1961). In this way also the ZAMS line is extended beyond that part of the diagram covered by the ZAMS of the Hyades.

Differences in chemical composition, however, may vary the position of the ZAMS in the M_V, B-V frame by as much as $0\overset{m}{.}24$ (e.g. Barry 1974) and this difference would appear as a difference in distance on application of the ZAMS fitting method.

In principle, however, the distances to all such clusters may be determined, and in them are the bright and/or variable stars that can then become calibrators of their types. Such stars, like cepheids and RR Lyrae

stars, to mention two of the variable types, are then ob-
served in more distant systems and compared with the cali-
brators in order to determine the distances to those sys-
tems. The uses of bright and variable stars in this rôle
are described in the following sections.

2.4   *Cepheids*

Important amongst distance scale indicators are
these orange supergiants.   With absolute magnitudes as
bright as -9 in V, these stars may be detected at great
distances.   What makes them useful as distance indicators
is that their luminosities (L) and periods of variability
(P) obey a fairly well defined relationship.   This was
first noted by Leavitt (1908, 1912) who observed these
stars in the Magellanic Clouds, the distance to which,
although unknown, reduces the apparent brightnesses of
all stars therein by the same amount, so that what is ob-
served there is a P-m_V relationship.

Calibration to a P-M_V relationship was first at-
tempted by Hertzsprung (1913) from observations of galac-
tic cepheids.   This assumes, of course, that galactic
and Magellanic cepheids are of a similar nature, and yet
there is an abundance of data to suggest that this is not
the case (see Apppendix A);   Magellanic cepheids being
in general bluer than their galactic counterparts, for in-
stance.

A significant fraction of the residual scatter
in the P-L relations derived to date must be intrinsic,

and suggests the necessity of a third parameter. (Martin
et al. 1979) - usually colour, as was suggested by the
theoretical work of Sandage (1972). Martin *et al.* (1979)
determine a coefficient for the colour term in their
P-L-C relation for the LMC that is close to that required
by theoretical studies.

Calibration of the P-L-C relation by galactic
cepheids is also discussed by Martin *et al.* (1979) and
they present

$$M_{<v>} = -3.80 \log P + 2.70(<B_o> - <V_o>) - 2.39 \quad (2.1)$$

as their global solution.

Distance moduli to members of the Local Group of
galaxies may then be obtained by application of such an
equation to the cepheids observed therein (Baade and Swope
1963, Gascoigne 1969, Kayser 1967, Pel 1980 and others).

The error induced in $M_{<v>}$ by using galactic cali-
brators that have a higher average metallicity than the
stars in the LMC is calculated by Martin *et al.* (1979)
to be about 0.11 mag, in the sense that the metal poor
stars are fainter. The SMC is thought to be rather more
metal deficient than the LMC, compared to solar values,
and the corresponding correction will be proportionately
larger for the SMC. Metallicity differences between the
cepheids of other Local Group galaxies and the 'standards'
used in setting up the above relation must be quantified
if the distances to these galaxies are to emerge accurate-
ly from a comparison of the P-L-C relations.

In theory, this applies to more distant galaxies also, though in practice there are no galaxies beyond the Local Group wherein cepheids most comparable with those used in formulating equation (2.1) can be observed throughout their light cycle. The M81 (NGC 3031) group, which may encompass the NGC 2403 and NGC 4236 associations (see de Vaucouleurs 1978d), was considered by Tammann and Sandage (1968) to be within the domain of applicability of the cepheid distance technique. They assumed the whole group to be at the same distance and derived this distance from cepheid observations in NGC 2403.

In NGC 2403, however, only the longest period cepheids are detectable at all phases while medium period cepheids ($P \sim 20^d$) are detectable only near maximum light. Tammann and Sandage derived the distance by a comparison of the upper envelopes of the P-L relations of the long period cepheids ($P > 40^d$) at maximum light. De Vaucouleurs (1978d) claims that this will have "at best a tenuous connection with the P-L relation at mean light for the calibrating open cluster cepheids ($P < 20^d$)".

A recalculation of the NGC 2403 cepheid data by Madore (1976) gives a distance modulus of 26.7 compared with 27.6 as derived by Tammann and Sandage (1968).

De Vaucouleurs (1978d) chooses to obtain the distance to the M81 group from secondary indicators calibrated in the Local Group. By developing and using several such secondary indicators (which do not include the sizes of "normal" HII regions) he follows the spread-the-risks philosophy (Appendix A) to avoid biasing the ensuing

distance scale with the peculiarities of the Local Group members.

2.5   *RR Lyrae Stars*

The early determinations of the mean absolute magnitudes of these short period "cepheids" (Mineur 1944) gave $M_V = 0^m.5$, while later results have tended to make them fainter ($0^m.6$ - Woolley *et al.* 1965, van Herk 1965, Sandage 1970; $1^m.3$ - Clube and Jones 1971; $0^m.7 - 0^m.8$ - Hemenway 1975; $1^m.0$ - Clube and Dawe 1980b).

The techniques of statistical parallax applied to field stars, as described by Clube and Dawe (1980a), avoid the membership problems associated with cluster work but must encounter homogeneity problems in samples whose members have highly various metallicities and galactic orbital parameters (e.g. Kukarkin 1975).

RR Lyraes are much less luminous than cepheids and are more restricted therefore in their domain of applicability as distance indicators. As Madore (1976) points out, the ideal of using many independent distance indicators has not been realised, and cepheids are still the most powerful tool in determining the distances to nearby galaxies.

However, some of the other primary distance indicators are still worth a mention.

2.6   *Novae*

Parameters have been found from the light curves of novae that depend upon their absolute magnitudes at

maximum light.   McLaughlin (1945) found a correlation

between t_3, the time taken for a nova to fall to 3 magni-

tudes below maximum, and the absolute magnitude at maxi-

mum.   Obviously the nova must be caught soon after maxi-

mum to apply the technique.   Van den Bergh (1977) finds

that the best fit to the m_{pg}(max), t_2 data for novae in

M31 (Arp 1956, Rosino 1964, 1973) still leaves a dispersion

in the magnitude of $0^m.4$.

Buscome and de Vaucouleurs (1955) found that novae

have a fixed absolute magnitude 15 days after maximum and

revised calculations by de Vaucouleurs (1978a) give

$$<M_{15}(pg)> = - 5^m.5 \pm 0^m.18.$$

Calibration of both methods is via observations

of galactic novae, now numbering 15, for which expansion

parallaxes have been calculated.

2.7   *Bright Stars*

The advantage of using the brightest stars is an

increase of the signal to noise ratio over comparable ob-

servations of other stars, while the main problems are

still those of sampling, where contamination by foreground

stars, clusters and HII regions may occur.   Again there

is a problem with metallicity effects: the brightest

stars in a highly evolved metal rich galaxy may be quite

different from corresponding stars in metal poor galaxies.

(Arp 1955, Sandage and Wallerstein 1960).

Sandage and Tammann (1974b) found that the abso-

lute magnitude of the brightest blue star in a galaxy is

correlated with that of the galaxy itself:

$$M_B^* = 0.315 \ M_{pg}^{gal} - 3\overset{m}{.}48 \pm 0\overset{m}{.}52.$$

The slope of this relation is close to that of the "distance effect" line, of slope 0.2, and persuaded Sandage and Tammann to derive a similar relation between M_B^* and L_c, the luminosity class of the galaxy, instead. de Vaucouleurs (1978c) deemed this move unnecessary since $M_B^* - M_{pg}^{gal}$ or $m_B^* - m_{pg}^{gal}$ is an observable quantity and leads to a direct solution for the distance.

The brightest red stars appear to have an upper limit ($M_V = - 7\overset{m}{.}9$) to their brightnesses whether variable or not (Tamman and Sandage 1968, Sandage and Tammann 1974b, Humphreys 1979), which in principle makes them useful distance indicators.

2.8   *Summary*

The primary distance indicators listed above, and some not listed, allow the distances to the nearest galaxies to be measured. Table 2.1 presents some distances as adopted by various workers.

If the average scatter in these results is intrinsic, an error in H_o of 12% may be expected.

Table 2.1

Adopted distances (in kpc) of Local Group galaxies

Galaxy	deV[1]	S&T[2]	vdB[3]	$\bar{d}$o
LMC	45.9	52.2	52.5	50.2 ± 3.7
SMC	53.0	71.4	60.3	61.6 ± 9.3
M31	652	667	724	681 ± 38
M33	724	817	692	744 ± 65
N6822	557	616	794	656 ± 123
IC1613	637	769	794:	721 ± 78

1   de Vaucouleurs 1978b

2   Sandage and Tammann 1971, 1974a

3   van den Bergh 1977

CHAPTER 3

HII REGIONS AS DISTANCE SCALE INDICATORS

The primary distance indicators allow us to determine the distance to nearby galaxies, but become unusable beyond a distance modulus of about 30 where even the brightest stars, variable or otherwise, are undetectable. To reach further out into the Universe requires the establishment of secondary distance indicators - including HII regions - whose properties must be calibrated within the Local Group and nearby galaxies.

This chapter will describe the ways in which HII regions have been used in the distance scale context, the "eyeball" measurements of the sizes of HII regions in external galaxies, and the recent advancements into machine measurements of these sizes.

3.1   *Sérsic*

In 1959 Sérsic postulated that the sizes of HII regions could be used as distance indicators and in 1960 measured the diameters of the largest HII regions in 65 galaxies in 11 groups from a uniform collection of blue plates. Assuming gaussian intensity profiles for the images of stars and nebulae, he reduced the measured nebular diameters, d_1 , by that of the stars, d_*, to give the corrected HII region diameters, d_o, thus:

$$d_o^2 = d_1^2 - d_*^2 \qquad\qquad (3.1)$$

The mean of the largest three nebulae in each galaxy, $<d_3>$, was seen to correlate with galaxy type, reaching a maximum of about 180 pc at the Sc⁻ type.

Sérsic (1979) later amended the formula for the instrumental diameter by introducing an additive constant to account for emulsion effects. The plate scale then becomes an important factor in the calculation of the corrected diameter since the angular sizes of objects will be overestimated by the measurement of their image sizes on small scale plates.

In the present work emulsion effects are examined very closely, and the availability of photographic plate material of quite different plate scales should illustrate the effect of plate scale upon angular size measurements.

3.2   *Sandage and Tammann*

In 1974, in the *Astrophysical Journal*, there began a series of papers by Sandage and Tammann (S & T) entitled "Steps toward the Hubble Constant" in which the complete hierarchy of the distance scale, from the Hyades to H_o, is examined (S & T 1974a, b, c, d, 1975a, b, 1976b). In their first paper they presented diameters of HII regions in the Local Group of galaxies and in the M81 group. Like Sérsic their measurements were by eye, but now they used photographs taken through red and Hα filters.

They introduced the concepts of 'core' and 'halo' to describe the structure they saw in HII regions, and measured both features on each image. They recognise,

however, that this "structure" was perhaps more a response of the eye and brain to steep gradients in plate density than to abrupt changes in the density profiles. While their halo measures of regions in the Magellanic Clouds compare well (chapter 3.6 here) with those of Henize (1956) and Davies *et al.* (1976), the means of core and halo do not, and de Vaucouleurs (1977a) rejects this mean as a metric length and therefore as a distance indicator.

'Cores' proved rather elusive to this author during the eyeball measurements conducted here, as they have to others (Kennicutt 1979a). The machine measurements, which produce intensity profiles, and which will be described fully later, show no sign of core/halo structure, although Hodge (1976) has presented one intensity profile that does show a shoulder and is well represented by its core and halo dimensions. In general, though, he found the assigned 'eyeball' dimensions unrepresentative of the intensity structure.

Sandage and Tammann (1974a) showed how their measured dimensions were essentially independent of exposure and therefore of the photographic technique and, hence, that the largest regions were radiation bounded (Strömgren 1939). They corrected their data for other systematic effects including differences in filter and in mode - direct or via an image tube - but made no corrections for the seeing, an omission for which they have been se-verely criticized (de Vaucouleurs 1977a). Accounting fully for the seeing is shown herein to be a non-trivial task, and despite Sandage and Tammann's justifiable comments

that the core-halo dimensions of the HII regions are domi-
nated by the relatively large halo measurements, for which
the seeing corrections are generally small, such measure-
ments in a more far-reaching scheme will need to be fully
seeing corrected in order to avoid systematic errors.
Yet there is no indication that they changed their approach
when analysing similar data for more distant galaxies
(S & T IV, 1974d).

Sandage and Tammann converted the measured angular
dimensions to linear dimensions using Cepheid distances
(S & T 1971, T & S 1968) - this reliance upon distances
derived from only one set of primary indicators has also
been the subject of much debate and will not be further
discussed here. A summary of the stances taken by the
two opposing schools is given in Appendix A.

Sandage and Tammann then aim (S & T I, 1974a) to
derive a relationship between the mean of the largest
three HII regions in a galaxy, $<D_3>$, and the absolute mag-
nitudes of the parent galaxies, M_{gal}. In order to avoid
an extrapolation of the relation to the bright ScI class
of galaxies they made a particular effort (S & T III,
1974c) to determine the distance to the ScI galaxy M101
(NGC 5457). The entire M101 group then became part of
the calibrating group, alongside the galaxies from the
Local and M81 groups. However, the normality of M101 as
an ScI galaxy and the possibility that it is a foreground
object to "its group" are problems that still plague the
use of M101 in this way (Holmberg 1964, S & T III, de
Vaucouleurs 1978d, Jaakkola and le Denmat 1976, Kennicutt

1979b, c). Sandage and Tammann have also been criticized by de Vaucouleurs (1977a) for apparent circularity of argument in that their distance to M101 was determined (S & T III) by methods that included the use of HII region diameters, although their result is unaffected by the exclusion of the HII region-diameter contribution.

Sandage and Tammann plot their data in the Mpg, log $<D_H, D_c>_3$ plane and derive the best fitting straight line by a 'least squares' approach. (Since the distances to the calibrating galaxies are assumed well known, their absolute magnitudes are too, so all the errors in this plot are assumed to lie with $<D>$ and therefore a 'least squares' approach is justifiable). Their data is replotted in Fig. 3.1 here, and a comparison with their Fig. 9 (S & T I) will reveal a couple of inexplicable differences.

Using unit weight for each datum in this D-M plane, best fit least squares solutions to various subsets of the data are:

a)   for just the local and M81 groups (11 galaxies)

$$\log D = (-0.151 \pm 0.022)M - 0.366 \pm 0.097 \qquad (3.2)$$

b)   for the local, M81 and M101 groups without M101

        (16 galaxies)

$$\log D = (-0.125 \pm 0.018)M + 0.058 \pm 0.105 \qquad (3.3)$$

c)   for the local, M81 and M101 groups (17 galaxies)

$$\log D = (-0.131 \pm 0.015)M - 0.042 \pm 0.102 \qquad (3.4)$$

where $D \equiv <D_c, D_H>_3$ and $M \equiv M_{pg}^o$ (S & T I). There is no significant difference between these lines as can be seen from Fig. 3.1.
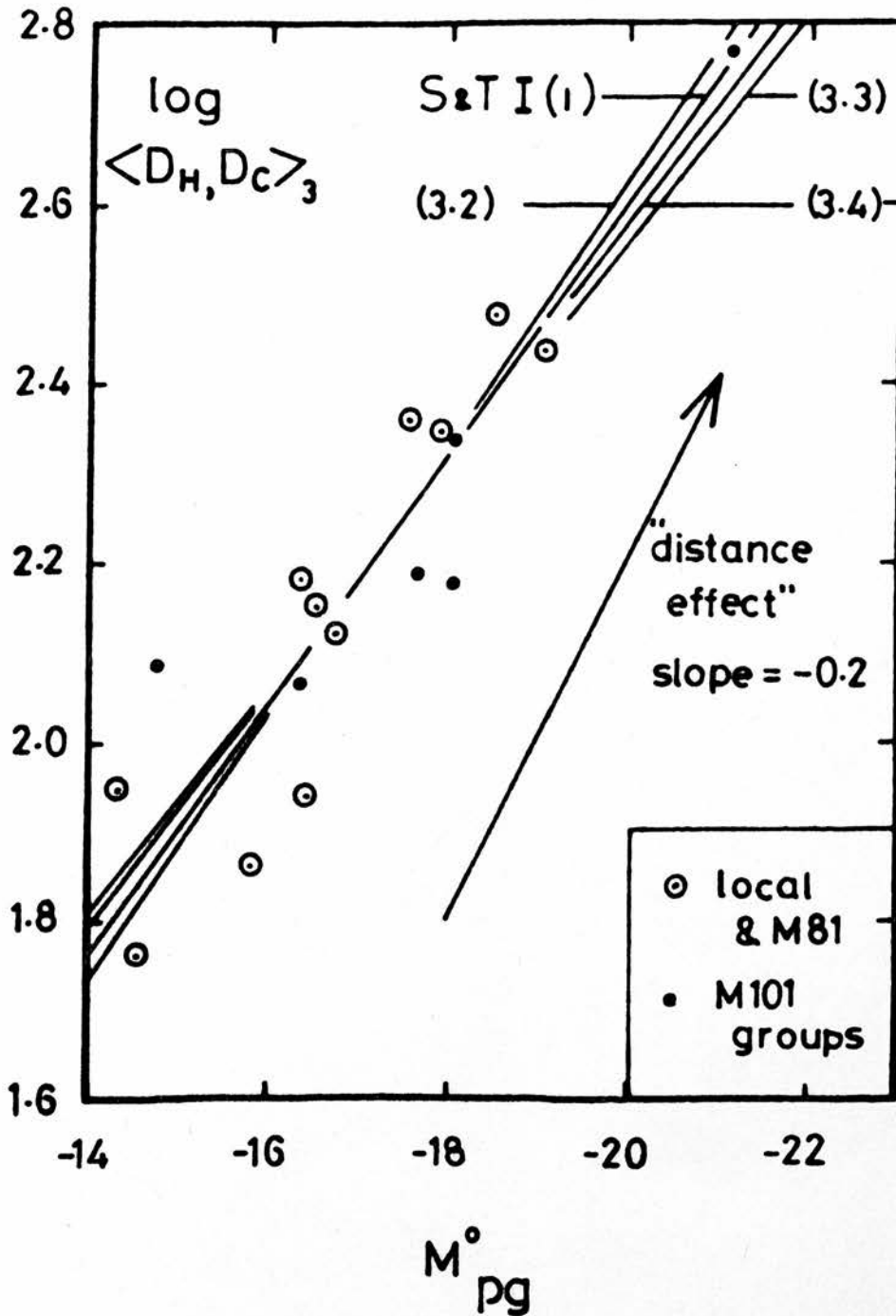
Figure 3.1. The D-M calibration. The relationship between the mean core-halo diameters (pc) of the largest three HII regions in a galaxy and the absolute magnitude of the galaxy. The lines are the best fit straight lines as numbered in the text.
Data from Sandage and Tammann (1974a).

Sandage and Tammann (1974a) presented their

equation (1)

$$\log D = -0.140 \, M - 0.202 \pm 0.09 \qquad (3.5)$$

as the equivalent to equation (3.4).

The slopes of these lines are close to -0.2, the slope of the "distance effect" line, which is also marked in Fig. 3.1. This line represents an hypothetical relation between D and M in which nearby dwarf and distant giant galaxies would appear to have HII regions of the same size and from which it is impossible to obtain iterative solutions for the distance. With slopes close to -0.2 in this diagram iterative solutions will not converge rapidly from the initial guesstimates.

The relations being iterated upon are

$$\log D = aM + b \qquad (3.6)$$

$$D = \alpha R \qquad (3.7)$$

and $\qquad M = m - 5 \log R + 5, \qquad (3.8)$

where α is the angular size of the HII region of linear size D, R is the distance to the galaxy, and M and m the galaxy's absolute and apparent magnitudes; a and b are constants. The direct solution for R is

$$\log R = \frac{b - \log \alpha + 5a + ma}{1 + 5a} \qquad (3.9)$$

which is degenerate if $\underline{a} = -0.2$.

The error in log R is

$$\Delta \log R = \frac{\Delta \log D}{1 + 5a}, \qquad (3.10)$$

as derived in Appendix B, and again shows that the technique becomes unusable as $\underline{a}$ approaches -0.2. With the

slope of equation (3.6) lying empirically between -0.125 and -0.151, as seen in equations (3.2) - (3.4), the error in log R may be expected to be 3 or 4 times as large as that in log D, and this implies an error in R of a factor of 2 or 3! This is somewhat larger than the 40% errors expected by van den Bergh (1980) from this part of the cosmic distance scale determination, and is what drove Sandage and Tammann (1974a) to search for another parameter to which to relate the HII region diameters.

An alternative would be to search for an improvement in the data quality - it is not just the closeness of the slope of the D-M relation to that of the distance effect line that makes the method inaccurate, but also the inherent inaccuracy in the values of D and M, in the distances to the calibrating galaxies, in the primary distance scale etc.. In fact, some improvement in the present scheme may be achieved by using $<D_H>_3$ instead of $<D_c,D_H>_3$ in the D-M relation. As will be described in ch. 3.6, the values of D_H derived by Sandage and Tammann (1974a) for HII regions in the Magellanic Clouds are in much better agreement with diameters derived from other sources than are their values of $<D_c,D_H>$. The lines corresponding to those described by equations (3.2), (3.3) and (3.4) are, respectively,

$$\log <D_H>_3 = (-0.128 \pm 0.021)M + 0.239 \pm 0.097 \quad (3.12)$$

$$\log <D_H>_3 = (-0.108 \pm 0.019)M + 0.575 \pm 0.101 \quad (3.13)$$

and $$\log <D_H>_3 = (-0.117 \pm 0.015)M + 0.419 \pm 0.100 \quad (3.14)$$

The slopes are clearly less close to that of the distance effect line than their core-halo counterparts, indicating $<D_H>_3$ to be more useful distance indicator than $<D_c,D_H>_3$, but equation (3.10) still indicates an error in R of $\sim70\%$.

The parameter chosen by Sandage and Tammann to fill the above role was van den Bergh's (1960) luminosity class, L_c, which may be assigned to a galaxy by morphological considerations alone. Numerations of the L_c scheme may well be subject to personal effect (Bottinelli and Gouguenheim 1976) although de Vaucouleurs (1979a) would strongly defend the numerations of both L_c and T (morphological type) since they have been shown reproducible by several persons (*op cit*) and have many astronomical precedents in cases where quantification has initially proven difficult.

Sandage and Tammann (1974a) derive finally their equation (7):

$$<D_H,D_c>_3 = -96.5\ L_c + 557 \tag{3.11}$$

which Bottinelli and Gouguenheim (1976) show to be incompatible with equation (3.5) and the (M,L_c) relation presented in S & T IV table 5.

De Vaucouleurs (1977a) has defined a luminosity index, $\Lambda = (T+L)/10$, which he shows to be more closely correlated with absolute magnitude than either T or L alone. But since these parameters are so closely tied to absolute magnitude (van den Bergh 1960, Sandage and Tammann 1974d, table 5) should any improvement over the

D-M relation be expected by replacing M by such a para-
meter?

3.3   De Vaucouleurs' HII Rings

Gum and de Vaucouleurs (1953) were the first to
use the diameters of ring-type HII regions to determine
the distance to galaxies. From their observations in
the Local Group they noted that the largest ring in a
galaxy, irrespective of galaxy type, was about 85 pc in
diameter and that the second, third and fourth largest
were 0.9, 0.8 and 0.7 of this size.

De Vaucouleurs (1978c) later reformulated the
calibration thus:

$$\log D_1 = 1.35 - 0.05\ M_T^O$$

where D_1 is the size in parsecs of the largest HII ring,
and M_T^O is the absolute magnitude of the parent galaxy.

The advantages of using ring type HII regions
are that their measurement is unambiguous and may be
possible on any type of plate. The main drawback to their
use is that they are not very bright in general (Boulesteix
et al. 1974) and may not appear in all galaxies. De
Vaucouleurs (1979c) has measured ring type HII regions in
M83, the largest of which is placed 2!1E and 2!2N of the
nucleus, yet it is not to be seen on the Hα plates used
in this work.

Boulesteix *et al.* (1974) suggest that these
rings are late stages in the evolution of expanding ionized
regions.

3.4   Other Properties of HII Regions

Other properties of HII regions that may prove useful as distance indicators:

Brand and Zealey (1975) showed that large HII region complexes are often outlined by dust shells which are unambiguously measurable from plates of any type.

Melnick (1977, 1978) has described the correlation between the velocity dispersion in the H_α emission of giant HII regions with both their linear dimensions and the absolute magnitude of the parent galaxy. The correlations are very tight and promise to produce a very powerful distance indicator.

Balmer line fluxes are relatively easy to measure (Hodge 1976) although absorption corrections are uncertain enough to preclude their present use as distance indicators (Melnick 1979).

3.5   The Sizes of HII Regions in the Galaxy

Catalogues of galactic HII regions, including their angular dimensions, have been compiled by Gum (1955), Sharpless (1959), Campbell *et al.* (1960) and Georgelin and Georgelin (1970) amongst others, and a compilation of all these works has been produced by Marsalakova (1974).

Distance estimation for galactic HII regions is usually accomplished via the assumed luminosities of the O (and B) stars exciting the regions. Luminosity determination for O stars is still problematic (Conti 1975) although recent improvements have been achieved

(Walborn 1978) in deriving luminosity sensitive absorp-
tion line ratios.

The distances so derived enable the angular dia-
meters to be converted to linear ones. Murdin and Sharpless
(1968) and Georgelin (1971) present frequency distributions
of HII region diameters that decay roughly exponentially
with increasing size. Best fitting curves to these data
show an e-folding on a scale of 30 to 40 pcs. A more re-
cent presentation of the size distribution of HII regions
by Georgelin *et al.* (1979) is again approximately an ex-
ponential decay, and is best fit by such a curve with an
e-fold of 22 $\pm$ 1 pc with rms/abc = 0.12 (see chapter 3.6
for an explanation of the symbolism and error determina-
tion).

As will be seen later this value of the e-folding
parameter, de, is indicative of the Galaxy being more
akin to M31 than to M33 - the latest classification of
the Galaxy by de Vaucouleurs (1979d) is SAB(rs)bcII (M31
is classified b, and M33 cd).

3.6   *The Sizes of HII Regions in the Magellanic Clouds*

Henize (1956) has presented data on the sizes,
shapes and Hα-luminosities of 415 HII regions in the LMC
and 117 HII regions in the SMC. The size distributions
for all but those in his brightness class 1 are shown in
Figure 3.2. Both distributions show approximations to ex-
ponential decays; the data for the LMC are well fit by
an exponential with an e-folding diameter of 2.6 arc mins
≡ 38 pc at 50 kpc.
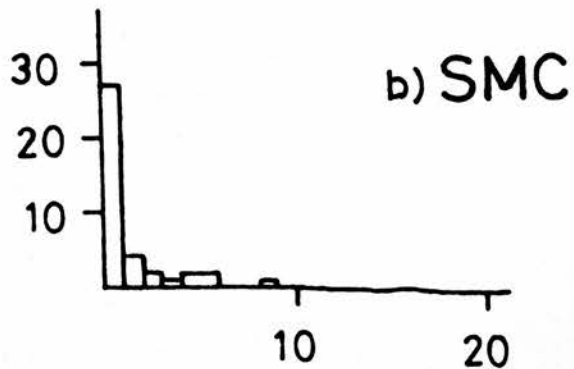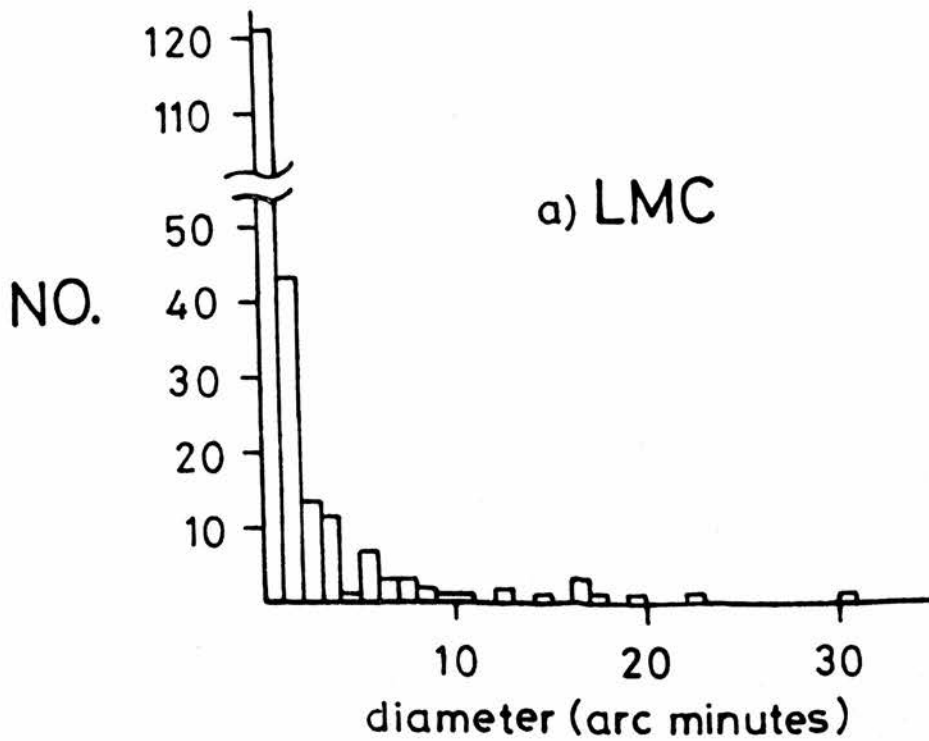
Figure 3.2.   The Sizes of HII Regions in the Magellanic Clouds.
Data from Henize (1956).
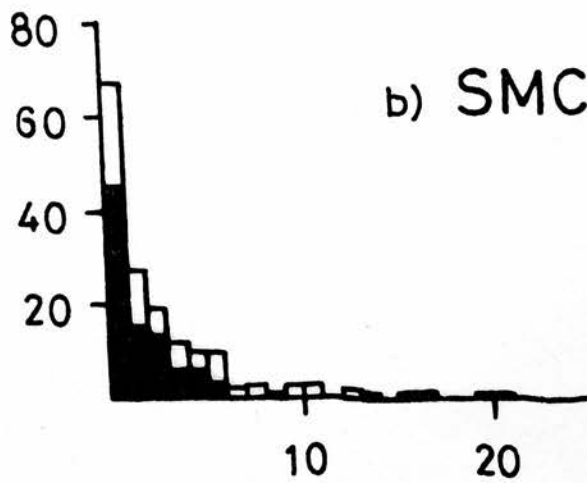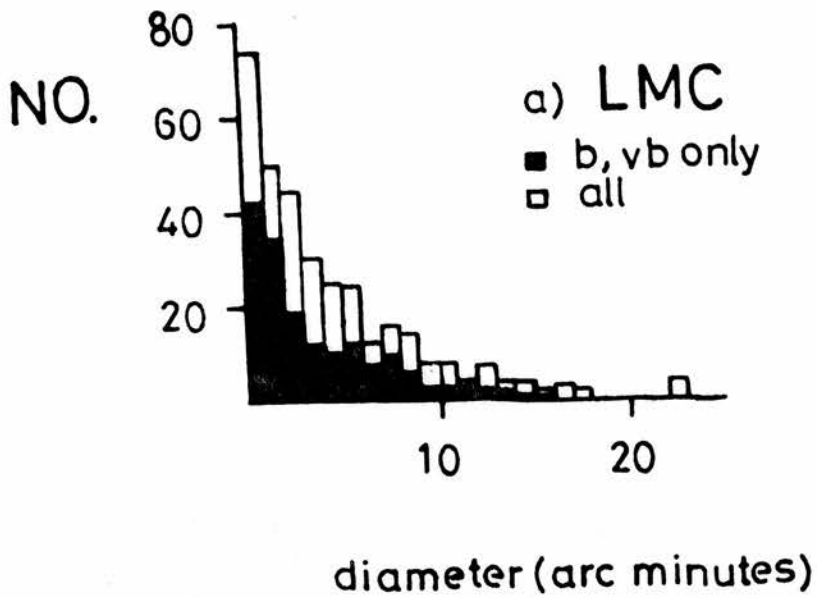
Figure 3.3. The Sizes of HII Regions in the Magellanic Clouds. Data from Davies *et al.* (1976).

Davies *et al.* (1976) have published excellent
Hα photographs of the Clouds and have given angular di-
mensions for the HII regions detected on them.   Their
data has been used to produce the size distributions
shown in Fig. 3.3, with a distinction being drawn between
the regions they classed 'bright' or 'very bright' and
the fainter ones.   Davies *et al.* seem to have detected
relatively fewer small regions (0 - 1 arc min) than did
Henize, but this may be explained by the telescope and
plate scale combination used (Arp and Bruekel 1973, ch.
5.5 here).   Again the distributions appear to behave like
exponential decays and curve fitting with such functions
was pursued.   The technique and nomenclature used here-
after and as mentioned in ch. 3.5 are as follows:

For a specified range of diameters an exponential
curve is fit to the data so as to minimise the sum of
the squares of the deviations of the observed data from
the curve.   The goodness of fit is given by the ratio of
this minimum valve (rms) to the average bin contents (abc)
across the domain, and the error in the e-folding parameter,
d_e, is defined to be that which induces a 10% increase in
the rms error.

Thus, for the LMC(b & vb) data of Davies *et al.*
(1976) in the domain 1' - 10', d_e = 2!9 $\pm$ 0!4 with rms/abc
= 0.26 ($\equiv$ 42 $\pm$ 6 pc at 50 kpc), while for all the data in
same domain d_e = 4!6 $\pm$ 0!4 with rms/abc = 0.12.   Inclusion
of the few regions larger than 10' will lead to errors due
to small number statistics (and that risk is being run al-
ready) while inclusion of all those 'regions' smaller than

1' runs into problems of identification and completeness.

Henize's (1956) data was not analysed in this way because of the small amount of data available, but it is pleasing to see the same values for d_e emerging from both sets of 'bright' region data.   Similarly, the SMC data are too scant for this analysis.

Sandage and Tammann (1974a) use the LMC and SMC in the calibration of their HII region diameter - galaxy luminosity relation.   The diameters used are the means of the core and halo measurements of the largest three HII regions in any galaxy (see ch. 3.2).   These, designated S & T <c,h>, are shown in the upper portions of Table 3.1 together with the mean dimensions of the largest regions as quoted by Henize (1956), labelled H, and by Davies *et al*. (1976), labelled DEMX.   The dimensions are all in angular measure.

There is little similarity amongst the three sets of data.   However, inspection of the original sources revealed that many of these "largest regions" are arcs of faint nebulosity often surrounding brighter knots.   These two sorts of HII region correspond to classes 3 and 1, respectively, in the scheme of Monnet (1971).   In studies of the spiral structure of our Galaxy, Georgelin and Georgelin (1976) concentrated upon those regions with excitation parameters, U, greater than 70 cm^{-2} pc (see Mezger (1970) for the definition of U and of "giant" HII regions) as it is these bright regions that define the spiral structure of external galaxies.

Table 3-1

Angular Diameters (in arc minutes) of the largest HII regions in the Magellanic Clouds

Rank (by size)	1	2	3	4	5
Source			LMC		
H	30.3	28.3	22.3	19.6	17.6
DEML	56	50	42.5	35	32.5
S & T <c,h>	22.7	12.3	9.6	-	-
H-1	30.3	22.3	19.6	17.6	16.5
DEMLb	32.5	22.5	22.5	15	15
S & T <h>	30.1	20.3	13.9	-	-
			SMC		
H	9.0	6.1	5.2	5.2	5.1
DEMS	32.5	21	21	19	15.5
S & T <c,h>	6.8	3.4	2.5	-	-
H-1	9.0	5.2	5.2	4.8	4.6
DEMSb	12.5	5.5	5.5	4.5	4.5
S & T <h>	10.7	6.7	5.0	-	-

H   :   Henize 1956

H-1   :   as above excluding regions of brightness
      class 1

DEMX   :   Davies *et al.*, 1976

DEMXb :   as above restricted to brightness classes
      b, vb.

S & T :   Sandage & Tammann 1974a

c, h   :   core, halo

So, concentrating upon the brighter regions in the Clouds, i.e. restricting Henize's data to his brightness classes 2, 3, 4 and 5, labelled H-1 in Table 3.1, and similarly restricting the data of Davies *et al.* to their classes 'b' and 'vb' (bright and very bright), and restricting the data of Sandage and Tammann to their halo measures only we get a much more pleasing comparison (Table 3.1).

The largest discrepancy under these restrictions is the case of LMC3, which may be explained away if a region with a larger halo but smaller core remains hidden within Sandage and Tammann's data. With all the problems that core measurements seem to produce, their relative insignificance in determining a representative dimension (S & T I) and the doubts expressed about their very existence (S & T I, Hodge 1976, de Vaucouleurs 1977a), they may surely now be discarded.

Note that under this scheme the three sources give values of $<d>_3$ of, for the LMC, 24.1, 25.8 and 21.4 arc minutes respectively, giving a mean of 23!8, and for the SMC, 6!5, 7!8 and 7!5 respectively, giving a mean of 7!3, both with errors of about 10%. At the distances adopted by Sandage and Tammann (1974a) these give linear values for $<D_H>_3$ of 361 pc and 152 pc respectively.

3.7   *The Sizes of HII Regions in M31*

Hubble (1929, p. 151) declared gaseous nebulae in the Sb galaxy to be completely absent. Since then

many groups have observed and measured HII regions in
M31 and the three principal groups concerned are given
in the first lines of Table 3.2. In subsequent lines
are given the observational parameters and the numbers
of HII regions detected.

Plotting the size distributions from the data
of Baade and Arp (1964) and Arp and Bruekel (1973)
(figs. 3.5 and 3.6) it was clear that once again an ex-
ponential decay was the curve of simplest form with
which to fit the data. Curves were fit to the data for
all the regions and also to just the 'bright' regions
in each set. To examine the effect of changing the
definition of 'bright' the data of Pellet *et al.* (1978)
was analysed with two interpretations - first at their
definition of 'medium' brightness, and second at their
definition of 'high' brightness. The effect upon the
final value of d_e, the e-folding dimension (see line 11
in Table 3.2) is considerable - a factor of 2.3 - in the
light of which the agreement amongst the values of d_e
derived from the three sources using their own defini-
tions of 'bright' is quite remarkable.

Did the three groups by chance choose the same
levels of intensity at which to classify the HII regions
they observed? Or were they forced into their choice by
the form of the brightness distribution of HII regions?
If, for instance, this distribution is bimodal with, say,
Monnet's (1971) class 1 objects and Megzer's (1970) 'giant'
HII regions in the brighter hump, then a natural division
by brightness may occur. Excitation parameters of 100

Table 3-2

Observations of HII regions in M31

		Baade & Arp	Arp & Bruekel	Pellet *et al.*
(1)	Source			
(2)	Date	1964	1973	1978
(3)	Telescope	100"	48"	76"
(4)	Plate Scale	16" mm^{-1}	67" mm^{-1}	100" mm^{-1}
(5)	Filter (Hα)	broad	80$\overset{\circ}{A}$	28$\overset{\circ}{A}$
	"	"	(FWHM, interference)	
(6)	N_t	688	93	940
(7)	N_a	83	93	940
(8)	N_b	21	54	768 (516)
(9)	N_c	21	34	471 (223)
(10)	N_p	5	5	10 (10)
(11)	d_e	6"0	7"5	5"7 (13"2)
(12)	rms/abc	0.35	0.14	0.24 (0.16)
(13)	error in (11)	1"6	0"8	0"5 (1"6)
(14)	N_{ac}	83	61	649
(15)	N_{ap}	9	5	12
(16)	d_{ae}	10"5	11"0	19"5
(17)	rms/abc	0.49	0.11	0.13
(18)	error in (16)	1"0	1"0	1"2

Key

Line

(6) N_t : total number of regions detected
(7) N_a : the number in (6) assigned dimensions
(8) N_b : the number in (7) of "bright" regions as defined
in the source - the two entries in final column in lines
(8)-(13) refer to their "high and medium brightness" regions
and to their "high brightness" regions only, ( ), respectively.
(9) - (13): analysis of the bright regions in (8)
(13) N_c : the number in (9) used in the curve fitting
(10) N_p : the number of points or bins that N_c covered.
(11) d_e : the e-folding diameter of the best fitting exponentially
decaying curve to the data in (9) and (10).
(12) rms/abc : the rms error for the points in (9) and (10) about
the curve defined by d_e in (11), divided by the average bin
contents (i.e. N_c/N_p) to give a normalization of the fractional
error along the curve. It is this quantity that is minimized
in producing d_e.
(13) error in (11) : .... to produce an increase in (12) of 10%
(14) -(18): analysis of all regions N_a in (7)
(14) - (18): correspond to (9) - (13)
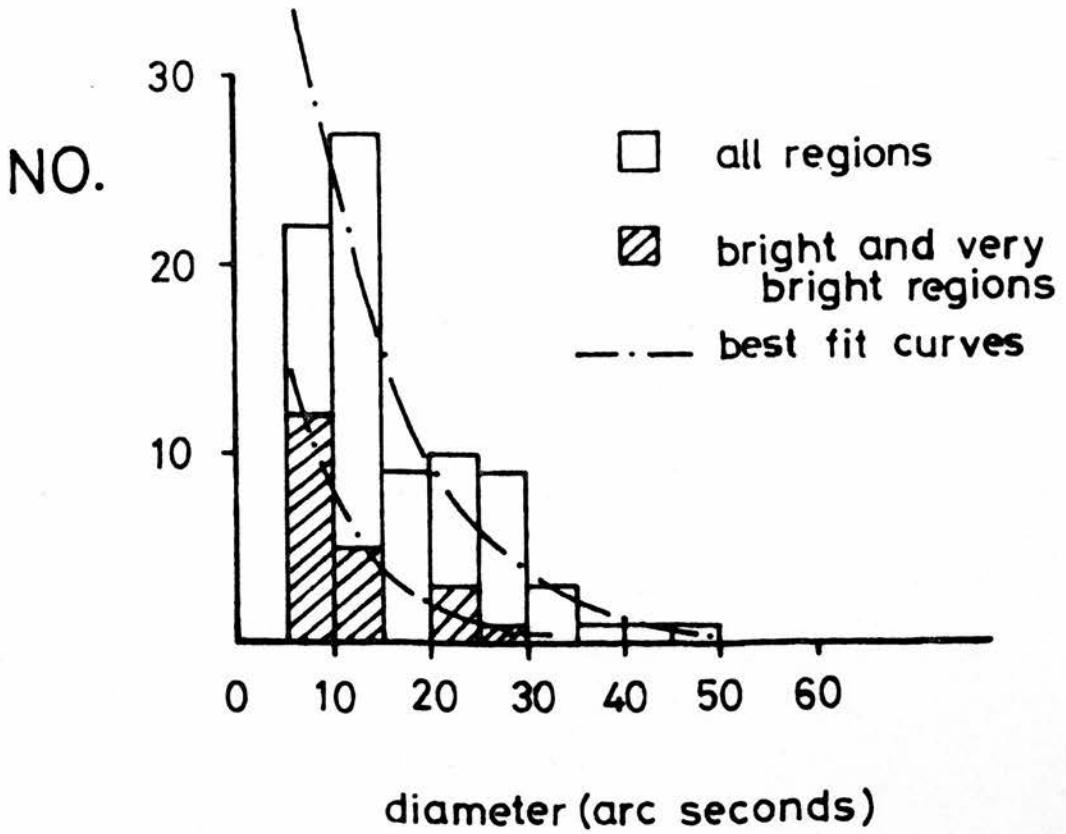
Figure 3.5. The sizes of HII Regions in M31.
Data from Baade and Arp (1964).
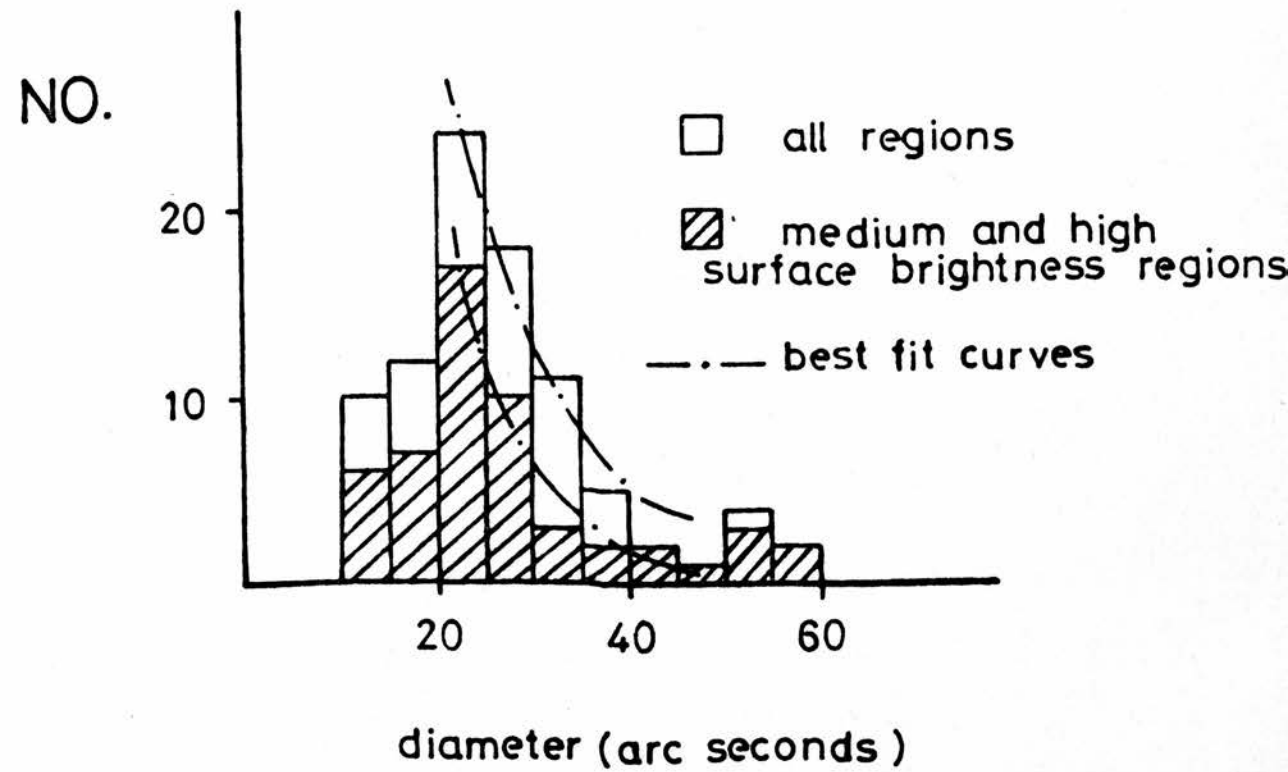
Figure 3.6. The Sizes of HII Regions in M31.
Data from Arp and Bruekel (1973).
Not shown is one region of size 150".

and 200 cm^{-2} pc. have been suggested (Georgelin *et al.* 1979) as divisions between the diffuse regions, the normal HII regions and the giant regions.

The values of d_e resulting from analysis of all the data in Table 3.2 (see line 16) would not give much confidence in a mean result.

As a mean result from the values of d_e in line 11 of Table 3.2, and this is for the 'bright' regions,

$$d_e(M31) = 6\overset{\prime\prime}{.}3 \pm 1\overset{\prime\prime}{.}0 .$$

At a distance of 650 kpc (de Vaucouleurs 1978a) or 520 kpc (Sandage and Tammann 1974a) this corresponds to 20 ± 3 pc or 16 ± 2 pc respectively.

3.8   *The sizes of HII regions in M33*

The size distribution of HII regions in M33 is presented by Sandage (1962). No partition by intensity is made. The distribution shows an exponential decay toward larger diameters, and the best fitting curve of this type has an e-folding diameter of $6\overset{\prime\prime}{.}0 \pm 0\overset{\prime\prime}{.}3$ with r.m.s./abc = 0.10.

Courtes and Cruvellier (1965) studied the central 14' of this galaxy with a system that used a $4\overset{\circ}{A}$ Hα filter. The exclusion of or the effect upon the intensity of the images of those HII regions whose velocities take their Hα emission out of the bandpass ($\pm 2\overset{\circ}{A}$ at $6563\overset{\circ}{A} \equiv \pm 90$ km s^{-1}) may affect the way the image sizes are measured. Their data has been used to form the histogram in Fig. 3.7a, the 'bright' regions being those that they classified

a)

NO.
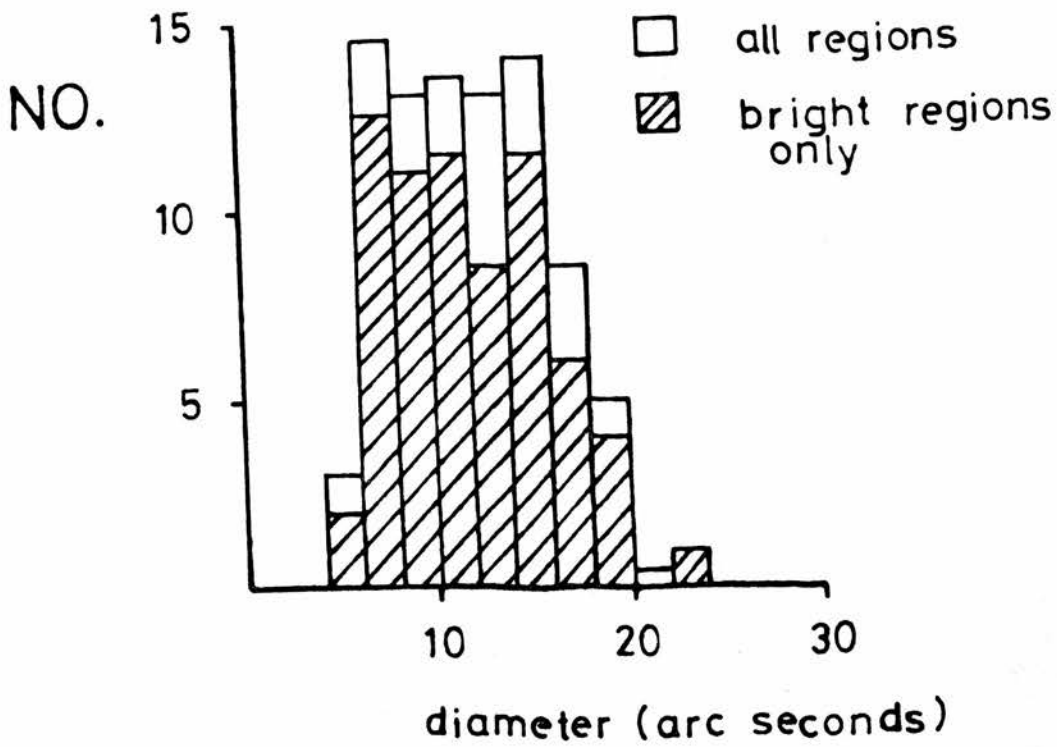
b)
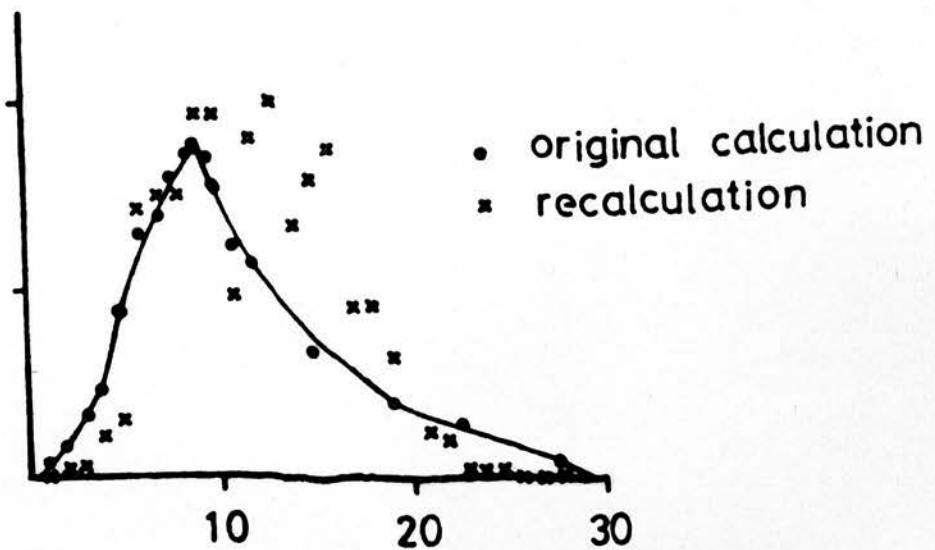
Figure 3.7. a) The Sizes of HII Regions in M33.
Data from Courtès and Cruvellier (1965).

b) The same data smoothed (see C and C 1965).

'medium' or 'bright'. They smooth their data, as illus-
trated in Fig. 5.7b, to account for the uncertainties in-
duced by the seeing. (Such may be important whenever
seeing effects are important). This curve was then used
to calculate the 'most probable' size of HII region, and
they determined this to be 9". Repeating their technique
produced a quite different 'smoothed' curve, as shown in
Fig. 3.7b, and a 'most probable' size of 13", in accord
with the value derived by Boulesteix *et al.* (1974).

Boulesteix *et al.* (1974) detected and measured
369 HII regions in M33 using a 25$\overset{o}{A}$ H filter. Their data
for all regions described as being of 'medium' intensity
or brighter has been used to form the size distributions
shown in Fig. 3.8. A bin size of 5 arc secs has been used
here in preference to the 2.5 arc sec bin size used by
Boulesteix *et al.* (1974) to be slightly more in line with
the quoted seeing size of 4".

The 'most probable' size to be deduced from
Fig. 3.8 is 10", though the error on this could be as much
as 5". The exponential decay curve best fitting the data
for diameters greater than 12" has an e-folding diameter
of 10.''3 $\pm$ 0.''6 which at a distance to M33 of 720 kpc (de
Vaucouleurs 1978d) or 820 kpc (Sandage and Tammann 1974a)
converts to (36 $\pm$ 2) pc or (41 $\pm$ 2) pc respectively.

3.9   *The Sizes of HII Regions in NGC 6822*

Hodge (1977) gives the dimensions of 16 HII
regions in this magellanic irregular, the distance to
which is given variously as 560 kpc (de Vaucouleurs 1978b)
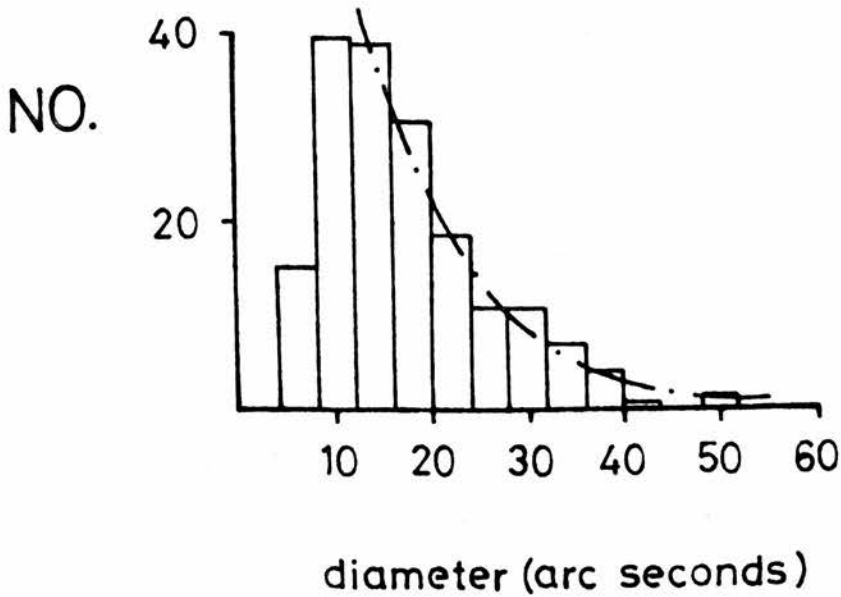
Figure 3.8. The sizes of HII Regions in M33.
Data from Boulesteix *et al.* (1974).
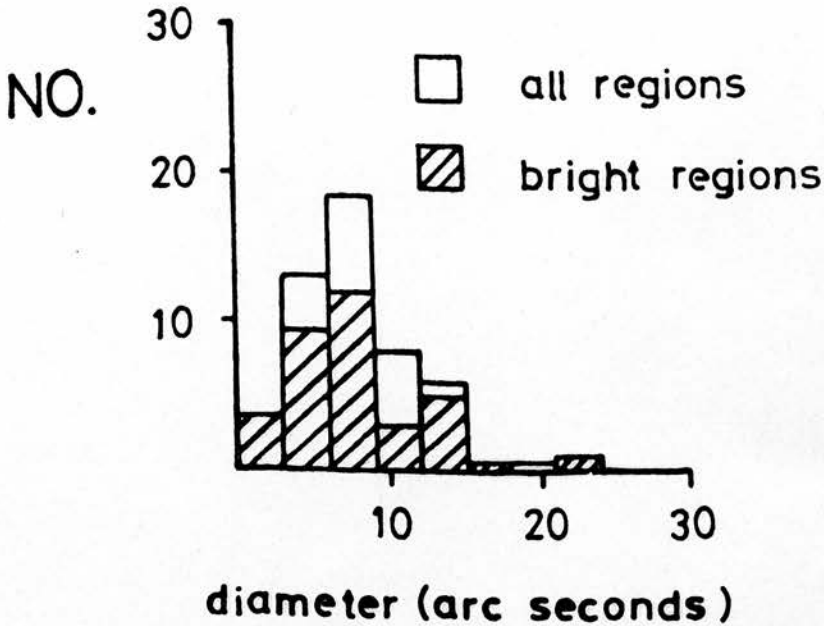
Figure 3.9. The sizes of HII Regions in NGC 2403.
Data from Véron and Sauvayre (1965).

and 630 kpc (Sandage and Tammann 1974a). Although there is really too little data to put much confidence in any analysis similar to those preceding, the data can be well fit to an exponential decay curve of an e-folding dia-meter of 30" ≡ 90 pc at 600 kpc.

3.10   *The Sizes of HII Regions in the Local Group*

In summary of the results of the preceding four sections, Table 3.3 shows the e-folding diameters of the size distributions in the Local Group.

There appears to be a relation between d_e and T, in that they both increase in value together. This may be interpreted as an increase in the proportion of large HII regions in the galaxies of later type, in accord with the evolution of spiral (and irregular) galaxies as de-scribed by Sandage (1975).

3.11   *The Sizes of HII Regions Outside the Local Group*

a)   NGC 2403

Véron and Sauvayre (1965) have presented data for HII regions in the ScIII galaxy NGC 2403 and these have been used to produce the histogram in Fig. 3.9.

The best fitting exponential decay curve to the right side of the distribution has d_e = 5.4 $\pm$ 0".3 with rms/abc = 0.57, though better accuracy could not have been expected with such little data. At a distance of 2.6 Mpc (de Vaucouleurs 1978d) this corresponds to 70 $\pm$ 4 pc.

Table 3-3

Characteristic e-folding diameters of the
size distributions of HII region diameters in
galaxies in the Local Group

Galaxy	Type	T	L	M_{pg}^{o}	d_e(pc)
MW	ScIII?				22 ± 1
LMC	Irr	9	6	-18.17	45 ± 6
M31	SbII	3	2	-20.48	21 ± 3
M33	SCIII	6	4	-18.51	36 ± 2
NGC 6822	Irr	10	8	-15.20	90:

Notes : Type, T, L, M_{pg}^{o} from RGBG2 or de Vaucouleurs
1978b.

Table 3-4

Size distribution of HII Regions in NGC 628

Mean Size (")	N_a	N_b	Mean Size (")	N_a	N_b
2.5	168.6	70.7	7.5	11.5	10.7
3.5	112.8	74.6	8.5	8.1	6.5
4.5	63.7	46.4	9.5	5.6	5.0
5.5	27.6	24.3	10.5	2.2	2.2
6.5	16.7	13.1			

Table 3-5

Best fitting e-holding curves to the data in Table 3-4

Bin Size	Data	d_e	error	rms/abc
1"	All	1.7	0.1	0.09
1"	Bright	1.9	0.1	0.07
2"	All	1.85	0.1	0.03
2"	Bright	2.0	0.1	0.05

N_a, N_b, d_e, error, rms/abc are explained in the key to
Table 3-2.
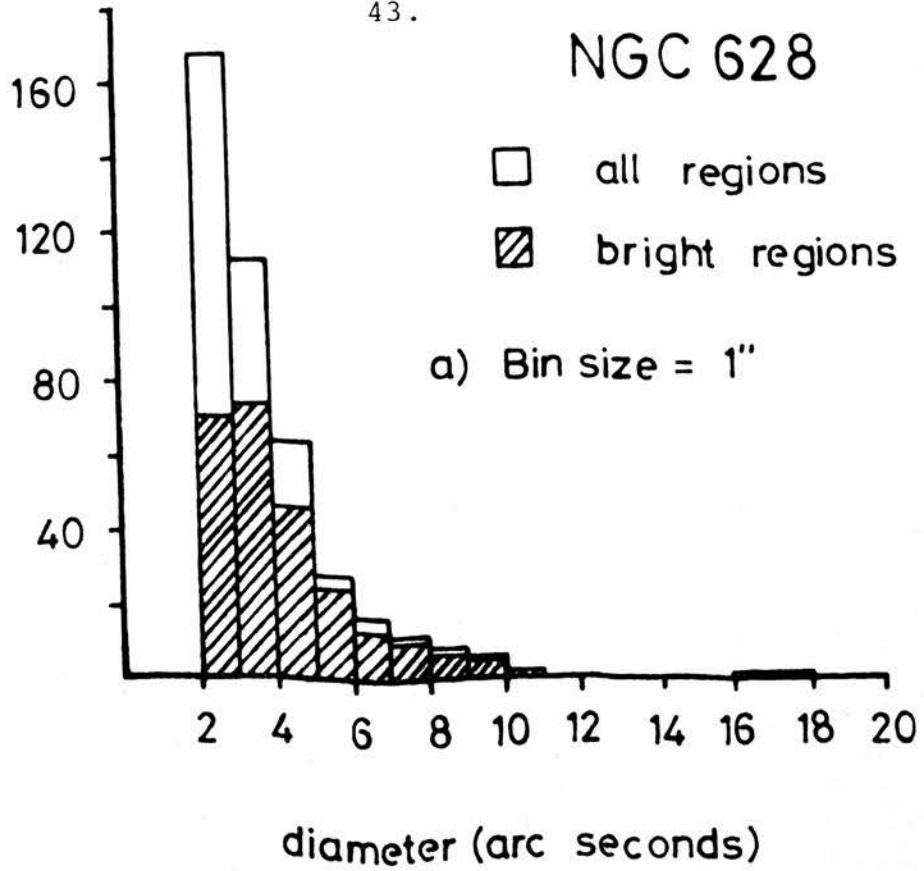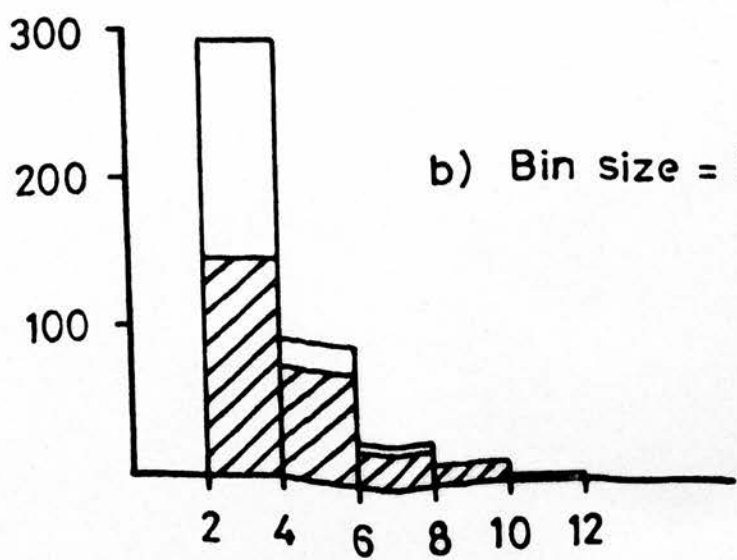
Figure 3.10. The Sizes of HII Regions in NGC 628. Data from Hodge (1976b).

b)   NGC 628 (M74)

Hodge (1976b) has presented measurements for the
HII regions in this ScI galaxy taken from an H_α plate
taken through a 20Å (FWHM) Hα filter. The dimensions
are quantised into integral numbers of arc seconds. For
analysis here his figures were adjusted thus:

(i)   By examining his photographs and choosing his
          region no. 48 as a brightness standard, the HII
          regions were divided into two brightness groups.

(ii)   Allowance was made, by equation (3.1), for the
          seeing, quoted as 2".   The data is then as shown
          in Table 3.4 and Fig. 3.10, and was then analysed
          in four ways as shown in Table 3.5 to discover
          the effect of different binning arrangements.   To
          within 10% the value of d_e thus derived is inde-
          pendent of the binning.   2".0 at 8.3 Mpc (de Vau-
          couleurs 1979b) corresponds to 83 pc.

c)   NGC 3631

Boeshaar and Hodge (1977) give data for the HII
regions in the ScI galaxy NGC 3631.   This data has been
corrected as above for seeing of 2".5 and divided into
two brightness groups by comparison with their region
no. 8.   The best fit curves to the right sides of the his-
tograms shown in Fig. 3.11 have

$$d_e = 1".8 \pm 0".2 \text{ with rms/abc} = 0.14 - \text{bright regions}$$
$$d_e = 1".5 \pm 0".1 \text{ with rms/abc} = 0.05 - \text{all regions.}$$
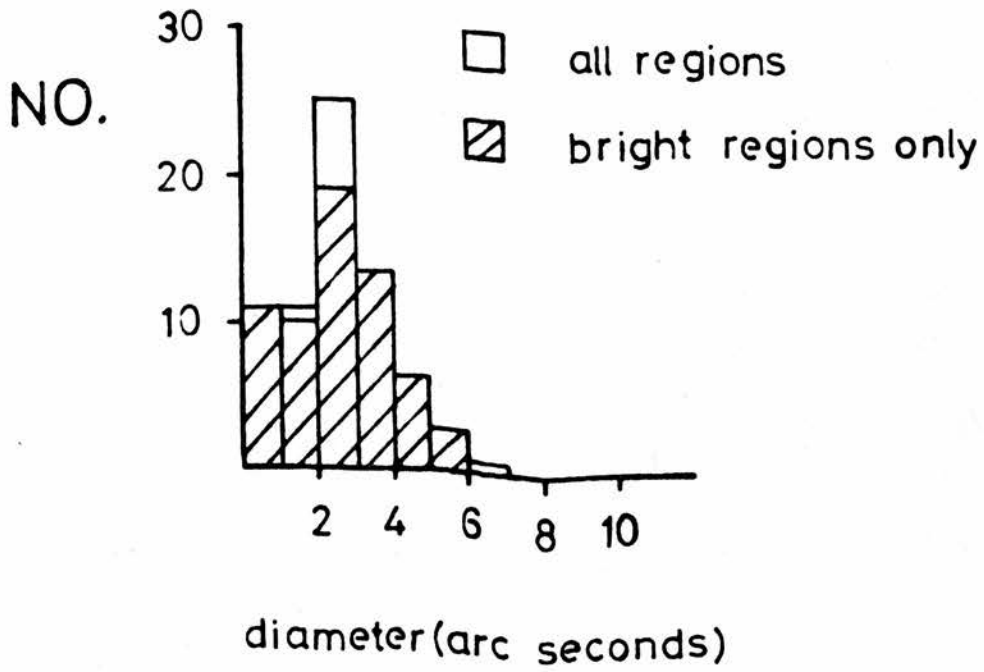
Figure 3.11. The Sizes of HII Regions in NGC 3631. Data from Boeshaar and Hodge (1977).

Experimenting again with the data to see the effects of certain changes, suppose that the four largest regions had been resolved into four regions each* of half the size, then we would have found

d_e = 1".5 $\pm$ 0".3 rms/abc = 0.20 for the bright regions

d_e = 1".3 $\pm$ 0".1 rms/abc = 0.13 for all regions;

changes that are hardly significant.

At the distance adopted by de Vaucouleurs (1979b) of 16.1 Mpc, 1".8 corresponds to 145 pcs.

Summary   The above are the only comprehensive sets of data on the diameters of HII regions in galaxies outside the Local Group. With them we have seen that 1) acceptable changes in the binning arrangements and 2) what may be typical of resolution problems, as illustrated with NGC 3631, produce little significant changes in the value of d_e.

However, the factor of 2 difference in the values of d_e for the two ScI galaxies above is worrisome.

3.12   *HII Regions - Galactic and Extragalactic*

General data on galactic HII regions may be biased by selection effects, and data on their sizes are certainly subject to the uncertainties in the determinations

---

* Wilson (1975) speculates that the giant galactic HII region W49A is made up of smaller regions, and Brand *et al.* (1980) describe the resolution of one large 'region' in M83 into a few smaller ones.

of their distances (ch. 3.5). However, it should be
possible to determine qualitatively whether galactic HII
regions are similar to those elsewhere, or not.

The optically picturesque galactic HII regions,
like M42, M8, M2O, M16, M17 and others are typically a
few tens of parsecs across (Georgelin and Georgelin,
1970b), M16 being the largest of these at 86 pc, M42 the
smallest at 8 pc. In the scheme of Churchwell (1975)
M42 is the youngest and shall expand as it develops until,
although still optically visible, it becomes a weakened
diffuse radio source. Many of the shells of gas we see
in H_α photographs will be such shells - others are super-
nova remnants. Somewhere along the line the HII region
ceases to be 'bright' in the optical sense discussed
previously, so restricting measurements of sizes to the
bright regions is selecting the younger regions and, pre-
sumably, those that best define the spiral arms by their
general association with regions of star formation.

Some HII regions are excited by single O-stars
(e.g. M17, Lemke 1975) while others are excited by
associations (e.g. M8, Hiltner *et al*. 1964, M16, Walker
1961, M42 by the trapezium). The 'giant' HII region W49A,
not visible at optical wavelengths because of galactic
dust, but studied at radio and infra-red wavelengths,
may be excited by some hundreds of O-stars (Wilson 1975).
On a slightly larger scale, the massive HII regions in
M101 may require as many as one thousand O-stars to pro-
vide enough flux for the ionization observed (Searle 1971).

In this sense, then, the galactic 'giants' may well be comparable with those we are able to observe in the optical in other galaxies. The largest galactic HII region available to us at optical wavelengths, the Gum Nebula, is rather enigmatic. Current theories (Reynolds 1976a,b, Kafatos 1976, Brandt *et al.* 1976) combine the two previously contending theories into one and suggest that it was originally formed by a supernova explosion and is now maintained in its state of ionization by more normal HII region processes. Its size is still in dispute, though, estimates ranging from 250 pcs to 700 pcs.

Spectra of galactic HII regions have been presented by Hawley (1978), and for extragalactic nebulae by Searle (1973), Smith (1975), Shields and Searle (1971), Pagel *et al.* (1978), Pagel *et al.* (1979), Dufour *et al.* (1980) and others. Such data has established the presence of composition gradients across spiral galaxies that can most simply be explained by an increase in the rate of nucleosynthesis towards the centre of the galaxy combined with increased dustiness in inner HII regions (Sarazin 1977). The latter resulting in the absorption of a significant part of the ionizing flux and in a reduction in the size of the HII region.

That the composition gradients are steeper in spirals of earlier type is indicative (Smith 1975) of an evolutionary effect linked to the amount of gas available for star formation: those galaxies with larger amounts of gas (the later types) have smaller fractional amounts processed into heavy elements.

Insofar as these factors affect the sizes of HII regions, one would expect that the HII regions of two galaxies of the same type would have the same size distribution.

3.13 *Objective measurements of the sizes of HII regions*

The first systematic machine-aided measurements of the sizes of HII regions have been made recently by Kennicutt (1979a, b, c). Following the approach of Sandage and Tammann (1974a, d) he obtained H_α photographic and photometric data for the same sample of galaxies studied by Sandage and Tammann and derived isophotal diameters for the largest HII regions.

Using the same foundations to the distance scale he obtained a value of the Hubble Constant, H_o, that was somewhere between 0% and 40% larger than that derived by Sandage and Tammann. The principal difference between the results of Kennicutt and Sandage and Tammann is that S & T's core/halo diameters are systematically smaller for the smaller regions than Kennicutt's isophotal diameters which leads to systematically larger distances for the more distant galaxies and to a smaller value of H_o.

Either Sandage and Tammann's diameters are subject to the effect described in Ch. 4.1 by which small images are measured smaller than they ought to be, or Kennicutt's isophotal diameters are subject to systematic errors in the seeing deconvolution.

The work of Sandage and Tammann has been examined already (Ch. 3.2). Before tackling this specific question

about Kennicutt's results let us examine his approach
to using these machine measures.

In his first paper (Kennicutt 1979a, hereafter
K1) Kennicutt examines the morphology of the HII regions
he is about to measure. The photographs concerned are
taken through H_α interference filters of width "20-75Å",
so it is unclear how much [NII] appears in the images.
As discussed in Ch. 5-2, however, the effect of [NII]
contamination upon the H_α morphology may be negligibly
small. The photographs were calibrated, and so density
mapping of the plates by a micro densitometer allowed the
production of intensity maps and it is the morphology
of the HII regions on these that was examined.

For a few regions, the structure was simple
enough that the diameters derived from the intensity
plots could be compared with S & T's 'eyeball' measure-
ments. More generally, though, the HII region structure
was too complicated to allow unambiguous core and halo
assignations. The cores were often multiple and the
outer parts of the regions often broke up or blended in-
to the background emissions. In the data to be presented
here no clear-cut edges to nebulae were observed, though
how how much of this is due to seeing smoothing will be
explained later (Ch. 5.3).

'Visual' diameters were measured by Kennicutt
and a co-worker to ascertain the personal equation in-
volved in such measurements, but measurements of cores
were abandoned after proving too difficult to assign con-
sistently. (No core measures were made in the similar

work presented here - Ch. 5.5). The personal equation
involved was illustrated, although the results of any
one observer did prove internally consistent.

Several definitions of an objective diameter,
to be derived from the intensity maps, were tried by
Kennicutt, and many were rejected. One such was a 'simple
half width' - rejected because 'seeing and continuum
contamination may introduce considerable (distance depen-
dent) error into the peak surface brightness level'. Con-
tinuum contamination is shown (Ch. 5.2) to be negligible,
and full account of the seeing coupled with close exami-
nation of the intensity morphology allows a reconstruc-
tion of the intrinsic intensity morphology and intrinsic
size. The diameter eventually selected by Kennicutt was
the mean of a pair of isophotal diameters, selected to
lie within the calibrated intensity range of the plate
and chosen to mimic, to some degree, the core and halo
of Sandage and Tammann. The exact choice of this pair
is apparently not critical to the distance scale so pro-
duced, so, presumably, as a degenerate case, a one-isophote
diameter would suffice. Without accounting for the seeing,
this may well be a 'simple half width'.

Kennicutt determines the seeing by mapping of
field stars. Their profiles were adequately gaussian,
as was found here (Ch. 4.7), and they were deconvolved
from the HII region profiles which were graphically fit
(K1) to a guassian or pair of gaussians. This is an
assumption about the intensity profiles that cannot be
taken lightly; although in his data the seeing correction

averaged less than 20% of the HII region profile and is
consequently not as likely to introduce very large errors
into the diameters as it may in this work, where the images
of some HII regions approach the size of the star images.

In his second paper (K2), Kennicutt calibrates
the HII region isophotoal diameters with measures in
the Local Group and M81 group. Plotting $<D>_3$ against
M_{pg}^o, as described in Ch. 3.2, produces a relation similar
to equation (1) of S & T I, with a slope close to that
of the distance effect line. He turns, like Sandage and
Tammann (1974a) to van den Bergh's luminosity class as a
new variable against which to plot $<D>_3$.

Systematic differences between the sizes of the
HII regions in these two groups are examined and explained
(K2) as being due to an overestimation of the distance
to the M81 group, and extrapolation of the $<D_3>,L_c$ rela-
tions established for these groups to the ScI class of
galaxy and to M101 in particular raise again the questions
of the normality of that galaxy, its HII regions and its
place within its cluster. (See Ch. 3.2). As a result,
three separate possible calibrations are presented in K2.

It also appears (K2) that the isophotal diameters
from the M101 group are best fit by a calibration based
on the M81 group alone, and that perhaps the Local Group
galaxies have been classified too bright. Results in K3
tend to support this view.

Applying the various calibration formulae to
21 field galaxies allows the calculation of the distances
to these galaxies and of their absolute magnitudes. There

appears to be a large systematic distance effect between Kennicutt's data and that of Sandage and Tammann (1974d) as mentioned earlier in this section. The possible explanations mentioned earlier were recognised by Kennicutt (K2), but the evidence he presents in K3 tends to indicate that the major source of error is in the S & T scale.

The value of H_o he derives from these analyses (K2) is somewhat larger than that derived by Sandage and Tammann (S & T I-VII), but the associated error of about 20% he attributes in large part to the uncertainty in the HII region diameter calibration.

3.14   *Empiricism*

If the sizes of HII regions are to be anything more than numbers on which to base an empirical distance indicator then some attempt at relating their measurement to some physical basis should be attempted.

However, that is not to say that a relation based upon an empirical 'diameter' and shown to be useful in its employ should be discounted because the diameter means nothing physically. A lot of astronomy started out as 'botany' i.e. classification, until the qualities so described could be meaningfully quantified. Spectral classification is the prime example, and de Vaucouleurs (1979a) describes the similar usage of type- and luminosity-indicators for galaxies.

Similarly, a usable definition of 'diameter' for HII regions should be used until a more physically based

one can replace it. While the methods in this work
seek to establish such a physical basis for these 'dia-
meters', the sizes of HII regions as measured by eye
from photographic plates and reduced, simply, by assuming
a gaussian form for the profile of both HII regions and
stars, and which are at that stage related, but in some
uncalculated way to the physical dimensions of the HII
region, should not be considered inferior parameters un-
til proven so.

CHAPTER 4

THE DATA AND ITS REDUCTION

4.1   *Concepts*

Only recently (Hodge 1976, Kennicutt 1979a, b)
have plate measuring machines been used in measuring HII
regions. In only a few galaxies (see Ch. 3) are complete(!)
size distributions compilable, and these have been made
by visual inspection and measurement.

Presented here are data on the sizes of HII regions
in 10 southern spiral galaxies (Table 4.1) taken from
mapping data of photographic plates made by an automatic
plate measuring machine. It is to be demonstrated that
this presents an improvement in the quality of this kind
of data, which at present leads to large uncertainties
in the value of H_o ($\sim$40% according to van den Bergh 1979,
20% Kennicutt 1979b).

The advantages of an automatic plate measuring
machine, like COSMOS at R.O.E., are many fold:

i)   it is fast;

ii)   it is accurate and consistently so, though in
        resolution it may be irregularly bettered by the
        human eye and brain;

iii)   it has a superior intensity/density resolution
        than the eye;

iv)   it has none of the subjective biases of the human
        eye/brain, e.g. it does not experience the effect
        noted by Hubble (1932) and described by de Vaucouleurs

Table 4-1

Ten Southern Spiral Galaxies

NGC	Type	D_{25}	m_C	V_C
1097	SB(s)b	7!9	$10^m.3$	1227 km s^{-1}
1179	SAB(r)cd	5.3	13.3	-
1232	SAB(rs)c	7.1	10.6	1644
1300	SB(rs)bc	6.3	11.2	1422
1313	SB(s)d	7.8	10.6	241
1365	SB(s)b	9.3	10.6	1502
1566	SAB(s)bc	7.2	10.3	1178
2442	SB(s)b	5.9	11.1	384
2997	SAB(rs)c	6.9	10.6	805
5236	SAB(rs)c	10.5	8.6	337

Column 1 gives the NGC number

2 the morphological type

3 the diameter in arc minutes

4 the corrected photographic magnitude

5 the corrected recessional velocity

All data from RC2

(1977a) whereby the eye measures small images
too small and which have been seen (Ch. 3) to be
a possible source of systematic error in the
determination of a cosmic distance scale.

The advantages to be gained in working with the
sizes of all the HII regions in a particular galaxy in-
stead of a restricted sample of 3 or 5 are that the effects
of deviants in such a sample are reduced. However, the
problems of identification, measurement and completeness,
particularly for the smaller regions will be encountered.

In this work, M83(NGC 5236) has been most intense-
ly studied because of its brightness and apparent size.
By measuring HII regions in M83 on several plates it is
hoped

i)   to derive intrinsic intensity profiles and hence
        characteristic sizes, by deconvolving the observed
        HII region profiles with those of star profiles;

ii)   to compare results, plate with plate, to deduce
        any telescope, exposure, seeing or other depen-
        dences that may affect these characteristic sizes;

iii)   to compate results with 'eyeball' measures of the
        same material to illustrate the improvement in
        the data quality;

iv)   to determine standard conditions, if necessary,
        to which to reduce further data;

v)   to produce size distributions for all the galaxies
        in the present sample and to determine from them
        some property that will be useful as a distance
        indicator;

vi)   to throw light, in passing, on HII region
        morphology.

4.2   *COSMOS*

The COSMOS automatic plate measuring machine
at ROE has been fully described by Pratt (1977). In its
'mapping' mode, as used here, it measures the transmission
of the plate by shining a beam of light through it and
comparing the intensity of the emergent beam with that of
the incident beam. The plate carriage is moved a step of
8 or 16 microns (10^{-6} m) and another measurement made, and
the designated area of the plate is covered like this in
a raster scan fashion. Transmissions are quantized to
integer values between 0 (opaque) and 127 (transparent),
and these values are stored on magnetic tape in known se-
quence.

Calibration areas of the plate are mapped at the
same time allowing conversion from COSMOS transmission
to relative intensity (see Ch. 4.4).

At the time that this work was carried out the
COSMOS spot (beam) was approximately gaussian in intensity
profile and of width 25.2 μm (FWHM). The step sizes used
were 8 μm for the UKST plates and 16 μm for the AAT plates.

Appendix C describes the computing necessary to
analyse COSMOS mapping data.

4.3   *The XY-machine*

The XY-machine at ROE consists of a supported

eyepiece mount on a moveable carriage. The position of
the carriage is determined by reference to two orthogonal
Moiré fringes and it displayed on a digital display unit
in units of 10 microns. The stepping motors allow motions
of one third of this, and, allowing for backlash, repeat-
ability is certainly no worse than 10 microns. The accu-
racy of the fringes is estimated to be a few microns.

There are doubts about the orthogonality of the
drive axes, but this effect is quite negligible over the
small areas of plate covered in this work. Drifting of
the carriage without corresponding response from the dis-
play unit, especially during 'warming up', is counteracted
by repeated measurements of the positions of standard stars.

Measurements made by eye are subject to a great
deal of personal bias (Sandage and Tammann (hereafter S & T)
1974a). As such it is difficult to describe exactly what
one does when aligning the crosswires at the 'edge' of an
image. Immediate repetition of the measurement is, of
course, biased by memory of the previous one, so repetition
was not effected until after the elapse of some considerable
time (like 24 hours).

The assigned dimensions were acquired with the
accuracy of the machine repeatability which at least in-
dicates some consistency in the 'eyeball' approach. Only
7% of measured 'diameters' repeated to worse than 10 microns,
and 1% to worse than 15 microns. No systematic errors in
the measurements of NS & EW dimensions was apparent.

The average scatter in the measurements of HII
regions on the 4 UKST plates of M83 (see Table 4.2) was 7

microns.

4.4.   *The Photographic Material and its Calibration*

Photographs of the galaxies in Table 4.1 were ob-
tained during 1975-77 with the UK 48" Schmidt Telescope
and the Anglo-Australian 3.8 metre reflector.   Details
of these plates are given in Table 4.2.   All the galaxies
apart from NGC 1313 are in unvignetted regions of the
plates.

Hα photographs of M83 are presented by Dufour
et al. (1980) and Talbot *et al.* (1980), and of NGC 1365
by Pagel *et al.* 1979.   Hodge (1969c) presents photographs
of NGC 1232, NGC 1300 and NGC 1365 and Garrison and Walborn
(1974) present photographs of NGC 1300, NGC 1566 and NGC
1313.   Intensity contour maps of M83 are shown in Figs.
4.8 to 4.17 and of the other galaxies in Appendix E.

Calibration of the plates

It is required to convert the COSMOS transmissions
to the intensity of the incident radiation.

Each U.K. Schmidt plate comes equipped with two
stepwedges produced by light of known relative intensity.
At the time that this work was carried out the UKSTU data
for these wedges was as shown in the first line of Table
4.3.   Stepwedge profiles in units of transmission are shown
in Figs. 4.1 and 4.2 for 10 UKST plates.   As can be seen
they vary considerably in quality - the best ones, fortui-
tously, being those for the plates of M83.   The same data
may be displayed as histograms of transmission and one such

is shown in Fig. 4.3. Table 4.3 gives the values of the transmissions deduced from such data for each step on each of the five UKST plates of M83, and these are plotted against log I in Figs. 4.4.

Data from the other five stepwedges was not considered satisfactory for present purposes and so an alternative method of calibration was sought.

The <u>MacBeth Densitometer</u> of U.K.S.T.U., R.O.E., measures diffuse density i.e. it shines a beam through the test material and collects the emergent light over 2π steradians. Diffuse density, D, is related to transmission, T, by

$$D = c - \log T \tag{4.1}$$

The spot of the 'MacBeth' was about 5% wider than a UKST plate wedge step and thus about 2% contributions from plate on either side of a step will contaminate the readings for any one step. However, in a step wedge arrangement these will tend to cancel out except for the highest density step. The scatter in repeated measurements of the steps was on average 0.02 in density, comparable with the accuracy with which the corresponding transmissions could be determined.

The results of stepwedge measurements on the seven UKST plates treated in this way are presented in Table 4.4 and Fig. 4.4.

The value of the constant in equation (4.1) was determined for each plate by measuring, with the 'MacBeth', the density of the sky background at four points to each

Table 4-2

Photographic Plate Material

Plate	Galaxy NGC	Exposure m	Emulsion	Filter	Seeing $''$	Date
Hα 3223	5236	120	127-04	Hα(AAO)	1,2,1-2	4-6-77
Hα 2918	"	60	"	"	2,2	17-2-77
Hα 2886	"	30	"	"	2,3-4	9-2-77
Hα 2955	"	13	"	"	2,2	13-3-77
R 1350	"	10	098-04	RG 630	Diff. Ltd.	23-3-75
AAT 1402	"	120	127-04	Hα(AAO)	3	9-5-77
AAT 1404	"	60	"	"	"	9-5-77
Hα 2579	1097	180	098-04	"	3,3	3-9-76
Hα 2595	1313	240	"	"	1-2,1	14-9-76
Hα 2600	1179	240	"	"	2,1-2	15-9-76
	1232					
	1300					
Hα 2606	1365	200	"	"	1,1	16-9-76
Hα 2683	1566	120	"	"	2-3,2-3	10-11-76
Hα 2871	2442	240	"	"	1,2-3	30-1-77
Hα 2937	2997	180	127-04	"	2,2	28-2-77

Notes

1) All emulsions are by Kodak

2) the 127-04 emulsion is now called the IIIaF.

3) the Hα filter of the AAO is of Gaussian profile, of FWHM 100Å and is centred at 6563Å.

4) the seeing is for translation and diameter when two figures are given, and as a total when one only is given. They are as quoted by the observer.

5) the AAT plates were taken by IMC. The doublet corrector was used and gives a plate scale of $16''24 \text{ mm}^{-1}$. All UKST plates were taken by UKSTU personnel and have plate scales of $67''2 \text{ mm}^{-1}$.
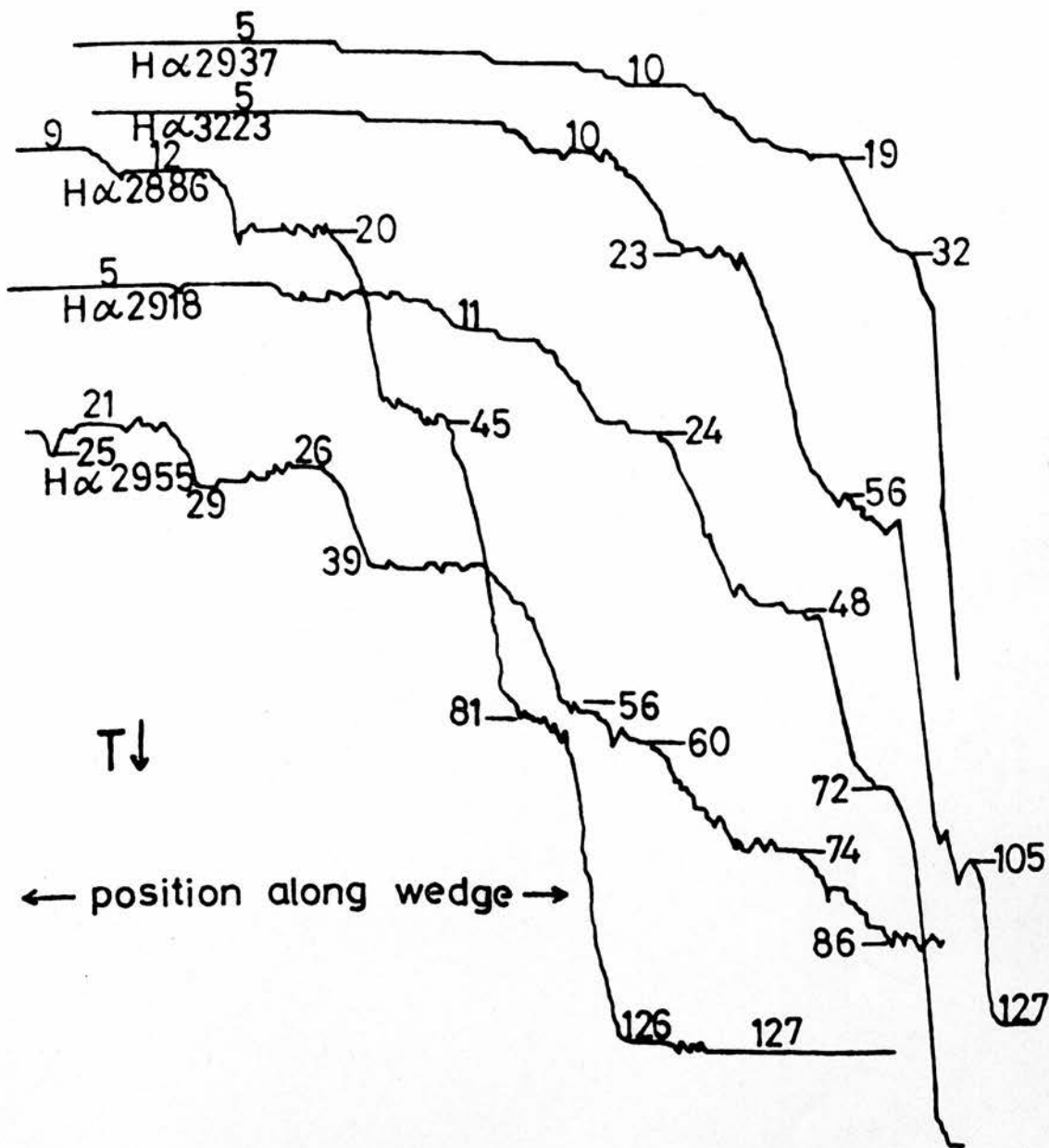
Figure 4.1. Scans in Transmission through the calibration stepwedges of 5 UKST Hα plates.
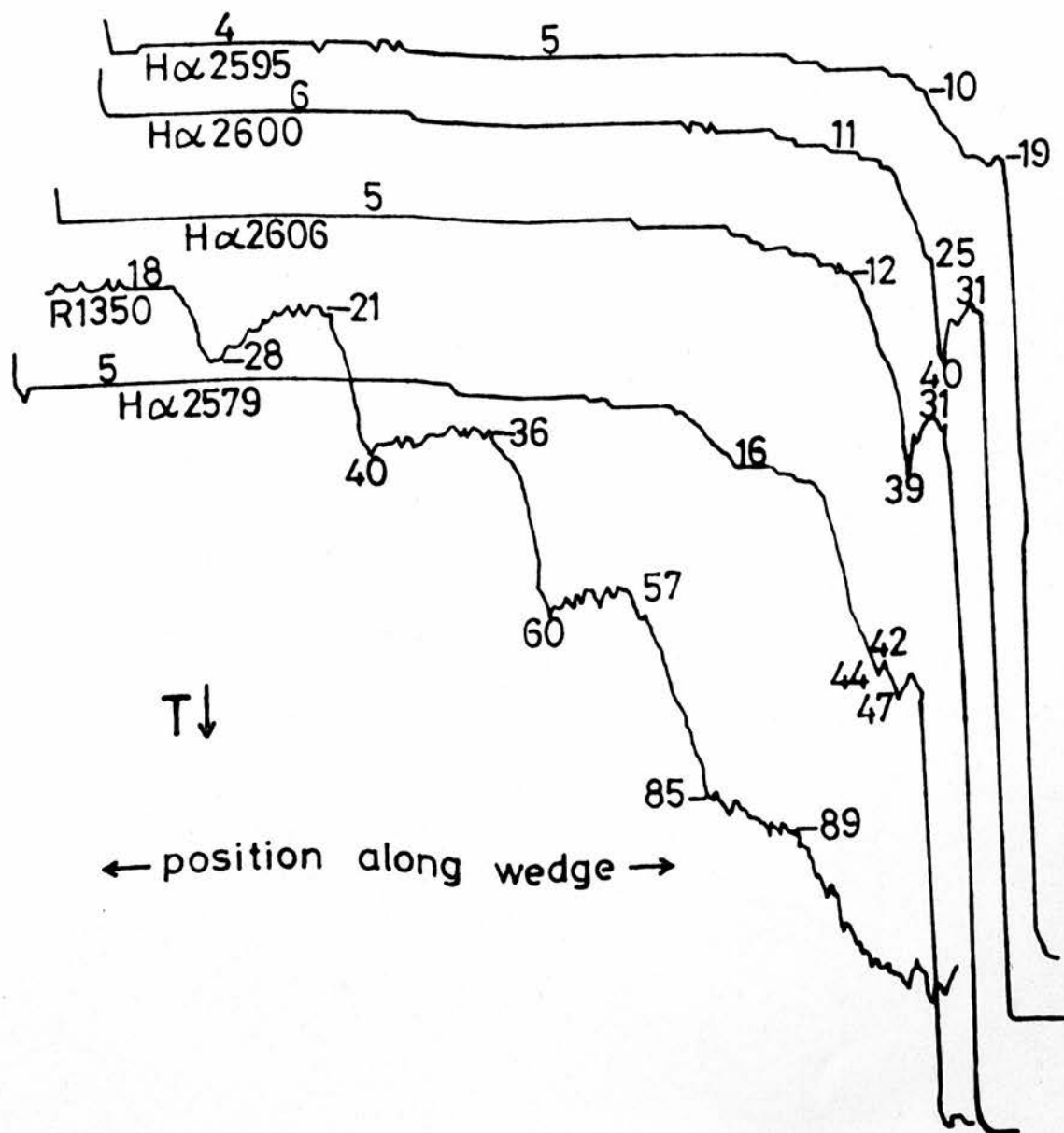
Figure 4.2. Scans in Transmission through the calibration stepwedges of 5 UKST Hα plates.

NO.

plate Hα 2955
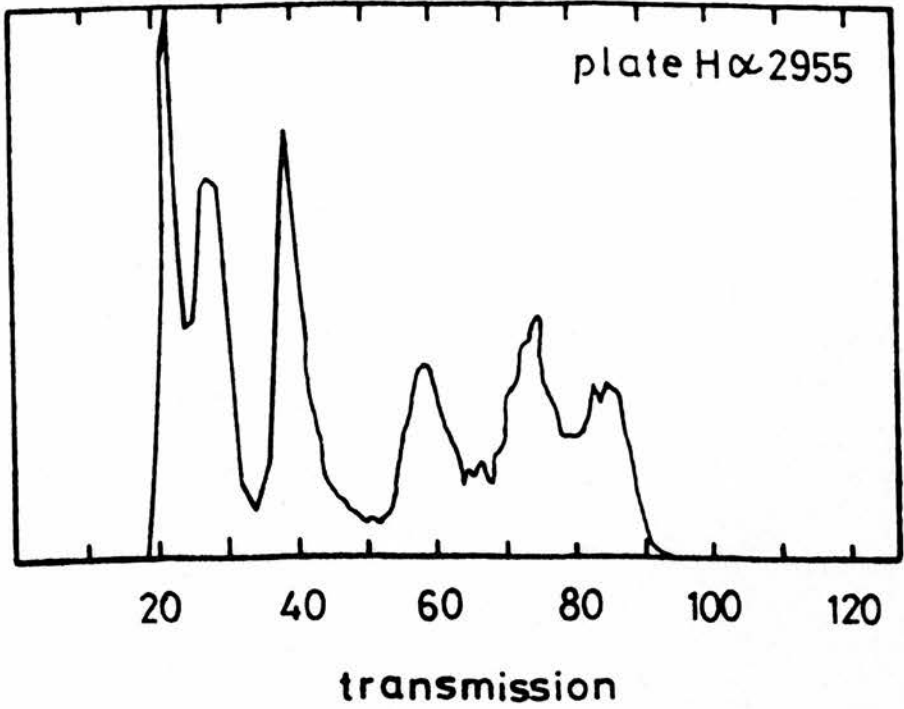
transmission

Figure 4.3. The Transmission frequency histogram for a scan through the calibration stepwedge of UKST plate Hα 2955.

Table 4-3

Step wedge data

Step	1	2	3	4	5	6	7		
log relative intensity	3.00	2.88	2.74	2.54	2.29	1.98	1.63		
Plate			COSMOS	Transmission				T_s	T_m
H 3223	(5)	(5)	6	10	23	58	105	79	12
2918	(5)	(5)	6	11	24	48	72	117	20
2886	9	12	20	43	81	-	-	109	23
2955	21	28	39	59	74	85	-	112	58
R1350	18	24	38	58	88	-	-	81	6

Notes

Bracketted values are at saturation levels.

T_s and T_m are the transmissions of the surrounding sky background to the galaxy and the minimum transmission encountered on the face of the galaxy away from the nucleus, respectively.

Errors: no more than one increment in transmission for low values of T, to no more than two increments for large T. (see Fig. 4-3)
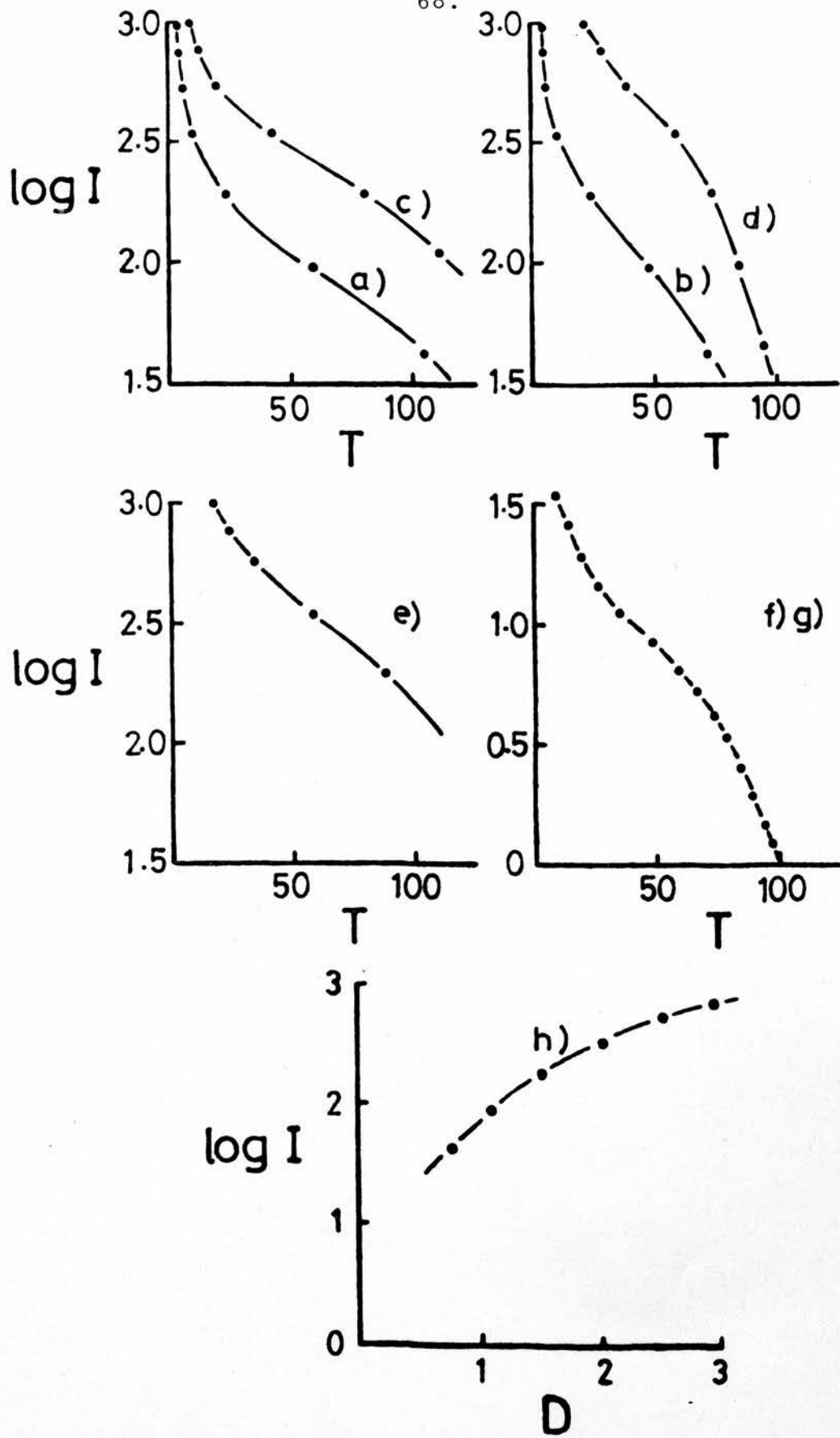
Figure 4.4. Transmission (or Density) to Intensity calibration
curves for

a) Hα 3223	b) Hα 2918	c) Hα 2886
d) Hα 2955	e) R1350	f) g) AAT 1402, 1404
h) Hα 2683		

Table 4-4

Step wedge data

Step	1	2	3	4	5	6	7	Fog	D_s	T_s	T_m	D_m
log (rel. int.)	3.00	2.88	2.74	2.54	2.29	1.98	1.63					
Plate	.... Macbeth density											
$H\alpha$ 2579	–	–	–	2.84	2.40	1.84	1.23	0.18	0.58	104	17	1.37
2595	–	–	–	2.75	2.38	1.76	1.06	0.18	0.67	50	10	1.37
2600	–	–	–	–	2.83	2.16	1.50	0.16	0.61	95	15	1.41
									0.63	92	33	1.08
									0.65	103	30	1.19
2606	–	–	–	–	2.65	2.06	1.38	0.17	0.49	105	23	1.15
2683	–	2.94	2.54	2.03	1.52	1.10	0.76	0.30	0.73	101	20	1.43
2871	–	–	–	2.84	2.48	2.04	1.53	0.38	1.23	82	33	1.63
2937	–	–	–	2.78	2.45	2.10	1.76	1.26	1.34	98	20	2.03

Notes

1) Fog is the density of developed unexposed plate.

2) Densities are accurate to an estimated 0.02.

3) D_s and T_s are the Macbeth density and COSMOS transmissions of the sky background to the galaxies of interest. (Hence three entries for $H\alpha$ 2600). T_m is the minimum transmission encountered on the faces of the galaxy and D_m the corresponding density. D_m is determined from T_m by application of equation (4.1), wherein 'c' has been determined from D_s and T_s.

side of the galaxy and comparing these with the average
COSMOS transmission levels in these areas. (Although Table
4.4 shows the means of these sky density (D_s) and trans-
mission (T_s) measurements, the resulting value of c is
negligibly different from the mean of four such comparisons!)

For the AAT plates a special calibration plate
was taken. The plate, from the same batch as the sky
exposed plates, is exposed to a spot sensitometer producing
an array of 15 spots in an arrangement as shown in Table
4.5a. The spots are of known relative intensity shown as
log B in Table 4.5a. The calibration plate was developed
with plate AAT 1402 though it should be applicable to plate
AAT 1404 also.

This calibration plate was also mapped by COSMOS
and measured with the 'MacBeth' and the results of these
measures appear in Table 4.5a.

Spot number 5 is seen to have an anomalous value
of the transmission that is hard to explain away, yet the
'MacBeth' density reading for that spot looks perfectly
normal. This may be an effect of the rather unfortunate
trend in the background density of this plate as illustrated
by the values of T_B and D_B in Table 4.5a. The background
gets more dense towards the left side of the plate so one
may expect spots 5, 6 and 15 to be measured too dark i.e.
too dense with respect to spots 1, 10 and 11.

The data has been adjusted slightly to try and
allow for this development error and the calibration of
the AAT plates will be based on Table 4.5b, shown also in
Fig. 4.4f.

Table 4-5a

Calibration Data for AAT plates

Spot	log B	T_i	T_B	D_i	D_B
15	1.542	9	99	1.505	0.615
14	1.407	13	104	1.330	0.605
13	1.277	18½	105	1.180	0.600
12	1.158	26	108	1.040	0.590
11	1.055	35	112	0.920	0.585
10	0.929	49	114	0.825	0.575
9	0.812	59	111	0.780	0.585
8	0.719	67	108	0.730	0.590
7	0.619	74	106	0.705	0.595
6	0.528	78	100	0.695	0.610
5	0.401	79	98	0.670	0.610
4	0.288	89	105	0.640	0.590
3	0.172	95	106	0.625	0.590
2	0.090	97	107	0.615	0.585
1	0.000	103	112	0.600	0.575

Notes

The arrangement of the spots on the plate is as follows:

15	14	13	12	11
6	7	8	9	10
5	4	3	2	1

: B is the normalised surface brightness (data source; AAO)

: T_i, T_B are the COSMOS transmissions of the spots and surrounding plate (mean of 4 measurements)

: D_i, D_B are the MacBeth densities of same.

Table 4.5b

Calibration of AAT Plates

Spot	log B	T_i
15	1.542	10
14	1.407	14
13	1.277	18½
12	1.158	25
11	1.055	34
10	0.929	48
9	0.812	58
8	0.719	67
7	0.619	75
6	0.528	80
5	0.401	85
4	0.288	90
3	0.172	95
2	0.090	96
1	0.000	101

Calibration Formulae

Previous formulae converting COSMOS transmission
into intensity have been achieved rather empirically, though
a particularly favourite form has been

$$\log I = k \, \log\!\left(\frac{T_C}{T-T_B} - 1\right) \qquad (4.2)$$

where I is the relative intensity, T the transmission and
k, T_C and T_B constants.

Some of the (T,I) calibration data of Table 4.3
were fit successfully to such formulae but others were not,
and so curves were simply sketched through the data points.
The (D, log I) data of Table 4.4 were all good straight line
fits except for that for Hα 2683 where the rather contrived
looking calibration formula in Table 4.6 is actually a good
fit to the data. Table 4.6 lists all the derived formulae.
The residual r.m.s. deviations in log I for the data points
about these lines are less than 0.01 for a) c) and e) and
less than 0.02 for the others.

4.5   *An Absolute Calibration?*

Using spectrophotometric data of HII regions in M83
obtained by Brand *et al.* (1980) with the Image Dissector
Scanner (Robinson and Wampler, 1972) on the Anglo-Australian
3.8 metre reflector, it would appear possible to convert the
relative intensities derived so far into absolute units.

The AAT/IDS system used, at that time, two 4".5 x
1".8 apertures through one of which was passed light from
the HII region and through the other of which was passed

Table 4-6

Calibration Formulae

Fig.	Plate	Formula
a)	Hα 3223	$\log I = 0.503 \log\left(\dfrac{130}{T-3} - 1\right) + 1.913$
c)	Hα 2886	$" = 0.447 \log\left(\dfrac{130}{T-4} - 1\right) + 2.364$
e)	R 1350	$" = 0.618 \log\left(\dfrac{130}{T} - 1\right) + 2.489$
	Hα 2579	$" = -0.56 \log T + 3.40$
	Hα 2595	$" = -0.53 \log T + 3.31$
	Hα 2600	$" = -0.50 \log T + 3.195$
	Hα 2606	$" = -0.52 \log T + 3.22$
h)	Hα 2683	$" = 2.12 \log (2.73 - \log T) + 2.09$
	Hα 2871	$" = -0.70 \log T + 3.47$
	Hα 2937	$" = -0.89 \log T + 3.05$

Notes

1) $I \equiv$ relative intensity

2) $T \equiv$ COSMOS transmission

3) The additive constants are arbitrary and simply convenient for the scaling.

4) Those indicated may be seen in Fig. 4-5.

5) In a) $\log I(T < 3) = \log I(T = 3)$ and

in c) $\log I(T < 4) = \log I(T = 4)$ - no such transmissions were actually measured in these plates.

6) Extrapolations are necessary faintward of
$I = 43$(Hα 3223), 46(Hα 2918), 196(Hα 2886)
96(Hα 2955), 196(R1350), 185(AAT plates)

nearby sky light. The rôles of the two apertures were reversed to allow for systematic differences and the sum of the sky readings subtracted from the sum of the HII region readings. Calibration spectra of standard stars allowed the absolute calibration of the HII region spectra.

The following two quantities may then be thought to be equivalent:

(A)   The convolution of such a spectrum with the trans-mission profile of the AAT Hα filter used to take the Hα photographs listed in Table 4.2 and with the spectral response of the 127-04 (or 098-04) emulsion used for these photographs (though in fact these emulsion responses are almost constant over the spectral region covered by the filter), and

(B)   the integrated 'intensity' obtained by placing a 4".5 x 1".8 mask over the photographic data of region from which the spectrum was taken. This is done by summing the relative intensities from each COSMOS datum around the nominal centre of the region (designated O in the scheme below) weighted according to the following scheme:

```
                       (N)
             D C C C C C C D
             B A A A A A A B
      (E)    B A A A O A A A B    (W)
             B A A A A A A B
             D C C C C C C D
                       (S)
```

where A = O = 1.0, B = 0.69, C = 0.18 and D = 0.12 for

the UKST plates, and A = O = 1.0, B = 0.16, C = 0.96 and

D = 0.15 for the AAT plates, except on a 19 x 7 grid. These

schemes break down the mask size into small squares one

COSMOS step on a side.

        The results of the application of these methods to

a)   the three nights on which AAT/IDS data are available,

       and

b)   plates Hα 3223 and Hα 2886

are shown in Table 4.7.

        The errors to be associated with the figures in this

table are assumed to be

a)   for method (A): the photon reception errors, which

       amount to factors of 20% at 2 units 8% at 10 units

       and 4% at 50 units, where one unit = 10^{-18} erg s^{-1}

       cm^{-2} $Å^{-1}$ ≡ fourteen 'Hα' photons per second on the

       AAT.

b)   for method (B): those associated with having offset

       the effective aperture from the nominal centre by

       one COSMOS pixel (≡8 μm ≡ 0".5 for UKST plates and

       16 μm ≡ 0".25 for the AAT plates), this error corres-

       ponding to the setting accuracy of the AAT.

       Plots of the method A results for each night against

the method B results for Hα 2886 are shown in Fig. 4.5.

Plots of the method B results for other plates against the

method A results show similar scattergram patterns, so much

so that one was encouraged to plot one set of Method B re-

sults against another and this is illustrated in Fig. 4.6

Table 4-7

"Intensities" of some HII regions in M83

Region	Method A Night			Method B Plate Hα	
	1	2	3	3223	2886
111	7.7	14.9	-	5223	8780
110	6.9	3.7	-	5249	8759
109	35.5	14.9	-	5601	9344
108	18.4	11.1	-	5240	8568
106	4.4	4.0	-	4272	6758
105	17.1	19.7	-	5910	9949
104	1.8	10.1	-	4915	7746
103	-	25.7	10.8	6354	10432
100	-	-	22.8	6471	10358
97	-	-	10.7	6173	9733
85	-	-	25.4	7716	14351
84	-	-	16.2	6802	10758
36	-	-	17.3	4891	7922
35	-	-	7.7	6972	11819
34	-	-	8.9	7302	13152
33	-	-	47.3	7444	13067
28	-	-	28.3	5987	9690
13	-	-	56.6	-	12172

Mean Errors in Method A : $\pm 20\%$ at 2 units

$\pm 8\%$ at 10 units

$\pm 4\%$ at 50 units

(1 unit $= 10^{-18}$ erg s^{-1} cm^{-2} Å^{-1})

Mean Errors in Method B : Hα 3223 $^{+1\%}_{-3\%}$

Hα 2886 $^{+2\%}_{-5\%}$

(units are on independent relative intensity scales)
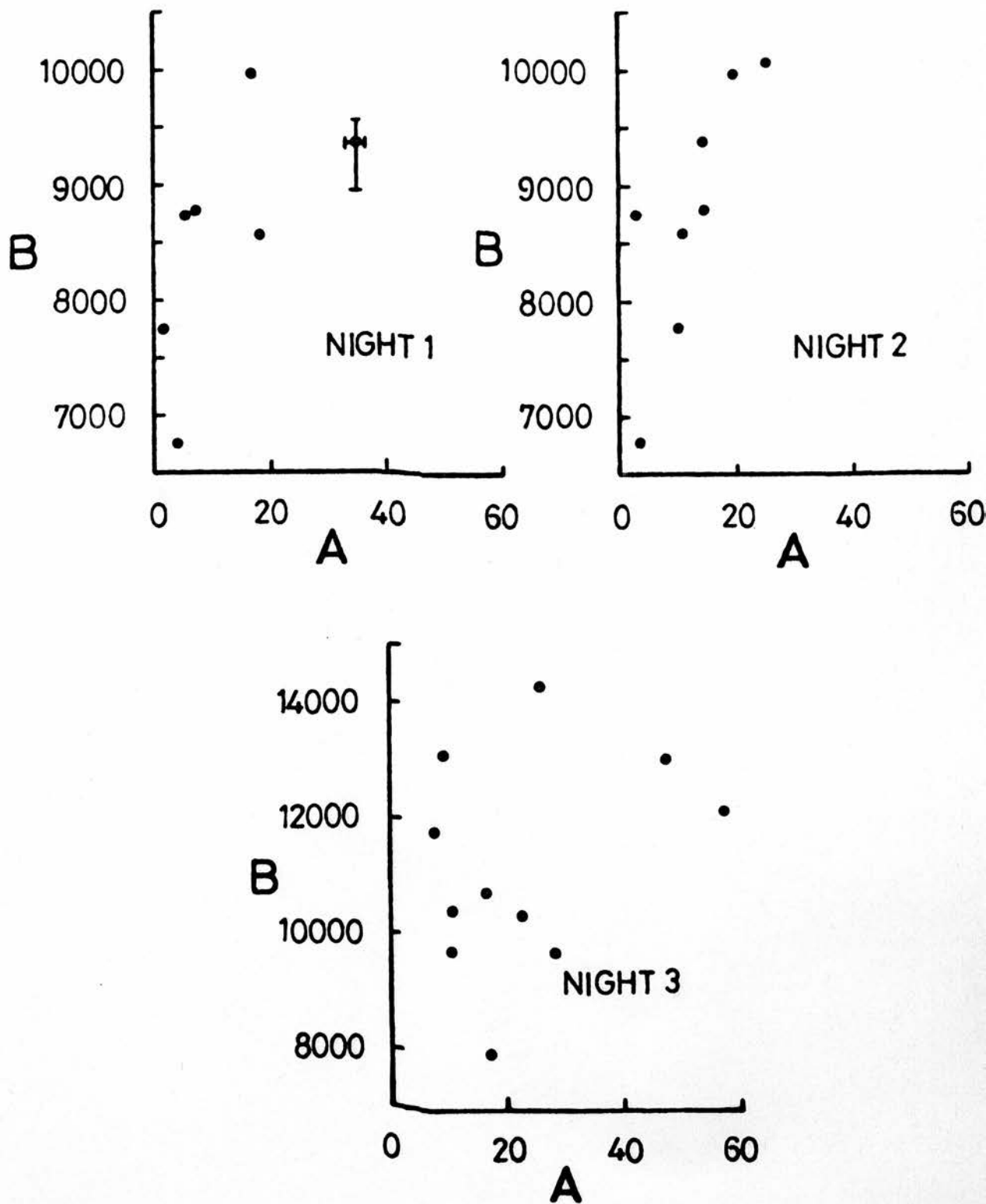
Figure 4.5. Calibration of photographic photometric measures of HII Regions in M83 taken from plate Hα 2886 (B) by spectro photometric data of the same regions obtained with the IDS/AAT system (A). (see text).
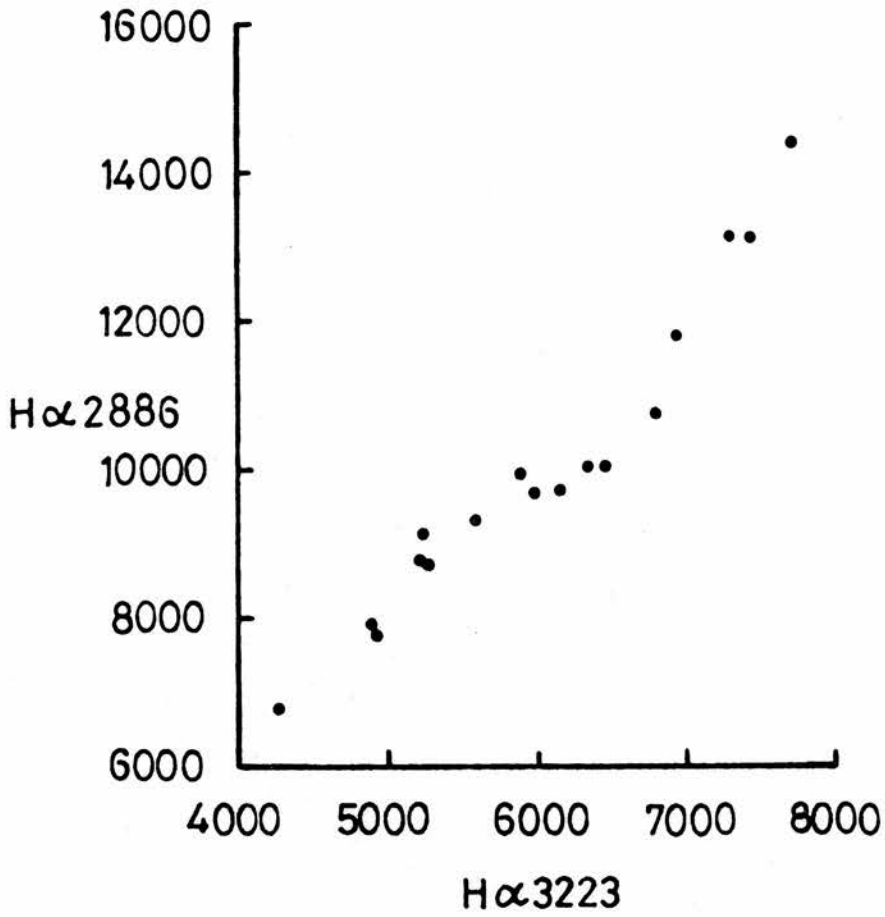
Figure 4.6. Method B results for 2 UKST Hα plates (see text for description of Method B).

for the data from plates Hα   3223 and Hα   2886.

Clearly there is reasonable agreement between the Method B results.

The reason for the lack of good agreement between the methods A and B is probably the variable observing conditions prevalent during the acquisition of the AAT/IDS data. Had the observed objects been point sources and the apertures large then we may have expected the two methods to agree. But the objects are diffuse and the apertures small compared with probable seeing conditions and with the objects themselves. Variable seeing during the IDS observations could explain the large variance between the Method A results for nights 1 and 2 thus:

a small isolated region would appear fainter in poor seeing, while

a faint region with bright neighbours would appear brighter in poor seeing.

The factor of six between method A results for region no. 104 may thus be explained - it does have brighter neighbours.

Average seeing conditions during the exposure of the plates are different, as seen from Table 4.2 but all regions are equally affected, so method B results should show some correspondence, as indeed they do (Fig. 4.6).

So - there is unfortunately no absolute calibration for this work, at present.

4.6   *Results I: Intensity Contour Maps*

Figs. 4.8 and 4.9 are intensity contour maps
showing M83 as it appears on plates Hα 2886 and AAT 1402.
(Compare these with the Hα photograph published by Dufour
et al. 1980). On these figures are indicated the four
principal reference stars listed in Table 4.8. The other
stars listed there and almost all the HII regions listed
in Table 4.9 are marked on Figs. 4.10 to 4.13 which show
the four quadrants of M83 in more detail. The lettered
plus signs in these figures mark the positions and sizes
of the areas photometered by Talbot *et al.* (1979).

The intensity levels used in the contouring are
equally spaced in the relative intensity scales derived
in Ch. 4.4. Not all contour levels near the very centre
of the galaxy are shown for sake of clarity.

Figs. 4.14 to 4.17 shows smaller areas of M83
at the greatest resolution available - in the previous
figures the COSMOS transmissions have been averaged over
16 and 4 pixels, resp., before the contours were calculated.
(This was necessary for computational reasons - see Appen-
dix C). These last figures also show the resolution
differences between the two sets of plate data. The re-
gions numbered 54 and 55 are well resolved on the AAT data
(Fig. 4.15), whereas they may have been considered as one
unit if the UKST plate scale had been smaller or the seeing
worse (see Fig. 4.14). Region number 60 was measured on
all the UKST Hα plates as a single region yet it clearly
resolves into two regions on the AAT plate (see Figs. 4.16
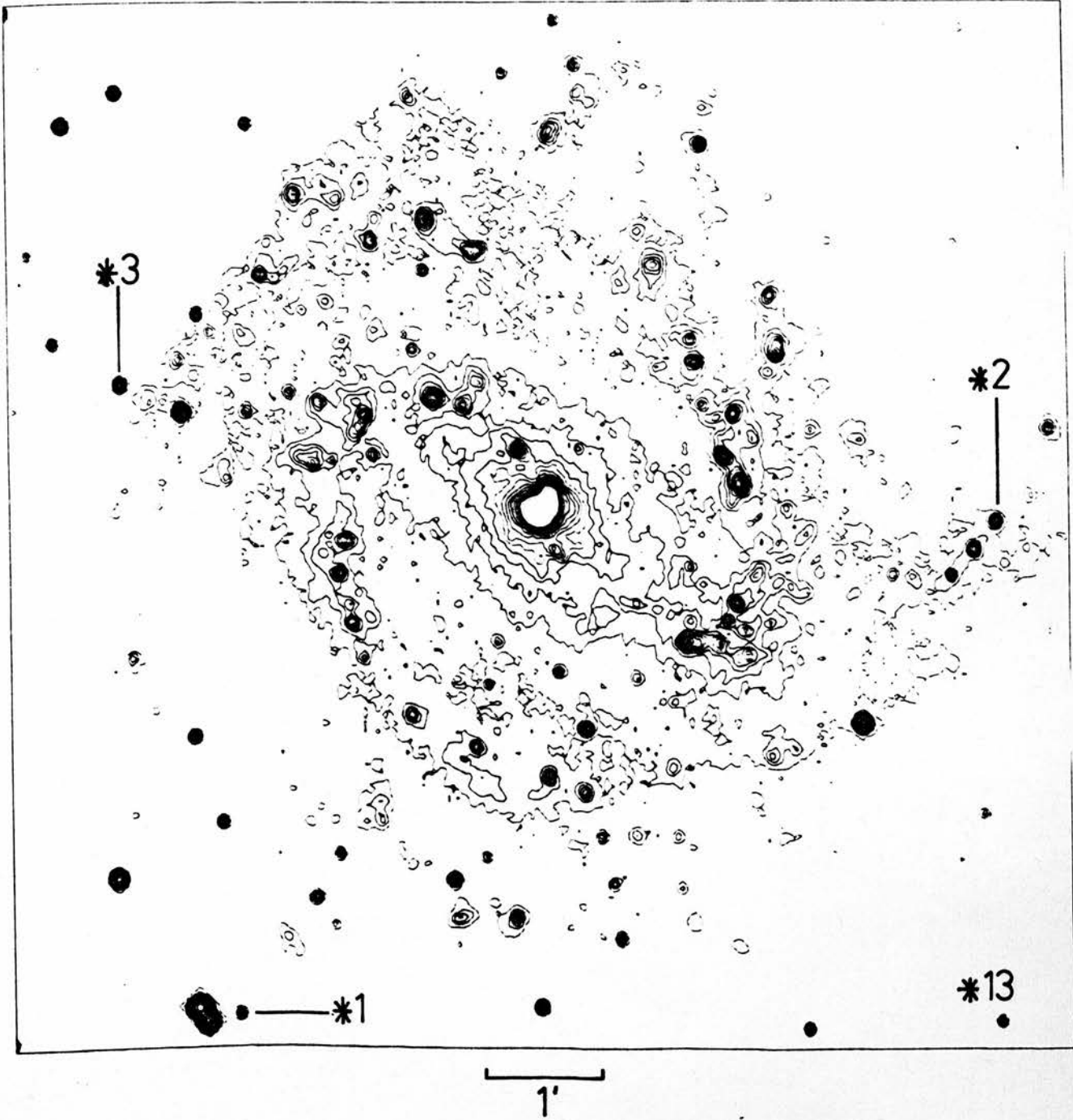
Figure 4.8. M83 on UKST plate Hα 2886.
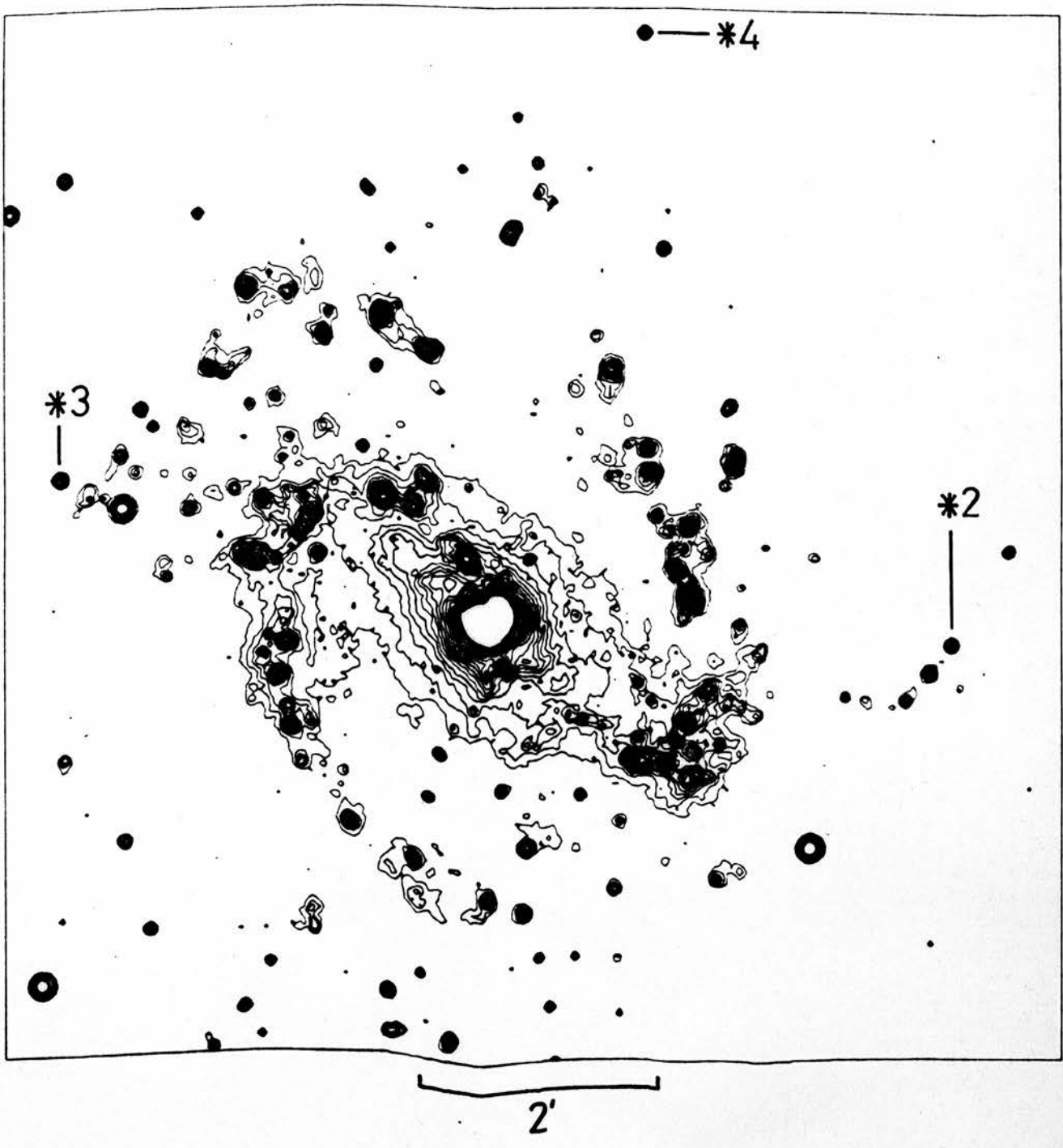
Figure 4.9. M83 on plate AAT 1402.

Table 4-8

Positions of stars in the field of M83

*	R.A.	(1950) Dec.
1	$13^h34^m23^s.8$	$-29°41'04"$
2	33 53.3	36 52
3	34 27.9	35 32
4	34 05.4	31 43

*	X	Y	*	X	Y
1	-160	-268	11	-20	226
2	234	- 9	12	28	-174
3	-219	64	13	234	-271
4	71	297	14	227	-163
			15	275	- 81
5	-187	48			
6	-179	99	16	344	58
7	-120	-206	17	289	88
8	-107	-183	18	-181	-122
9	- 48	-197	19	-168	-167
10	- 29	- 95	20	20	-118
			22	-141	214

X and Y are in arc secs with respect to the nominal
centre. X increases to the West, Y to the North.

Table 4-9

Positions of HII Regions in M83

No.	X	Y	No.	X	Y	No.	X	Y
1	5	-20	49	50	142	103	-105	- 36
2	9	-27	50	83	187	104	-101	- 54
3	42	-50	51	83	175	105	- 99	- 63
4	48	-52	52	20	214	107	- 94	- 81
6	83	-42	53	19	229	108	- 63	-112
7	76	-61	54	5	195	109	- 36	-128
8	74	-73	55	5	187	110	1	-144
9	90	-74	56	- 67	214	111	19	-151
11	104	-66	57	- 54	183	112	66	-138
12	117	-63	58	- 36	195	113	117	-132
13	100	-52	59	- 31	133	114	129	-128
14	95	-62	60	- 36	133	115	46	-173
16	122	-42	61	- 59	149	118	- 44	-214
17	128	-44	62	- 88	139	119	- 16	-215
18	136	-47	64	- 86	150	120	- 88	-155
19	136	-16	67	-126	170	121	- 85	-163
20	125	- 1	68	-144	120	124	-135	-224
22	138	38	69	-136	119	125	-129	-230
23	163	33	70	-124	102	127	-124	-167
26	191	-38	71	-111	106			
28	223	-24	76	-189	76	151	-141	-138
29	252	4	78	-204	54	152	- 24	- 71
30	250	-25	79	-196	43	153	- 87	91
31	238	-32	80	19	28	154	- 20	86
32	261	39	81	- 13	29	155	40	115
33	101	10	83	- 33	63	156	85	206
34	94	25	84	- 40	52	157	214	36
35	99	47	85	- 56	56			
37	98	36	88	- 92	47	300	-166	20
38	90	44	89	- 95	6	302	- 70	-193
						306	-118	-158
39	83	52	90	-115	53	310	-105	- 98
40	118	68	91	-130	58	318	-201	-108
41	122	79	92	-153	49			
42	122	82	95	- 88	26	320	-214	- 81
43	119	102	96	-109	23	321	- 88	195
						322	-115	168
44	79	86	98	-152	30	323	- 31	115
45	78	98	99	-163	13	325	- 51	153
46	70	99	100	-103	-19			
47	59	72	101	-111	-17			
48	58	125	102	-114	-26			

Positions are in arc seconds from the nominal centre.
X and Y increase to the West and North respectively.

Table 4-9 cont.

Identifications by other workers:

No.	BZC	DTJS
13	M	
28	P	V
32		VI
33	N	III
61		IV
81		I
84	L	II
85	K	
100	I	
103	H	
104	G	
105	F	
108	D	
109	C	
110	B	
111	A	

BZC ≡ Brand *et al.* 1980

DTJS ≡ Dufour *et al.* 1980
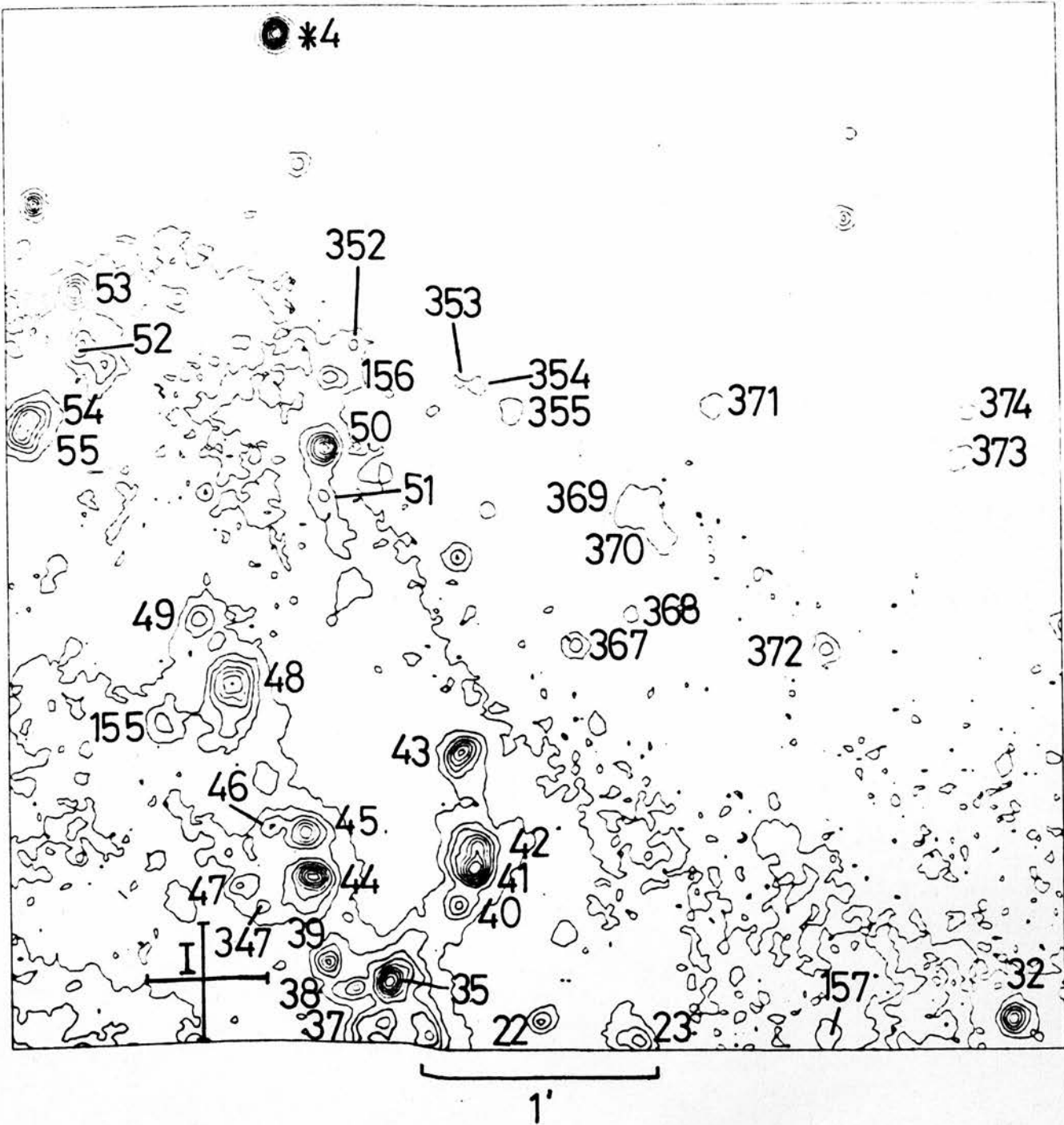
Figure 4.10. NW quadrant of M83 on UKST plate Hα 3223.
Region no. 43 is at 13^{h}34 02.2 −29°34 51 (1950).
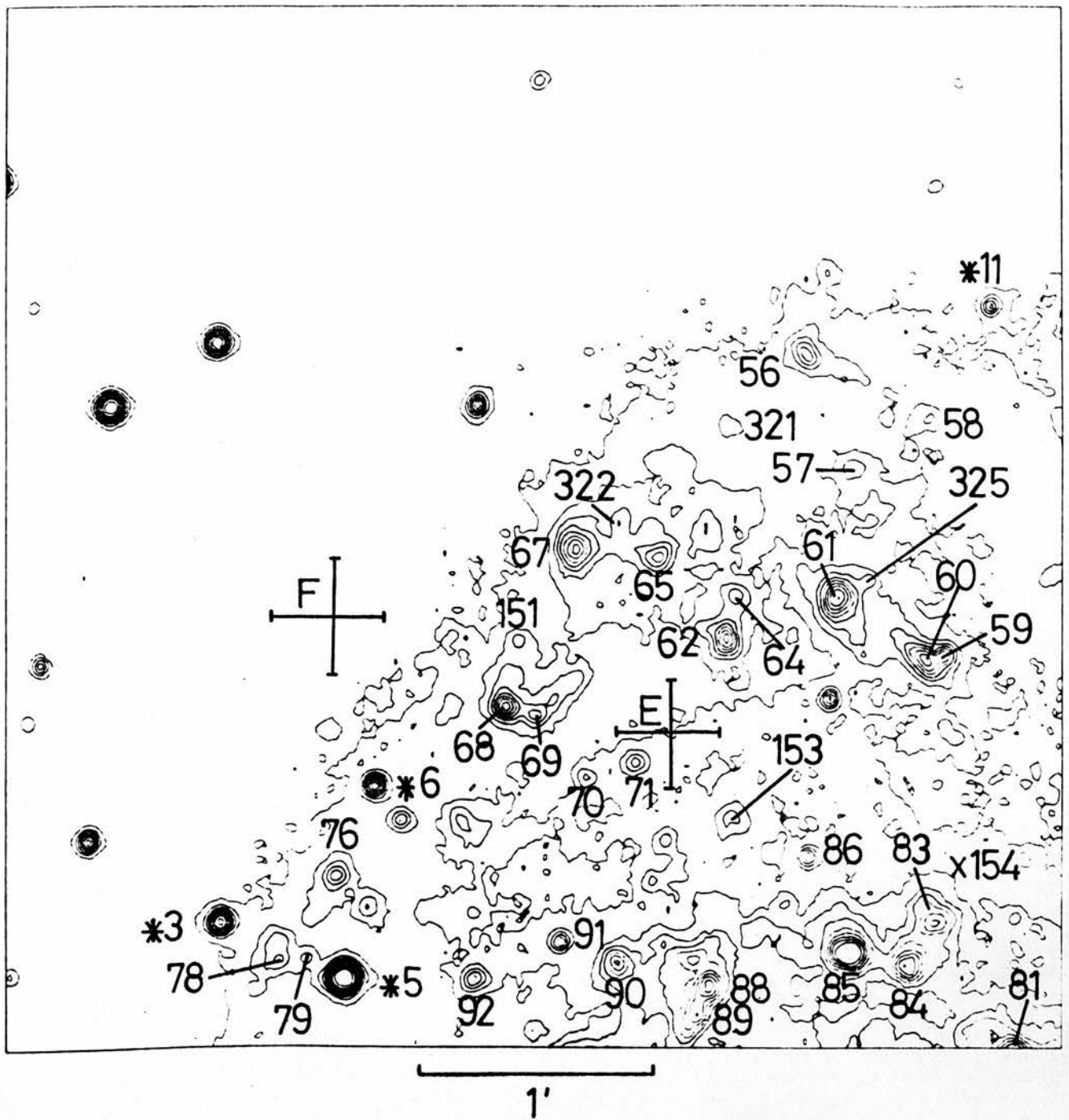
Figure 4.11. NE quadrant of M83 on UKST plate Hα 3223.
Region no. 67 is at 13^h34 20.8 -29^o33 55 (1950).
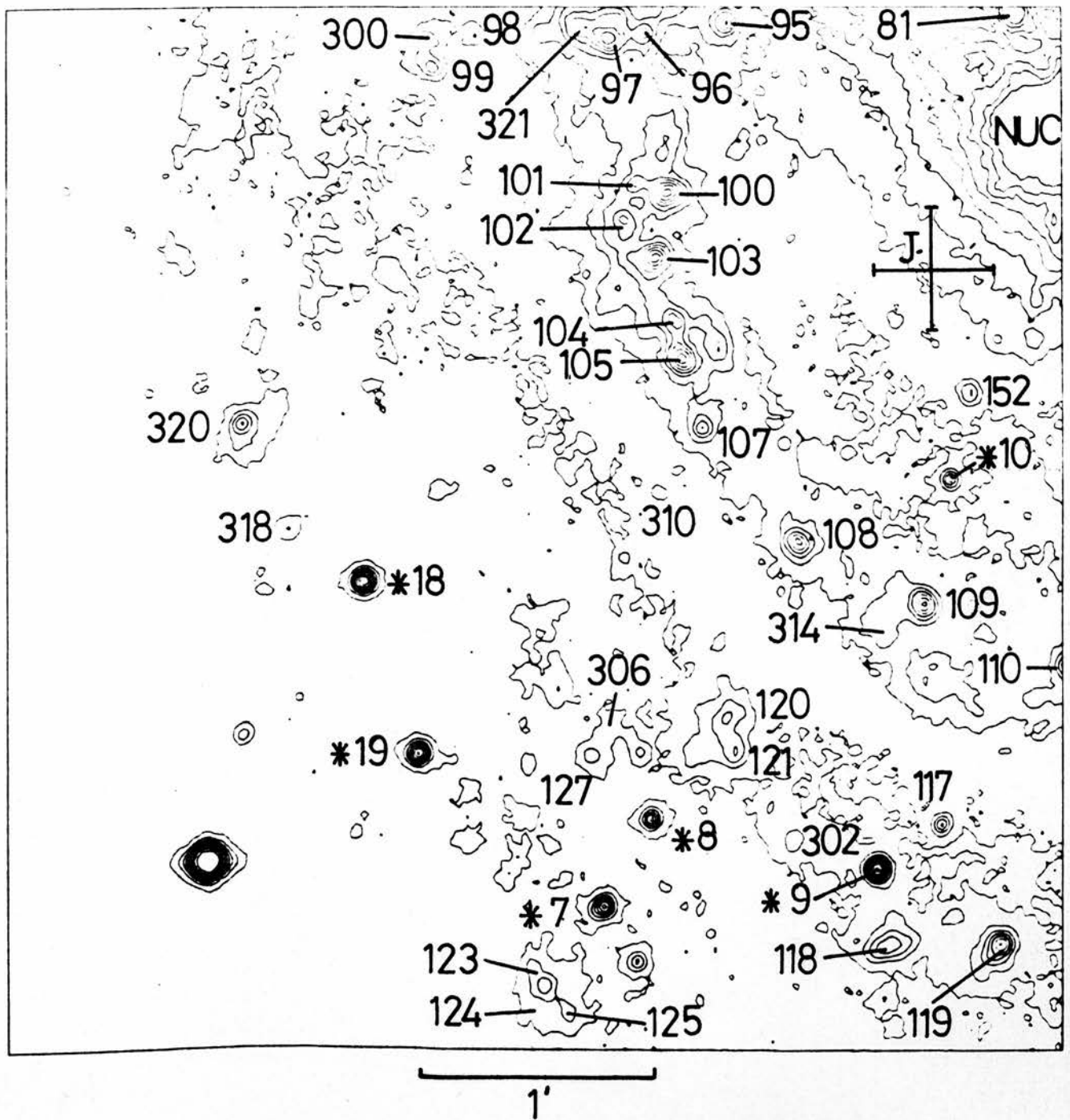
Figure 4.12. SE quadrant of M83 on UKST plate Hα 3223.
Region no. 108 is at 13^{h}34 16.8 -29°38 28 (1950).
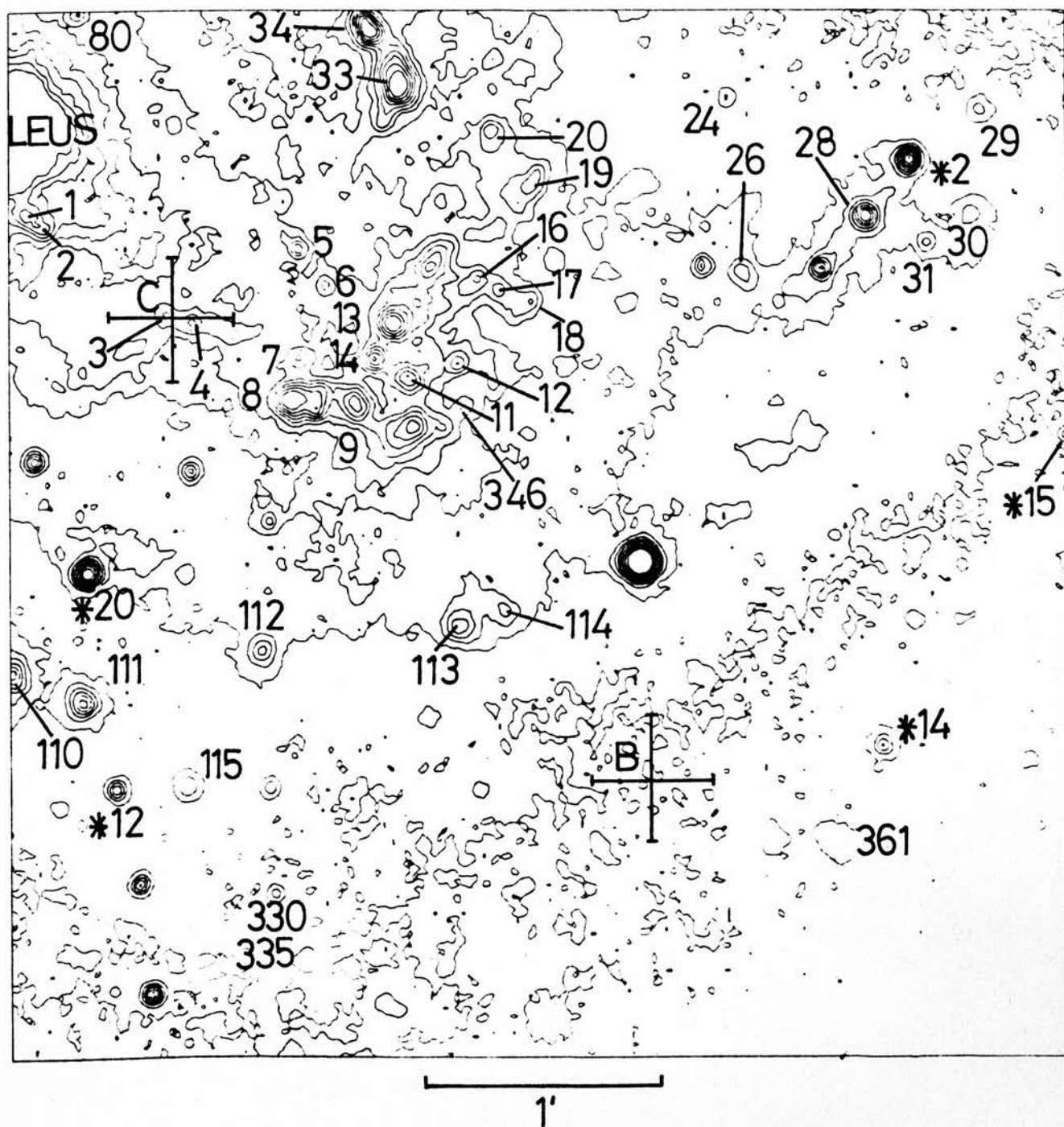
Figure 4.13. SW quadrant of M83 on UKST plate Hα 3223.
Region no. 113 is at 13^{h}34 02.6 -29°38 52 (1950).
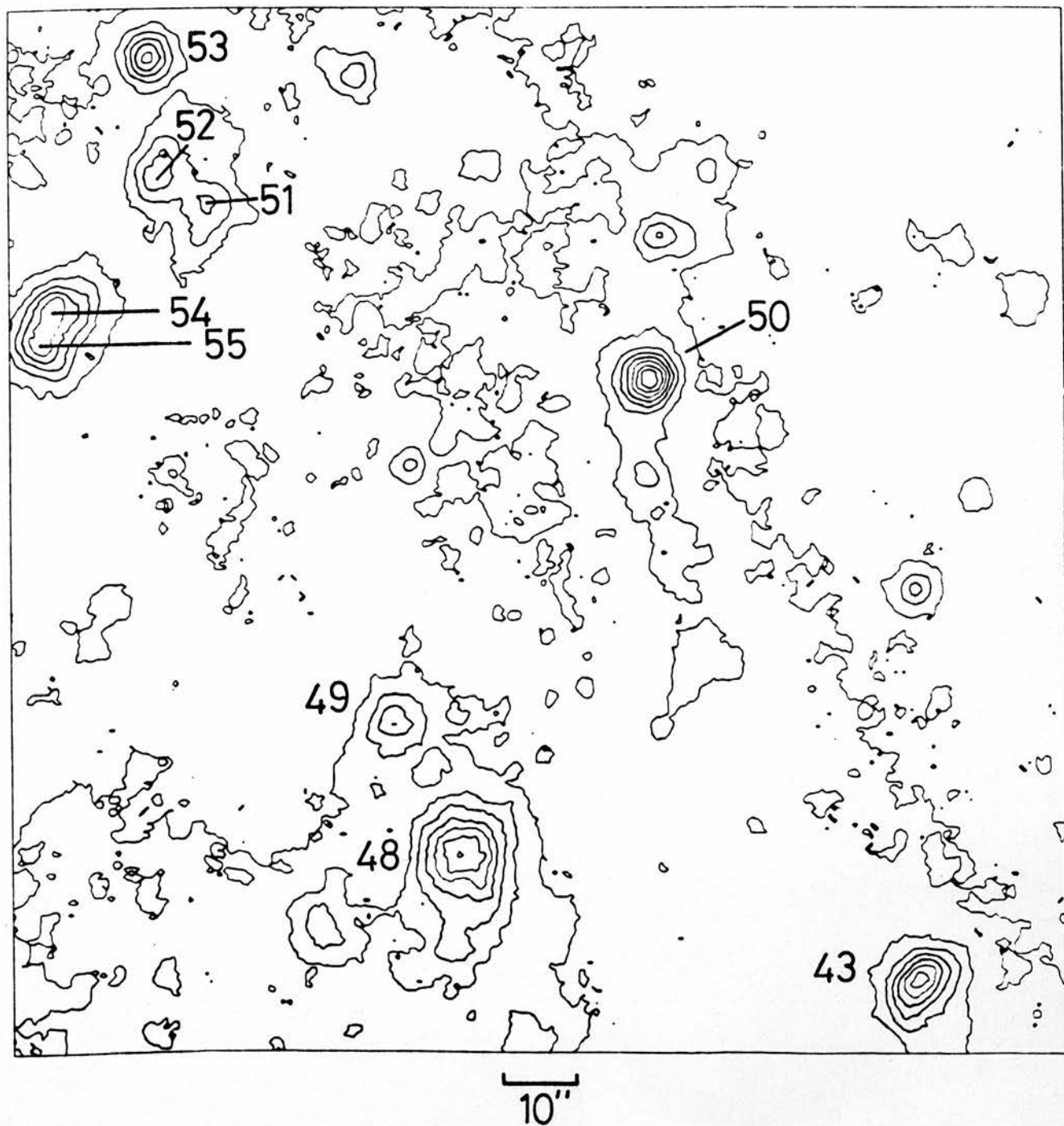
Figure 4.14. Part of M83 on UKST plate Hα 3223.
Region 50 is at 13^{h}34 04.7 -29°33 35 (1950).
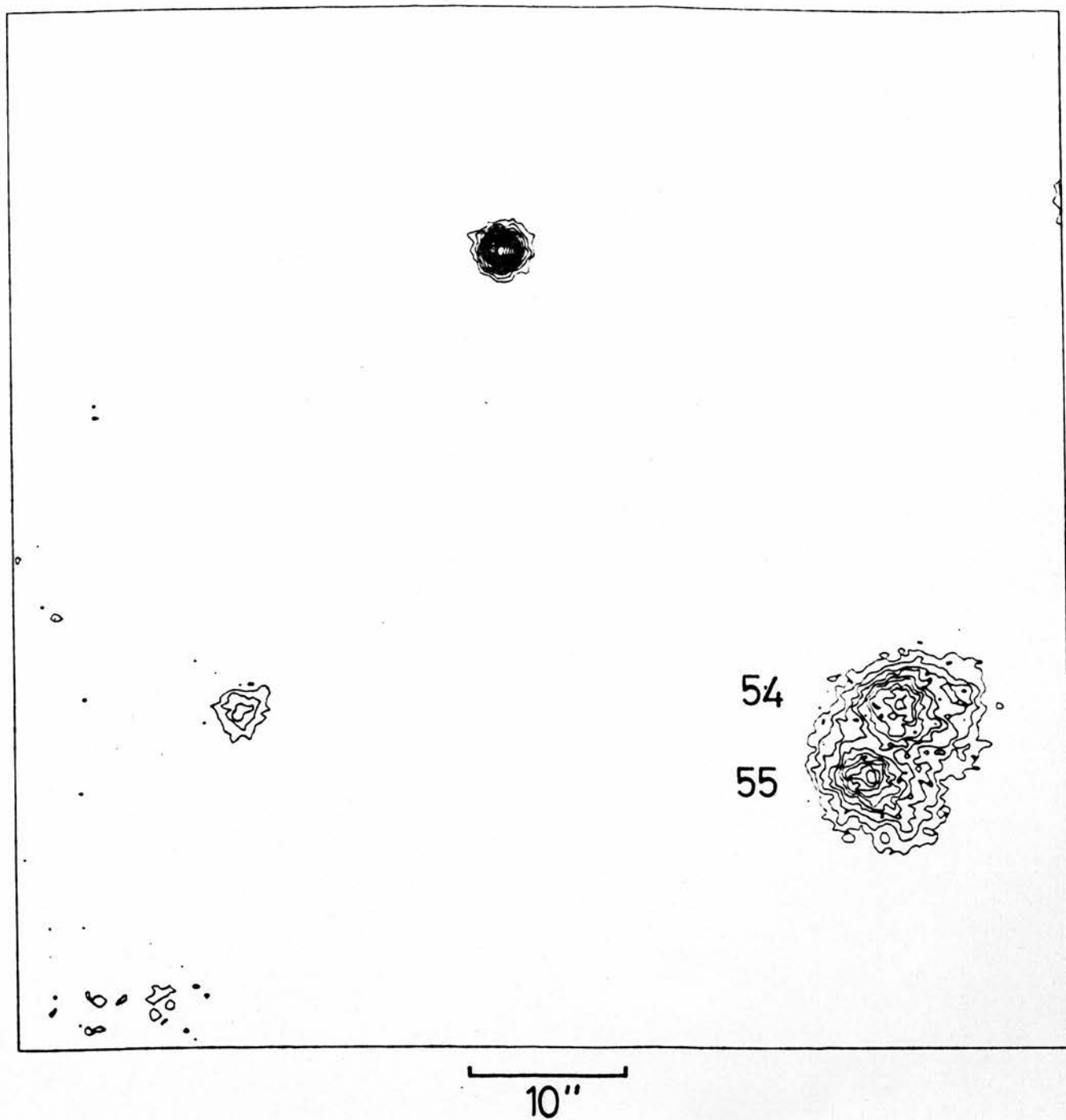
Figure 4.15. Part of M83 on plate AAT 1402.
Region no. 54 is at 13^h34 10.6 -29^o40 04 (1950).
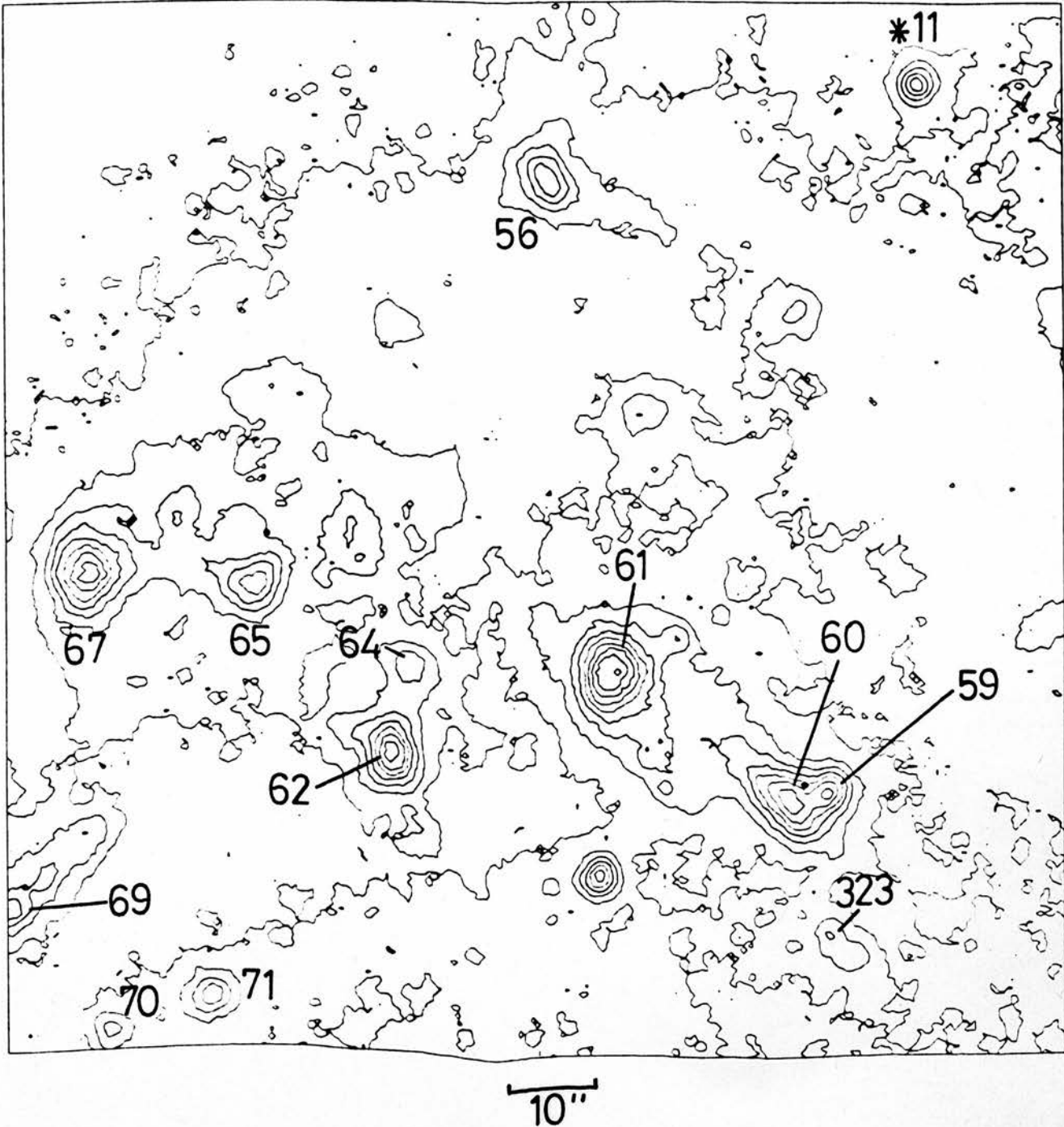
Figure 4.16. Part of M83 on UKST plate Hα 3223.
Region no. 61 is at 13h34 15.1 -29°34 09 (1950).
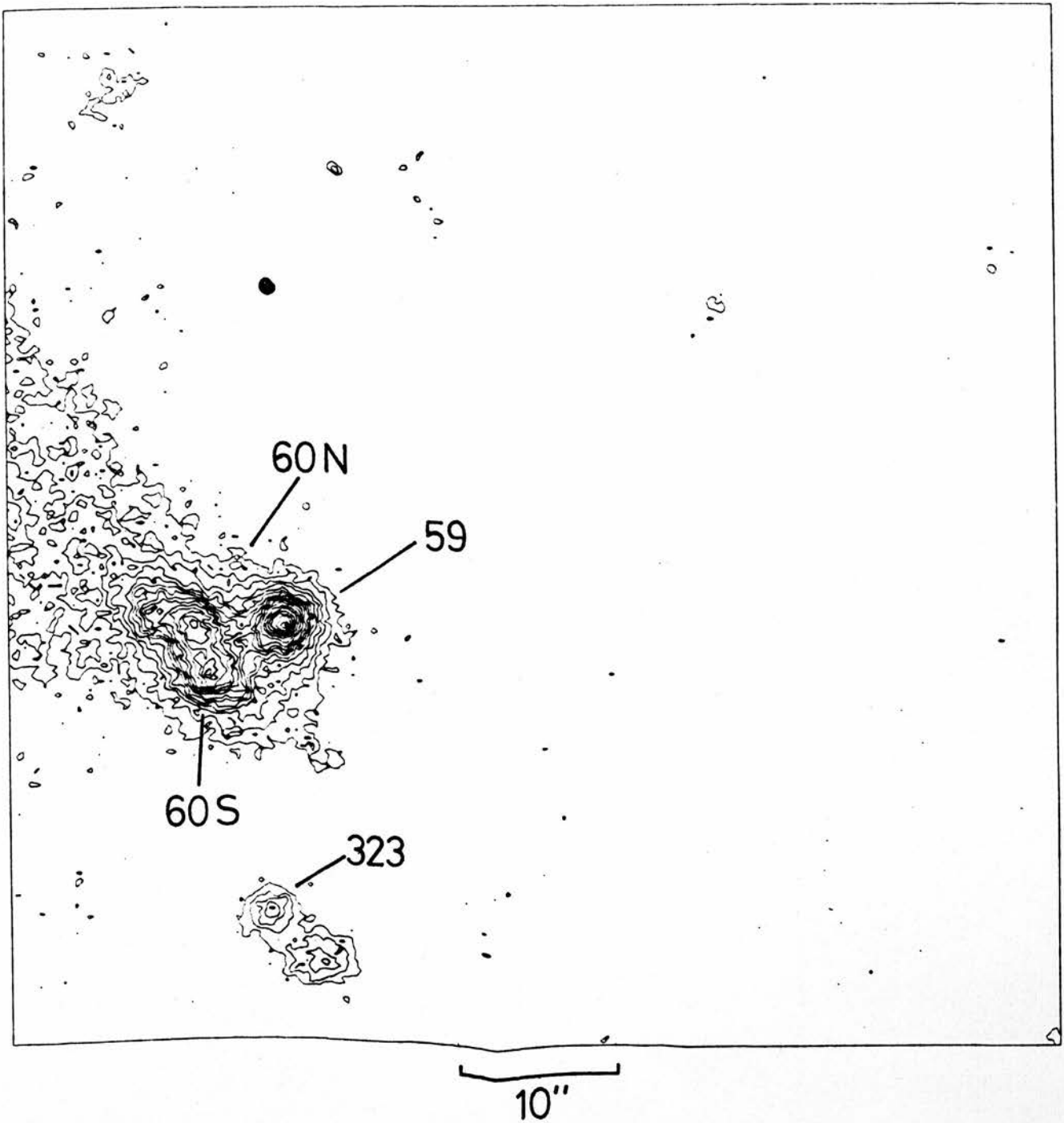
Figure 4.17. Part of M83 on plate AAT 1402.
Region no. 59 is at $13^h 34\ 15.5\quad -29°34\ 26$ (1950).

and 4.17).

The Hα plates were compared with a UKST blue plate
(J2382) to separate red and blue objects, and with the red
plate Rl350 to identify the HII regions from red stars
and clusters. The positions of objects so identified are
given in Table 4.9.

Many contour maps like those shown here were
drawn up, but clearly not all of them could be displayed.
Appendix E shows similar maps for the other galaxies in
the present sample.

4.7   *Results II - The Intensity Profiles of stars*

Let us consider the distortions affecting the
light from a point source at infinity on its way to form-
ing an image on a photographic plate.

The effect of atmospheric turbulence is to spread
the light about the mean path in a way most simply described
by a 2-dimensional gaussian (Dainty 1975).

The light is then subject to distortions within
the telescope and also within the photographic emulsion.
This combined residual spherical aberration and emulsion
spread function, f_a, has been determined for the UK Schmidt
telescope by Grubb Parsons Ltd. (1977). From their data
the mean radial distribution of intensity through the pro-
file formed by monochromatic $\lambda 6500$ light on a IIaD emulsion
was calculated and is shown as curve (1) in Fig. 4.18. The
radial distance of the peak is governed by the size of any
obscuration sitting on the optical axis, e.g. the plate
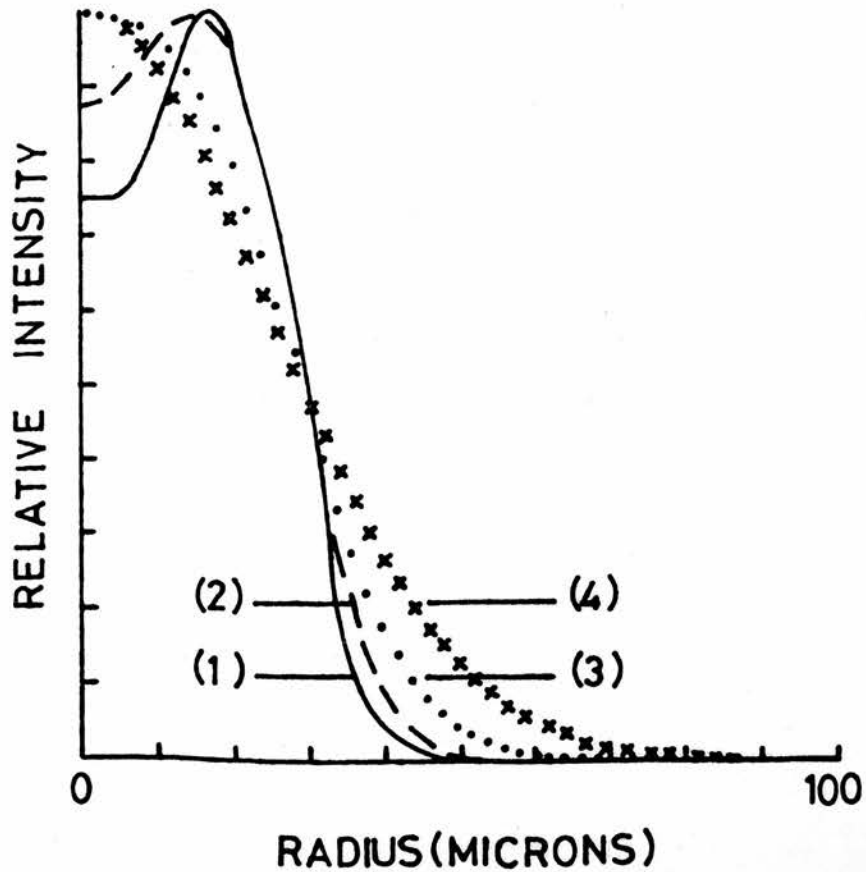
Figure 4.18. The residual spherical aberration and emulsion spread function, f_a, for the UKST with a IIaD emulsion, and the convolutions of f_a with gaussians

(1) f_a $(\lambda=6500\text{Å}, \text{IIaD})$: Grubb Parsons Ltd. (1977)
(2) $f_a \oplus g$ $(\sigma=\sigma_c/2)$ $(\sigma_c=10.7\mu\text{m})$
(3) $f_a \oplus g$ $(\sigma=\sigma_c)$
(4)   gaussian of same FWHM as (3)

holder, while the central depression deepens with increas-
ing emulsion resolution. The resolutions of the O98-O4,
IIaD and IIIaF emulsions, expressed in lines per mm, are
80, 100 and 200, respectively (Kodak 1973).

With the achromatic corrector plate in position
on the Schmidt Telescope, f_a is seen (Grubb Parsons Ltd.,
1977) to be a good approximation to a gaussian with $\sigma =$
18.3 μm. Of the UKST plates in Table 4.2 only Hα 3223
was taken with the achromat in place. The AAT plates were
taken through an achromatic corrector, also.

The photographic image of a star has an intensity
profile that is, then, the convolution, denoted $\oplus$, of the
seeing profile, g_s, with the function f_a; viz:

$$g_s \oplus f_a \equiv f_{sa} .$$

If this image is then scanned, as by COSMOS, with a moving
spot of gaussian profile g_c ($\sigma = \sigma_c = 10.7\mu m$) then the
digitised output of the image, in intensity units, is the
convolution

$$g_s \oplus f_a \oplus g_c \equiv f_{sac} .$$

This function may be determined by examining the COSMOS
data of stars, and may then be used to deconvolve other
(COSMOS-digitized) profiles, e.g. those of HII regions,
back to their intrinsic forms.

Since the intrinsic intensity profiles of HII
regions are probably exceedingly complex on a small scale
(see the intensity profiles presented by Kennicutt 1979a),
and since on the scale at which they are examined here

they may be more profitably approximated by some simple geometric functions, and since of more concern here is is the determination of some characteristic dimensions of such functions, a full 2-D deconvolution is not attempted here. Rather, the relationship between the characteristic dimensions of the intrinsic intensity profiles, the mean (digitized) star profile and the observed (digitized) image profiles are explored (Ch. 5.3).

Previous 'eyeball' techiques have used a simple deconvolution formula, like equation (3.1), to produce an intrinsic dimension for the HII regions (e.g. Sérsic 1960), but such techniques may be improved if the relationships between these dimensions and the profiles from which they came were better understood. It will be seen, for instance, that eyeball measures of stars correspond very well with the FWHM (Full Width at Half Maximum) dimension of (gaussian) stellar intensity profiles.

Other profiles in Fig. 4.18 simulate the plate images of stars photographed in 'seeing' of 1.55 arc secs (curve 2) and 3.10 arc secs (curve 3). Numerical values for 'seeing' refer to the diameter, d_{90}, of a circle enclosing 90% of the integrated intensity of a star profile. Its relation to other characteristic dimensions of a 2-D gaussian are

$$d_{90} = 4.31\sigma = 1.825 \text{ FWHM}.$$

At the plate scale of the UKST plates, i.e. 67.15 mm^{-1}, seeing of 3.1 arc secs produces the same loss in resolution as does the COSMOS spot, of FWHM 25.2 μm,

alone. For the AAT plate data, at a plate scale of 16''24 mm^{-1}, the degradation of the data by the COSMOS spot is equivalent to seeing of 0.75 arc secs.

Curve (4) in Fig. 4.18 is a gaussian of the same FWHM as curve (3). Convolutions of f_a with gaussians broader than that which produced curve (3) will be better approximations still to pure gaussians. Curve (3) may be considered either as the plate image profile of a star taken in seeing of 3.1 arc secs, or as the COSMOS digitized output of a star taken during diffraction limited seeing. Clearly the COSMOS images of stars taken during average seeing should be well approximated by gaussians, whereas plate image profiles of stars taken during good seeing may deviate somewhat from gaussians, as illustrated by curve (2) in Fig. 4.18.

Examination of COSMOS data on stars confirms the first of the above speculations. Fig. 4.19 shows some intensity profiles of stars on the plates of M83. The ones illustrated, and the ones chosen for measurement of their FWHM dimensions are unsaturated, yet not so faint as to be too noisy for practical purposes. The measurement of the FWHM is as descrived in Appendix F, and this dimension is given as d_1 in Table 4.10. The mean value of d_1 for each plate represents the function f_{sac} above.

In the case of plate 3223, where f_a is a good approximation to a gaussian, it has been possible to calculate the seeing, given variously as d_s and d_{90} in Table 4.10a, since

100.
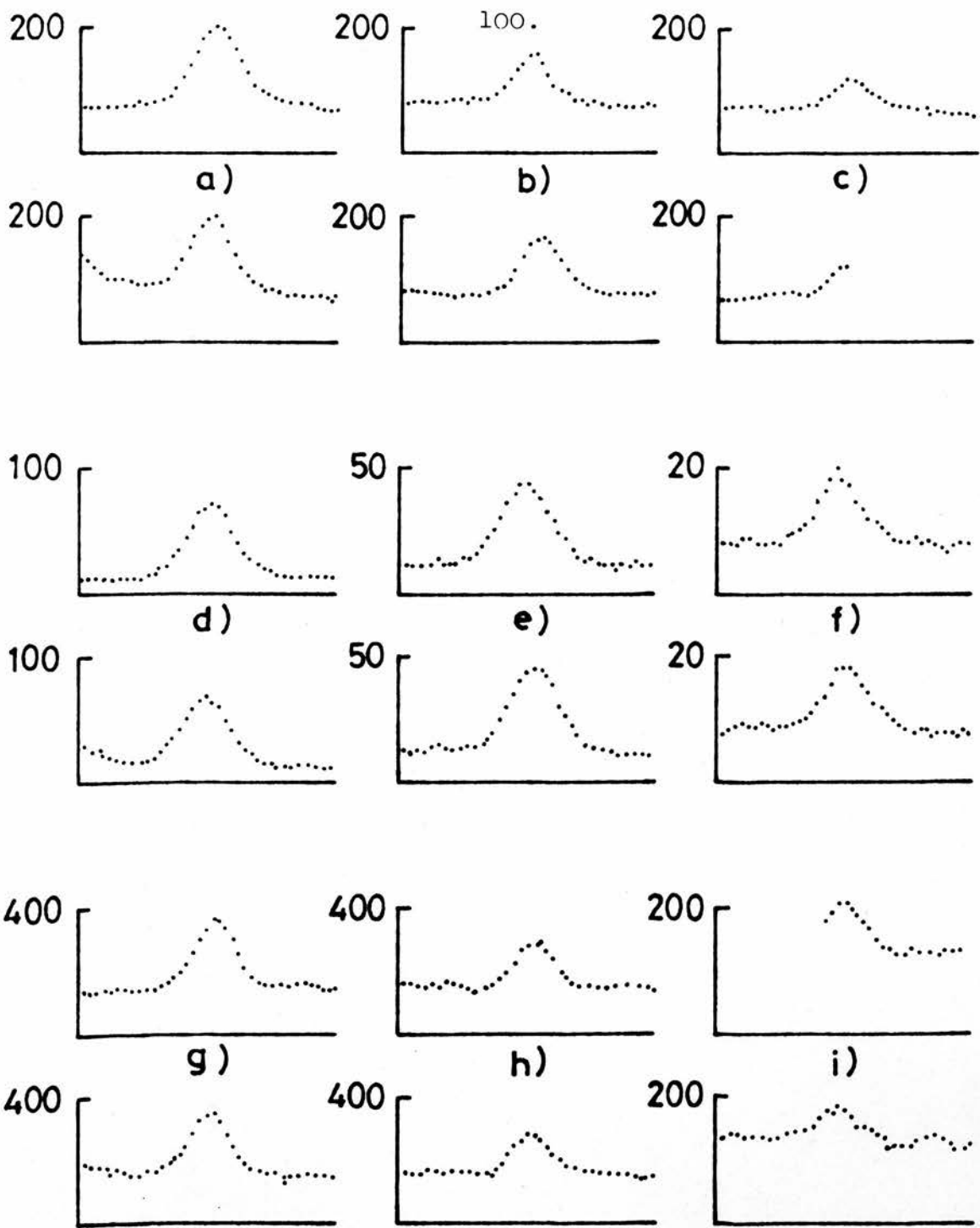
Figure 4.19. Stellar Intensity Profiles

a) *1   b) *11   c) *16   - Hα 3223
d) *1   e) *11   f) *16   - Hα 2918
g) *1   h) *11   i) *16   - Hα 2886

Upper plots are S-N, lower plots E-W.
Dots are 1 COSMOS step (8μm UKST, 16 μm AAT) apart.
Intensity scales relative.
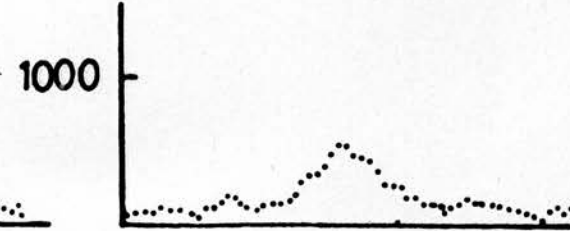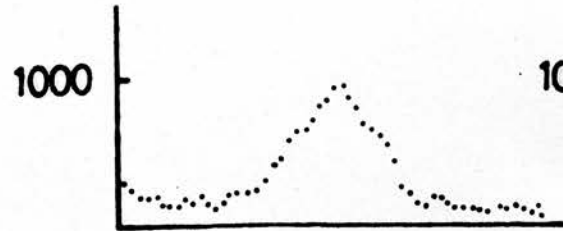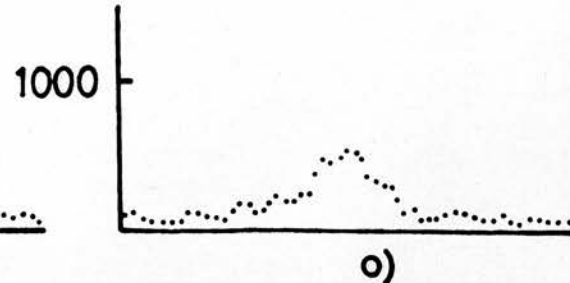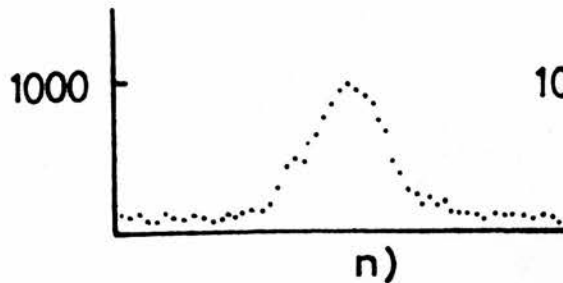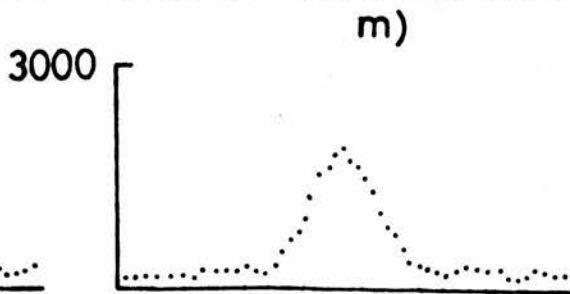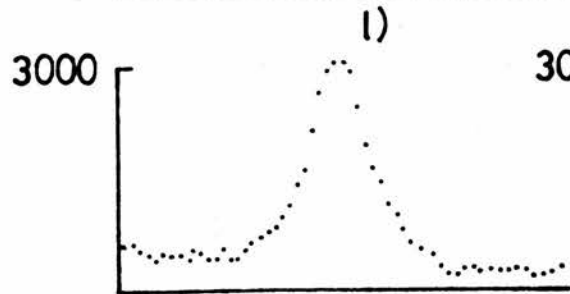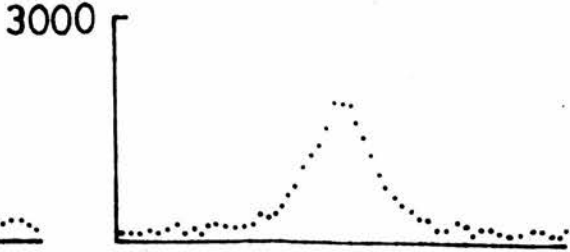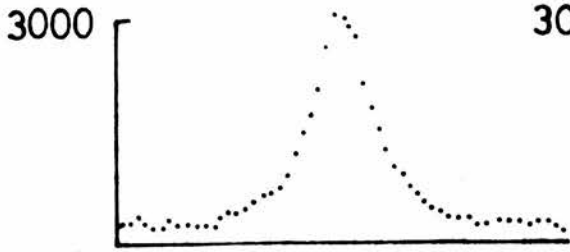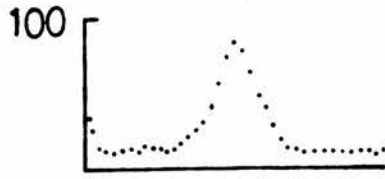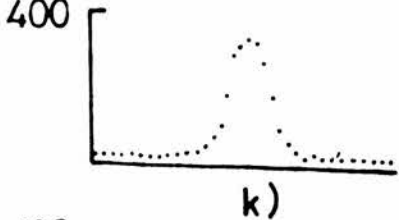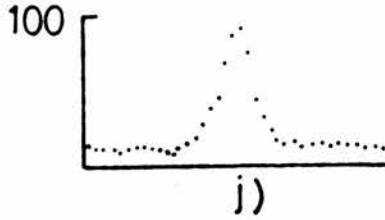
Figure 4.19 cont./...

j) *1 k) *9 – Hα 2955
ℓ) *1 m) *11 – AAT 1402
n) *1 o) *11 – AAT 1404

Table 4-10

Profile Widths of Stars in the field of M83

a) Plate Hα 3223

*	I_p	I_B	I_C	d_1	d_s	d_{90}	d_p	d_{xy}	$R_{p,xy}$
1	129	70	137	62	37	4.5	57	64	-0.12
8	112	75	119	59	31	3.8	53	65	-0.20
10	87	100	93	54	20	2.4	48	57	-0.17
11	94	74	100	57	27	3.3	51	52	-0.02
12	102	80	109	65	41	5.0	60	48	+0.22
13	130	69	138	64	40	4.9	59	52	+0.13
14	70	74	75	57	27	3.3	51	60	-0.16
15	56	76	60	58	29	3.5	52	60	-0.14
16	51	70	54	54	30	2.4	48	37	+0.26
17	60	70	64	61	35	4.3	56	62	-0.10
Means				59	31	3.7	54	56	-0.03
				+4	+8	+0.9	+4	+9	+0.17

Key:-

I_p : the relative intensity above local background

I_B : the relative intensity of local background

I_C : I normalised to I_C(*11) = 100

d_1 (μm): the FWHM of the COSMOS image

d_s (μm): d_1 'less' the COSMOS spot and telescope/emulsion distortions ($d_s^2 = d_1^2 - d_{ac}^2$, see text)

d_{90} ("): d_s expressed as "seeing"

d_p (μm): d_1 reduced to the plate, i.e. 'less' the COSMOS spot ($d_p^2 = d_1^2 - d_c^2$, $d_c = 25.2 μm$)

d_{xy} (μm): the xy diameter

$R_{a,b} = (d_a - d_b)/\frac{1}{2}(d_a - d_b)$

Notes:-

1) d_1 and d_{xy} are the means of the NS & EW measurements
2) d_1 is subject to errors of roughly 10% (see Appendix F)
3) d_{xy} is subject to errors of roughly 10% (see chapter 4.3).

Table 4-10 (cont.)

b) Plate Hα 2918

*	I	I_B	I_C	d_1	d_p	d_{xy}	$R_{p,xy}$
1	60	11	176	67	62	70	-0.12
8	48	11	141	64	59	65	-0.10
10	48	20	141	64	59	72	-0.20
11	34	11	100	72	67	64	0.05
12	40	13	118	66	61	63	-0.03
13	54	7	159	63	58	62	-0.07
14	22	8	65	69	64	61	0.05
15	17	9	50	65	60	64	-0.06
16	12	8	35	61	56	75	-0.29
17	18	8	53	69	64	70	-0.09
Means				66	61	67	-0.09
				±3	±3	±5	±0.10

c) Plate Hα 2886

*	I	I_B	I_C	d_1	d_p	d_{xy}	$R_{p,xy}$
1	225	134	165	58	52	45	0.14
8	192	140	141	56	50	45	0.11
10	137	170	101	51	44	58	-0.27
11	136	145	100	56	50	47	0.06
12	143	155	105	53	47	53	-0.12
13	226	130	166	57	51	58	-0.13
14	128	130	94	62	57	53	0.07
15	95	130	70	63	58	62	-0.07
16	74	130	54	59	53	50	0.06
17	89	130	65	66	61	55	0.10
Means				58	52	53	0.00
				±5	±5	±6	±0.14

Table 4-10 (cont.)

d) Plate Hα 2955

*	I_p	I_B	d_1	d_p	d_{xy}	$R_{p,xy}$
1	81	9	42	34	55	-0.47
2	294	15	49	42	60	-0.35
3	401	8	51	44	53	-0.19
5	948	15	74	70	77	-0.10
8	81	9	38	28	45	-0.47
9	319	18	42	34	45	-0.28
13	84	11	41	32	45	-0.34
18	307	11	46	38	60	-0.45
19	190	13	44	36	63	-0.55
20	548	15	<u>62</u>	<u>57</u>	<u>60</u>	<u>-0.05</u>
			49	42	56	-0.33
Means			±11	±13	±10	±0.17

e) Plate AAT 1402

*	I_p	I_B	d_1
1	2837	233	144
8	2682	233	138
10	1898	397	146
11	1661	233	151
12	1716	342	150

Mean d = 146 ± 5
$d_{xy}(*1) = 150$
$R_{p,xy}(*1) = -0.05$

f) Plate AAT 1404

*	I_p	I_B	d_1
1	881	94	198
7	900	120	184
8	646	94	178
10	510	120	147
11	413	120	146

Mean d_1 = 170 ± 22

Table 4-10 (cont.)

g) Plate R1350

*	I_p	I_B	d_1
1	1063	280	51
8	917	350	45
10	812	530	61
11	807	330	45
12	983	360	<u>50</u>
			50
			± 7

$$d_s^2 = d_1^2 - d_a^2 - d_c^2 \quad,$$

where d_a is the FWHM of f_a

and d_c is the FWHM of the COSMOS spot.

The average value of d_{90} of $3\overset{''}{.}7 \pm 0\overset{''}{.}9$ compares well with the estimated 1" - 2" of disk size and 1" - 2" of translation quoted in Table 4.2. Similar calculations could be attempted for the other plates, except that the above repeated application of equation (3.1) could not be applied exactly because of the non-gaussian nature of f_a for these other plates.

The quantity d_p in Table 4.10 is the size of the plate image of the star calculated from the COSMOS data by 'reducing' d_1 by the COSMOS spot size:

$$d_p^2 = d_1^2 - d_c^2$$

(Recall that so long as the seeing is not too good the plate image profile is approximately gaussian). d_p is compared with the size of the plate image as measured with the XY machine, d_{xy}, by the function

$$R_{p,xy} = (d_p - d_{xy})/\tfrac{1}{2}(d_p + d_{xy})$$

which is a normalised measure of the difference between d_p and d_{xy}.

The mean values of $R_{p,xy}$ are seen not to be significantly different from zero for any of the Hα plates of M83 for which XY measures were made. The eye (at least *my* eye) appears to measure the sizes of star images at their Half Maximum intensity levels.

Plate 2955 offers the most striking non-zero value of

$R_{p,xy}$, and an examination of the causes of this seems

necessary.

The calibration for this plate is extrapolated

faintward of transmission 85 (= a relative intensity of

96 on the scale derived here and shown in Fig. 4.4). All

the values of I_B for the stars in Table 4.10d are in this

extrapolated zone and three of these stars' intensity pro-

files lie wholly in this zone. None of the HII region

data lies wholly within the calibrated region of intensity, and

the usefulness of this plate seems now to be in serious

doubt.

Although there is a possible subjective effect

present in the XY measures of the stars on plate 2955, in

the sense that d_{xy} increases with I_p, the smallness of

$<d_1>$ is at least partly responsible for the large negative

value of $<R_{p,xy}>$. Confirmatory evidence comes from a

determination of the theoretical lower limit to d_1.

Estimates of the forms of f_a (O98-O4) and f_a

(IIIaF) were compiled according to the precepts specified

above, and convolutions of these profiles with gaussians

of various widths were performed on a computer and the

FWHM dimensions of the resulting profiles measured. When

the FWHM was measured at zero impact, i.e. from a profile

cut through the axis of symmetry of the (2-D) convolution,

the minimum values obtained were 58 μm from f_a (O98-O4),

58 μm from f_a(IIaD) and 59 μm from f_a(IIIaF). The measured

FWHM is found to decrease with increasing impact distance,

i.e. as the plane of the cut moves away from the axis of symmetry, although FWHMs of 50 μm would only be measured at impact distances of 25 μm or 3 COSMOS step sizes. All the measures of the stars on plate 2955 listed in Table 4.10d were made at zero impact - or as close to that as the 8 μm resolution of the COSMOS step size allows.

[It is partly this resolution problem that stimulated the evaluation of the errors induced in the FWHM measures by making them at non-zero impacts, i.e. not right through the centre of the image. In general, each FWHM was measured along the lines of the COSMOS data grid, although interpolation between the grid points was occasionally performed (see Appendix C). The error induced by misplacing the line of measurement by as much as one grid width, say, (8 or 16 μm) is shown in Fig. 5.10 to be negligibly small].

The conclusion to be drawn is that the smallness of the FWHM dimensions of stars on plate 2955 is due to an incorrect intensity calibration, at least, and as perhaps may have been anticipated, in the extrapolation of this calibration. Although the reduction of the data from this plate will be completed, no weight will be attached to its results in any final compilation.

Plate Hα 2918

Extrapolation of the intensity calibration for this plate was also necessary to cover the transmission measured in the star profiles. While the first six stars listed in Table 4.10b are data of class f (i.e. the peak intensity in their profiles lies within the calibrated

range of intensities but the assigned background intensity
does not), the remaining four are of class x data (i.e.
the entire intensity profile lies outside the calibrated
range of intensities). However, the fact that the mean
values of d_1 and $R_{p,xy}$ for the f class data set alone are
no different from those of the whole set ($<d_1(f)> = (66\pm3)\mu m$,
$<R_{p,xy}(f)> = -0.08\pm0.08$) hints that the mean values quoted
in Table 4.10b are the correct ones to use. Much of the
data for the HII regions on this plate falls into classes
f and x, and this is indicated for each region in Table
5.3.

Plate Hα 2886

All of the stellar data in Table 4.10c is of
class f. However, the mean values of d_1 and $R_{p,xy}$ do not
change significantly if the set is reduced to those of
largest values of I_p or I_B, so the mean values quoted may
be used with some confidence.

This rather unfortunate situation, of having
little wholly calibrated (class 'a') stellar data, arises
because of the calibration limitations, and because stars
with background intensities within the calibrated range
must tend to lie on the galactic face, where backgrounds
are more variable, where the associated peak intensities
are pushed up and where saturation therefore sets in at
fainter magnitudes, and where identification of stars as
such is more problematic.

Most of the HII region data for this plate is,
formally, of class 'f', but only just fails to make class

'a'. Assuming that the calibration does not go to awry immediately upon extrapolation, much of this data will be treated as class 'a'.

Plate R1350

A result of the convolutions performed above, during the analysis for plate Hα 2955, was that the FWHM at zero impact of a convolution of f_a with a gaussian is, to within 2%, independent of the particular form of f_a used. f_a is wavelength dependent, and the particular form shown in Fig. 4.18 is that for a wavelength of 6500Å. The effective wavelength of the R-plate is about 6650Å where the FWHM of f_a(IIaD) is given by Grubb Parsons Ltd. (1977) as 60 μm, though its shape is not given. Assuming it is similar to curve (1) in Fig. 4.18, but of FWHM 60 μm, and convolving it with a gaussian of the same width as the COSMOS spot, yields a function of FWHM 60 μm, which may be assumed to be insensitive to the exact form of f_a. The measured values of the FWHM of the stars on plate R1350 are considerably smaller than this, yet there are no intensity calibration problems or non-zero impact measurements to explain this.

CHAPTER 5

THE INTENSITY PROFILES AND SIZES OF HII REGIONS

In the previous chapter we saw how the various
smoothing processes that affect an image on a plate could
be quantified. In this chapter the images of HII regions
will be examined and the processes required to obtain their
intrinsic forms will be determined. Their intrinsic dimen-
sions will then be used in producing a size distribution
for the HII regions of M83.

5.1   *Results III: The Profiles of HII Regions*

The HII regions of M83 were ranked by peak inten-
sity above local background and Fig. 5.1 shows E-W (upper)
and S-N (lower) intensity profiles through the six bright-
est as they appear on plate 2886. The intensities are in
relative units, as derived separately for each plate in
Ch. 4.4, and the zero of this scale is at the 'origin' of
the plots. Fig. 5.2 and 5.3 show profiles through the
same regions but as they appear on the AAT plates. Figs.
5.4, 5.5 and 5.6 show profiles through more HII regions,
taken from plates 3223, 2886 and 1402, respectively.
The regions were sampled unbiasedly to illustrate HII
regions of decreasing brightness: the last region dis-
played in these three figures, region no. 96, is ranked
no. 100.

The figures should be compared for interplate simi-
larities and differences. The most notable differences
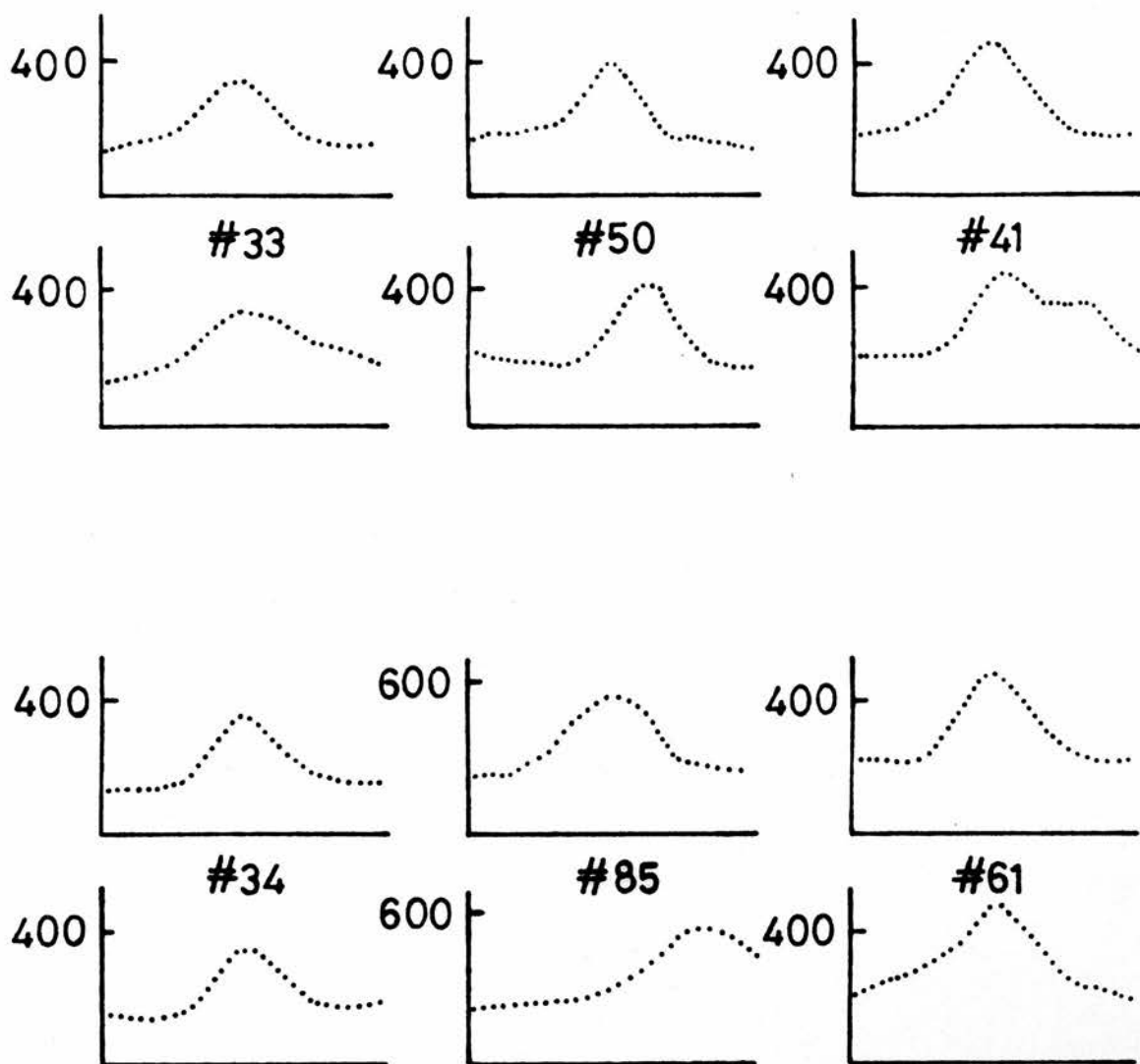
Figure 5.1.   E-W (upper) and S-N (lower) intensity profiles through
the six brightest HII regions in M83.   Data from UKST
plate Hα 2886.   Dots are one COSMOS step apart.   (=0".54
for UKST plates, 0".26 for AAT plates).
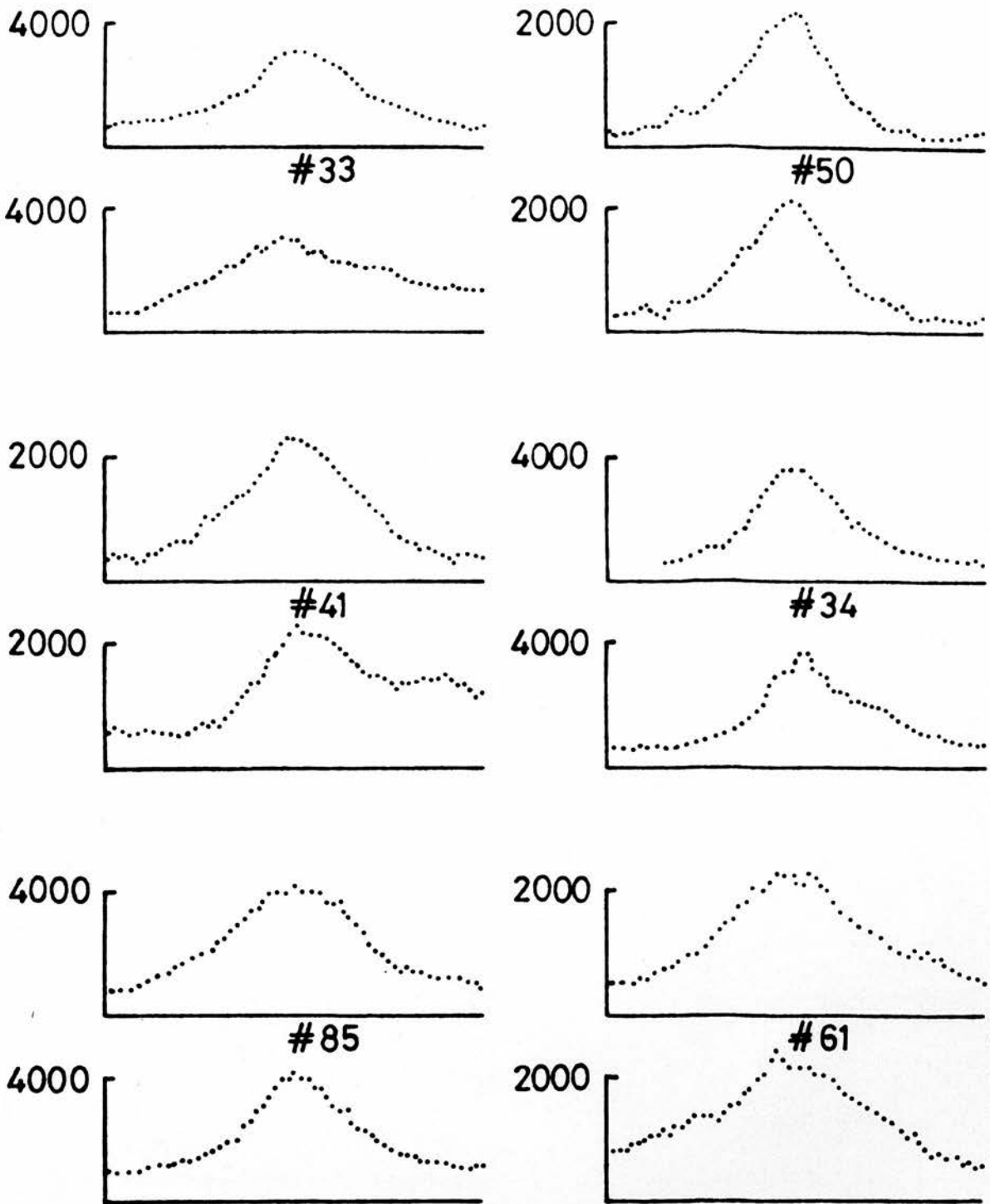
Figure 5.2. E-W (upper) and S-N (lower) intensity profiles through the six brightest HII regions in M83. Data from plate AAT 1402. Dots are one COSMOS step apart. (=0".54 for UKST plates, 0".26 for AAT plates).
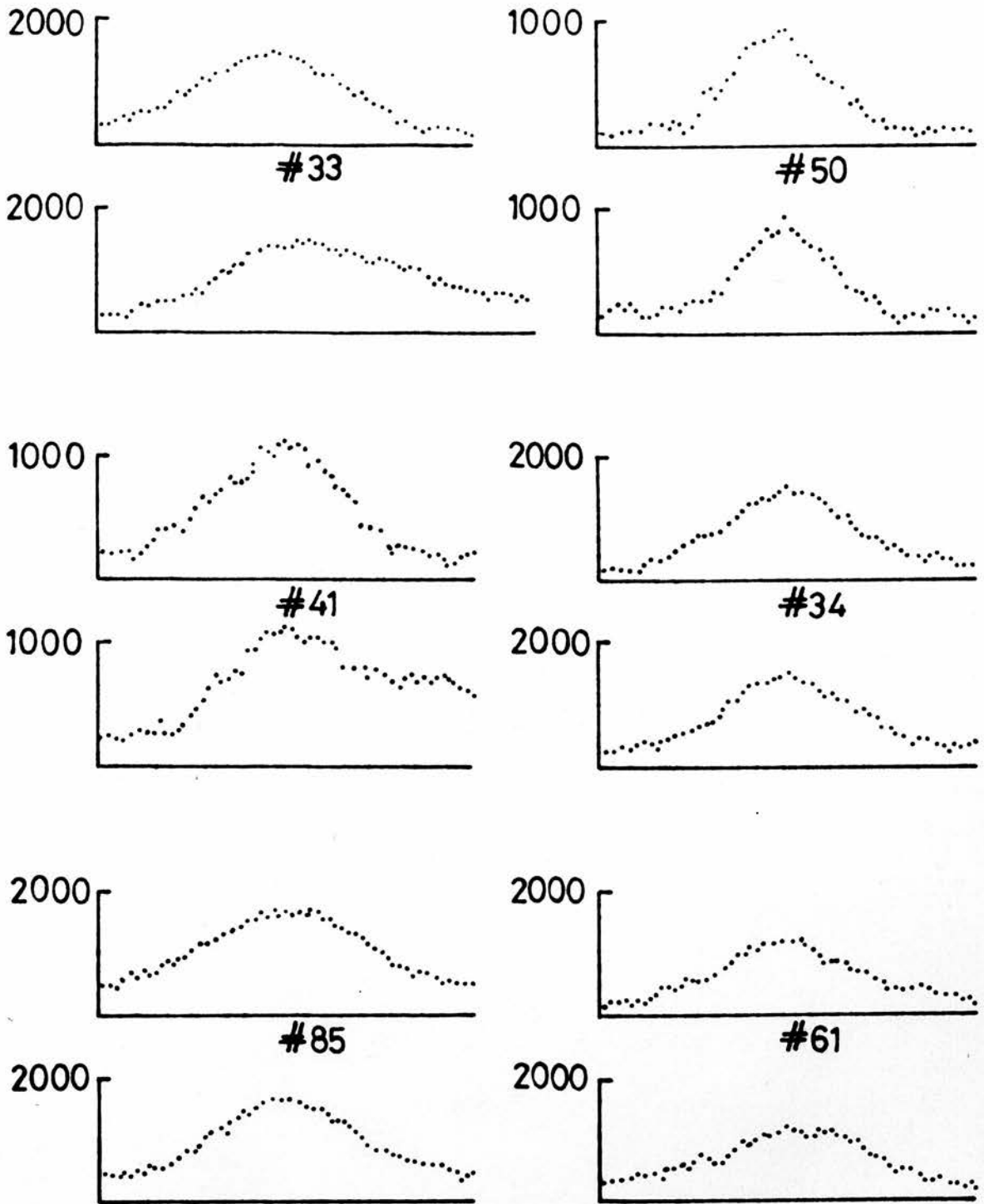
Figure 5.3. E-W (upper) and S-N (lower) intensity profiles through the six brightest HII regions in M83. Data from plate AAT 1404. Dots are one COSMOS step apart. (=0".54 for UKST plates, 0".26 for AAT plates).
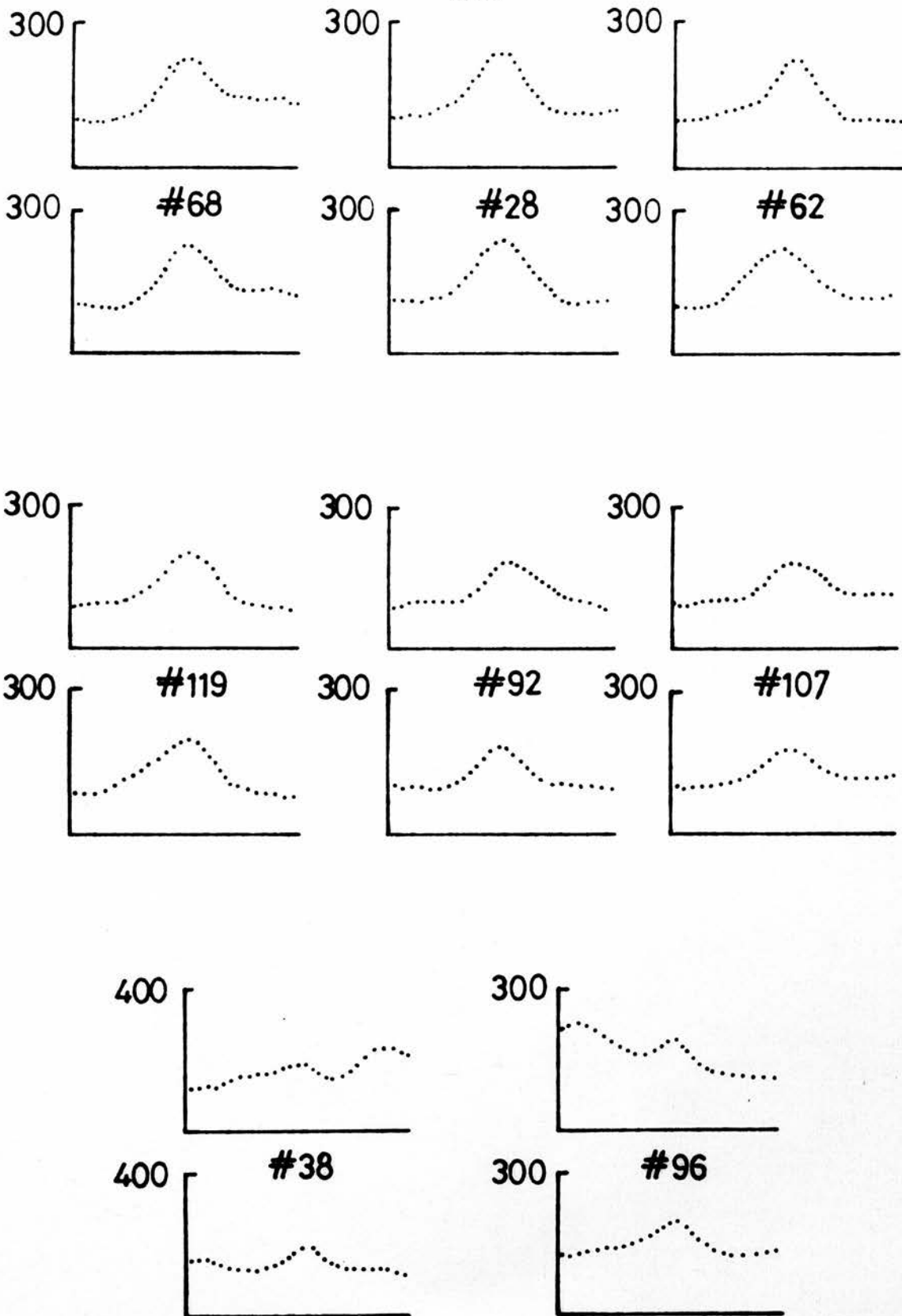
Figure 5.4. Intensity Profiles of HII regions in M83. Data from plate Hα 3223. Upper plots are E-W lower plots S-N. Dots are 1 COSMOS step apart.
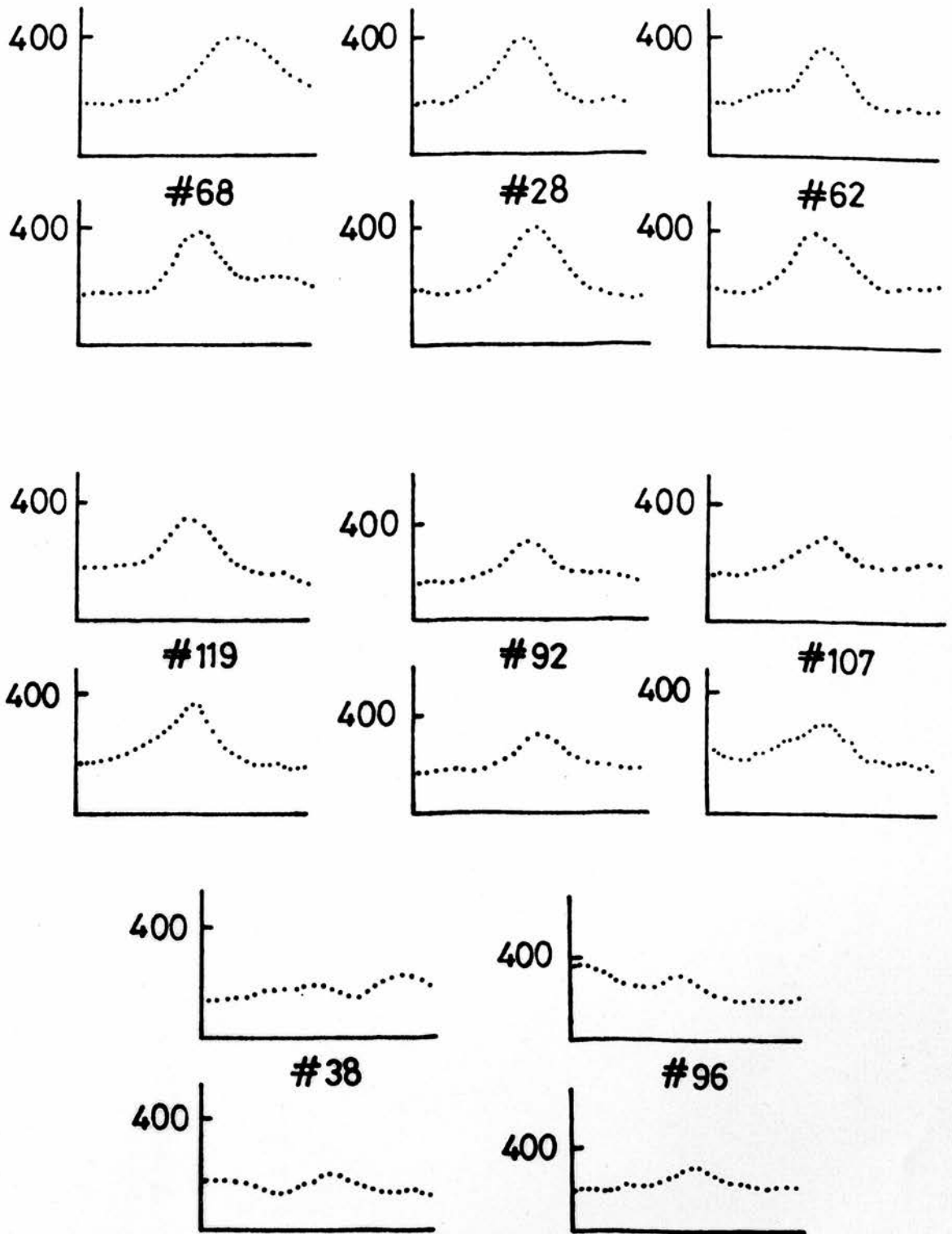
Figure 5.5. Intensity Profiles of HII regions in M83. Data from plate Hα 2886. Upper plots are E-W lower plots S-N. Dots are 1 COSMOS step apart.
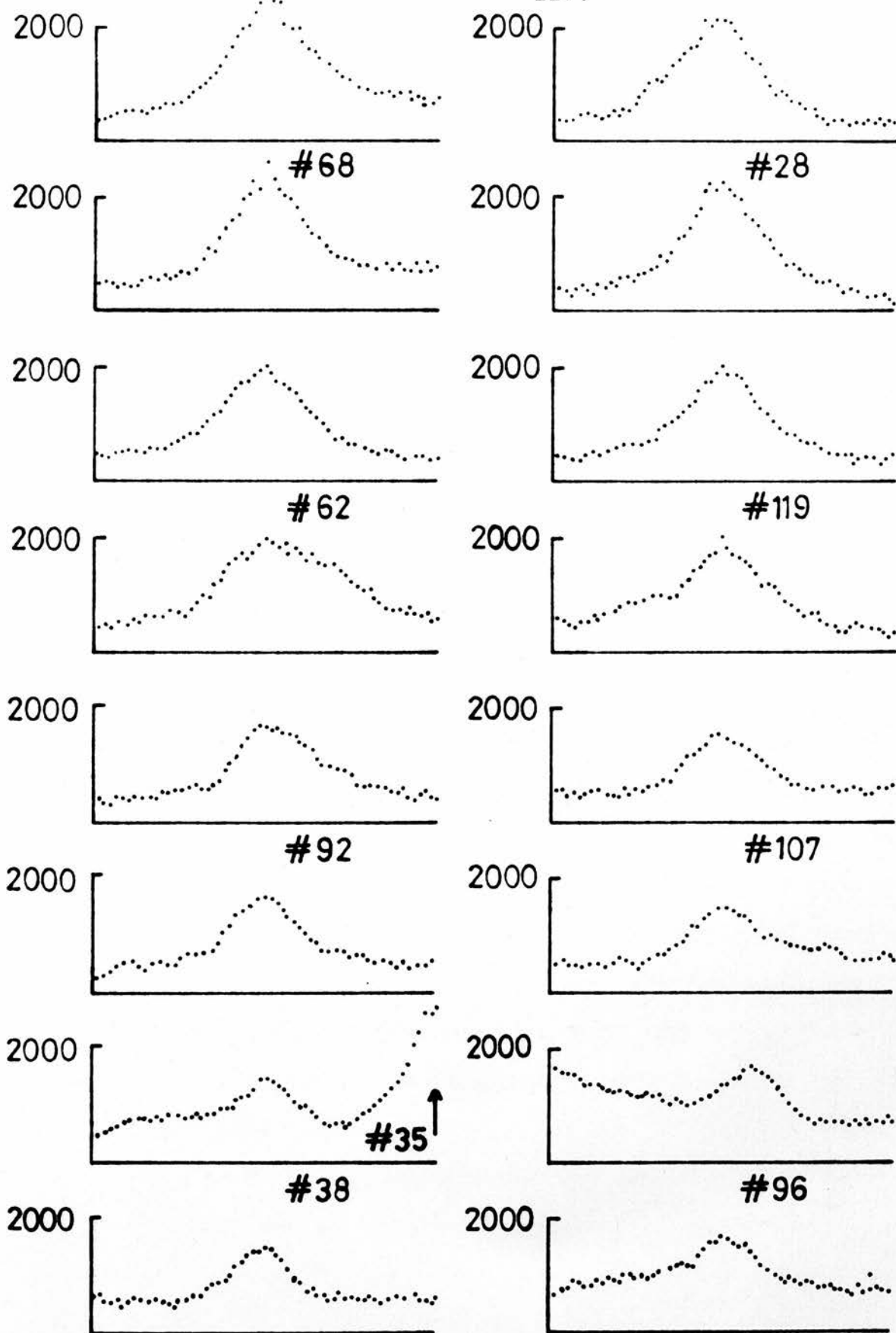
Figure 5.6. Intensity Profiles of HII regions in M83. Data from plate AAT 1402. Upper plots are E-W lower plots S-N. Dots are 1 COSMOS step apart.

amongst the profiles shown for the brightest six concern the relative brightnesses of the background levels of intensity - the data for plate 2886 indicating a brighter background than that from the AAT plates. This may be as a result of the intensity calibration extrapolation indicated in Fig. 4.4 and discussed at the end of Chapter 4.

The figures show that the HII regions in M83 have intensity profiles that blend into the background and do not have well defined edges. This is most clearly seen in the AAT data where resolution problems are less.

The profiles of the largest regions in the other galaxies studied here show no sharp edges either but resolution problems are generally greater for them.

Considering the roughly gaussian smoothing that has affected these images their roughly gaussian appearance may not be surprising. Yet many of the larger regions must have intrinsic intensity profiles that are also gaussian or conical perhaps, for otherwise some residual non-gaussian or non-conical trait should survive the gaussian convolutions they have undergone. The limitations on the forms of the intrinsic profiles will be quantified in Chapter 5.3.

Let us first consider the spectral make-up of the 'Hα' images examined here.

5.2   *The Hα bandpass*

The 'Hα' filter used in taking the 'Hα' photographs listed in Table 4.2 has a gaussian transmission

profile of FWHM 100Å and is centred at 6563Å. Allowing
for the redshift velocity of M83 (337 km s^{-1}), the filter
allows entry to 99.6% of λ6548 [NII] radiation and 81.6%
of λ6583[NII] radiation compared with unit entry of
Hα (λ6563) radiation. These nebular emissions arise from
the processes of recombination, in the case of Hα, and
from collisional excitation followed by spontaneous radia-
tive decay in the case of the [NII] lines (Osterbrock
1974). Continuum radiation allowed through the filter,
and contributing to the 'Hα' images, arises in general from
from the stellar background, although some exceedingly
weak continuum emissions are produced by nebular free-free
and free-bound transitions.

The stellar background continuum also contributes
to the 'Hα' intensity of the nearby 'sky', and so is
automatically removed in the determination of the FWHM
dimension of the nebula by the specification of the local
background (see Appendix F). However, the sky-reduced
spectra of some HII regions in M83 as presented by Dufour
et al. (1980) show residual continuum that is attributable
to the stellar association exciting the nebulae and its
blueness does indicate that it arises from very early
type stars. More important for present purposes is that
the contribution of this continuum to the 'Hα' flux (i.e.
that which would be measured with the filter used in this
work) is quite small, less than 10%, say: this figure
being deduced from the spectrum of region I of Dufour et
al. (1980) (region no. 81 here) which is at small galacto-
centric radial distance, and which is where continuum

subtraction proves most troublesome.

The contribution of the [NII] emissions is more significant. Both Dufour *et al.* (1980) and Brand *et al.* (1980) measure the $\lambda 6584$[NII]/Hα ratio in HII regions in M83 and find the mean value to be 0.40 ± 0.10 and independent of galactocentric radius. With the figures above this implies an average Hα contribution to our 'Hα' images of about 69%. This figure refers to the nebula as a whole and is based on the usual $\lambda 6584$[NII] / $\lambda 6548$[NII] ratio of 3:1. The (true) Hα profiles of HII regions will be merely scaled down versions of these 'Hα' profiles, <u>if</u> there is no change in the [NII]/Hα ratio across the face of the nebula. Kennicutt (1979a), encountering a similar need to switch from an 'Hα' (i.e. Hα + [NII]) morphology to a pure Hα morphology, refers to the photographic evidence of Elliot *et al.* (1977) to support his claim that "[NII] apparently exhibits a very similar morphology (to Hα) in these large objects". The work of Elliot *et al.* suggests, rather, that variations of the [NII]/Hα intensity ratio of almost an order of magnitude may be expected over the face of one such object - the 30 Doradus nebula in the LMC.

However, the supposition of similar morphologies may be acceptable: "....differences in spectrum between different parts of one HII region are small compared with differences that exist between spectra of different HII regions". (Searle 1971). All the major works on the spectra of extragalactic HII regions (Searle 1971, Smith 1975, Shields and Searle 1978, Pagel *et al.* 1979, and

others) have analysed the integrated spectra only - because it is time consuming to achieve good spectral and spatial resolution simultaneously. Shields and Searle (1978) recognise that the large HII regions observed in external galaxies are often complexes of smaller individual HII regions that "have previously been shown to be remarkably homogeneous in spectrum". In such a case i.e. of a large number of small homogeneous HII regions being observed as a single larger entity, the spectrum of the larger entity would not change across its face, even though that may be the case for any individual component given sufficiently high spatial resolution.

Observations of galactic HII regions by Hawley (1978) suggest that the [NII]/Hα ratio may vary across faces of individual nebulae by as much as a factor of 3 - M16(NGC 6611), for instance, shows such a variation - yet for many other nebulae in his sample there is no indication of significant spatial variation in this ratio.

The HII region models of Dufour et $al.$ (1980) and Balick and Sneden (1976) with $Z_* = 2Z_\odot$ and $T_* = 38\ 000K$, both predict global $\lambda6584[NII]/H\alpha$ line ratios of 0.4 as was observed in M83 by Brand et $al.$ (1980) and Dufour et $al.$ (1980). The models of Balick and Sneden also indicate that this ratio is independent of the average nebular density, which is the only nebular variable input to the models.

Finally, it is noted that Brand et $al.$ (1980) and Dufour et $al.$ (1980) used quite dissimilar aperture sizes in making their observations (1".8 x 4".5 and 3".6 x 40",

respectively) and yet achieved the same results.

The above evidence is consistent with an assumption that the fractional Hα contribution to an 'Hα' image as described above is constant across the face of any HII region, and so the Hα profile, in suitable intensity units, is just a scaled down version of the 'Hα' profile.

But has M83 been particularly co-operative in this regard or is this a result that can be applied to other galaxies?

[NII]/Hα line ratios have been measured in a number of extragalactic HII regions and a summary of such results, applicable to Local Group and nearby spiral galaxies, is shown in Table 5.1.

It is not forgotten that significant correlations exist between the [NII]/Hα ratios and galactocentric radius in some of these galaxies. Yet the scatters in the ratio displayed are small and the values themselves indicate that the Hα contributions dominate those of the [NII] lines even if the filter used in a manner similar to that here has uniform transmission at the wavelengths concerned. With a filter like that used here the Hα contributions will be somewhat larger still.

Although these results do not prove that the [NII]/Hα ratio is constant across the face of any HII region, they would suggest that the errors arising from such an assumption are likely to be quite small - the galaxy amongst those listed in Table 5.1 where this assumption might lead to the largest errors would appear to be M83! yet we have seen other evidence to the contrary.

Table 5.1

Mean Hα/(Hα+[NII]) ratios in
extragalactic HII regions

Galaxy	Ratio	No. of HII regions observed	Source
M101	0.80 ± 0.11	13	1
M33	0.87 ± 0.08	6	1
M51	0.67 ± 0.06	5	1
NGC 2403	0.90 ± 0.03	5	1
NGC 2903	0.73 ± 0.07	4	1
NGC 6822	0.95 ± 0.03	3	1
IC 1613	0.91 ± 0.05	2	1
M83	0.66 ± 0.01	5	2
M83	0.66 ± 0.06	17	3
NGC 1365	0.75 ± 0.01	3	4
NGC 300	0.90 ± 0.04	5	4

Sources   1   Smith (1975)

2   Dufour *et al.* (1980)

3   Brand *et al.* (1980)

4   Pagel *et al.* (1979)

So there is good reason to expect it to hold reasonably well for the other galaxies - it must surely be a contrived and contrary set of physical conditions that can produce such galaxy-wide constancy in this regard and yet significant intra-nebular variations.

5.3   *The Intrinsic Profile*

The dimension to be assigned to an HII region should ideally have some physical meaning, although to resort to empirical analysis should not be regarded as totally inferior. (see Ch. 3.14).

If the HII region, say, is of some uniform density greater than that of the surrounding interstellar medium, then the edge of the nebula is well defined, its size is well defined and so the dimension extracted from its light output should be defined so as to represent that size. Since Hα is usually the strongest emission from an HII region it is with this that we concern ourselves, and it was for this reason that the discussion in Chapter 5.2 was held.

The Hα emission at a point in an HII region distance r from the centre is given by

$$I_{H_\alpha}(r) \propto N_e^2(r) T(r)^{-3/2} \exp\left(\frac{17547}{T(r)}\right) \tag{5.1}$$

(Osterbrock 1974, Ch. 4), where N_e and T are the local electron density and temperature respectively. Fig. 5.7 shows some typical radial distributions of N_e and T in cases of assumed spherical symmetry and shows also the
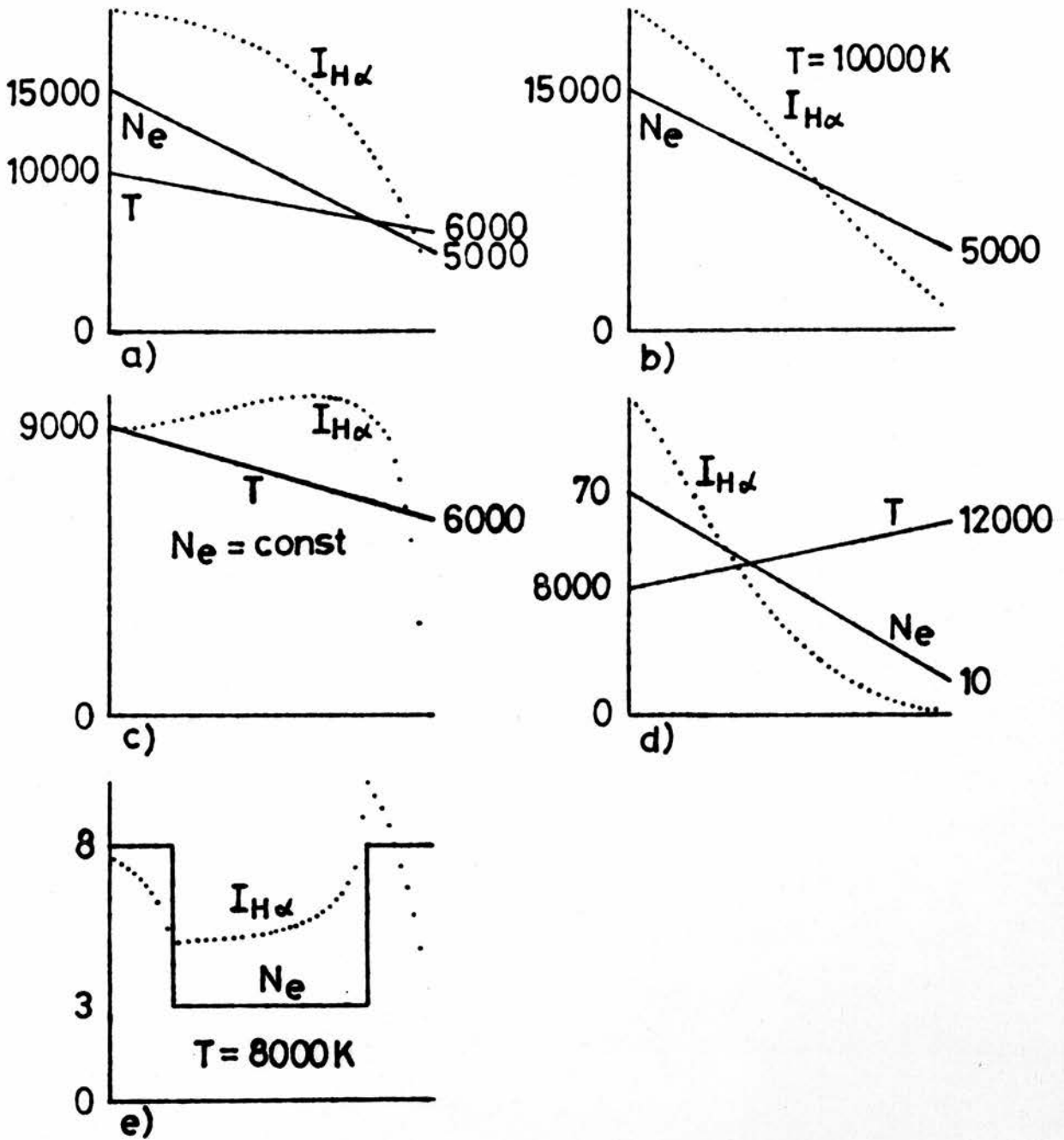
Figure 5.7. Some possible Hα profiles of HII regions. Profiles in density and temperature as indicated produce the Hα intensity profiles given by the dotted lines. End point values refer to T or N_e as appropriate. Intensity scales are linear.

observed Hα output that such structure produces. The Hα profile is obtained by intergrating (5.1) along the line of sight at each point across the face of the nebula. The distributions of N_e and T were specified on a grid of 100 mesh points to a diameter, and are simplified versions of those observed in galactic nebulae (see for instance Peimbert, 1966, Menon, 1964, Cunningham 1968, Terzian 1968b, Deharveng 1974, Perrenod *et al.* 1977). Other combinations of $N_e(r)$ and $T(r)$ than those shown in Fig. 5.7 were tried but the resulting profiles in Hα are typified by those shown.

Fig. 5.7e serves to illustrate the effects of radially localized density enhancements upon the Hα profile. A central enhancement, as observed in M8 and M16 (Cunningham 1968, Meaburn 1969) and in the NGC 2363 complex in NGC 2366 (Kennicutt *et al.* 1980) would produce a central intensity increase that may be interpreted as a 'core' (Sandage and Tammann 1974a) - and indeed the density structure of NGC 2363 may be well described by a core and halo - while a shell of higher density would produce a ring type HII region (Gum and de Vaucouleurs 1953, de Vaucouleurs 1978c, 1979c).

Fig. 5.7 indicates that a wide variety of morphologies of Hα profiles of HII regions may occur. From it, however, we may set up a sequence against which to classify such profiles. The sequence has as its extrema the 'exponential decay', similar to the profile in Fig. 5.7d, and the 'cylinder' (Fig. 5.7c). Between them runs the gamut of 'gaussian' (like d, also) 'cone' and 'hump'

(a). The ratio of the size of the HII region, as defined by its density limits, to the FWHM of its (intrinsic) Hα profile is

- greater than 2 for exponential decays and gaussians
- equal to 2 for cones
- between 2 and 1 for humps
- equal to 1 for cylinders

It is imperative, then, that an Hα profile be classified correctly if an error of perhaps a factor of 2 in the size of the HII region is not to be incurred.

The scheme has problems though: in cases other than pure cones and cylinders the ratio defined above is indeterminate. Also, though the scheme is one of intrinsic profiles, the observed profiles have undergone gaussian convolution (see Ch. 4.7). The degree to which accurate identification and classification can be made from the convolved profiles needs quantifying.

Figs. 5.8 and 5.9 show convolutions of the two extrema of this classification scheme with families of gaussians. From them it appears that unless

$$d_1 \geq 1.5 \, dg \text{ (in the case of the cylinder)}$$

or $\quad d \geq 1.8 \, dg$ (for the exponential decay)

then it is impossible to identify with any certainty the underlying intrinsic profile. It is perhaps unnecessary to state that convolutions of cones with gaussians are indistinguishable from pure gaussians unless the cones are relatively very wide.
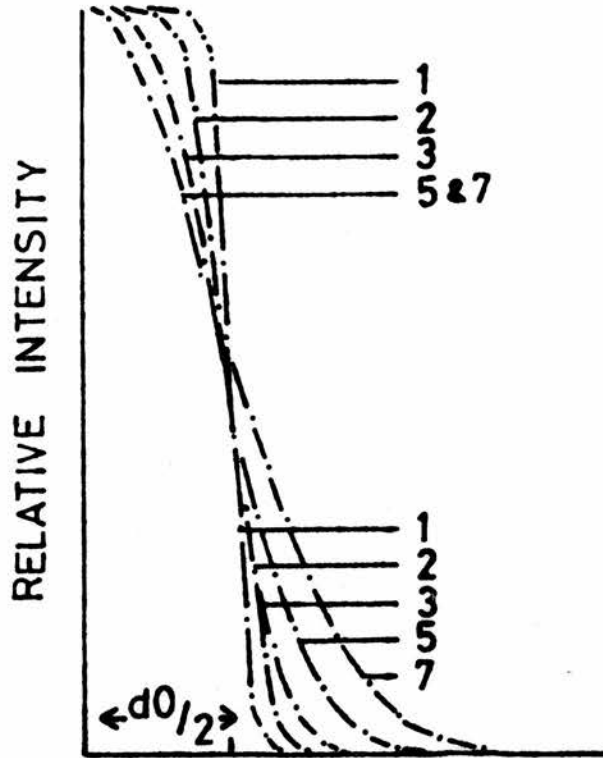
Figure 5.8. Convolutions of a cylinder of FWHM d_O with gaussians of FWHM dg.

1) dg = 0.24 d_O i.e. σ = 0.1 d_O
2) dg = 0.47 d_O i.e. σ = 0.2 d_O
3) dg = 0.71 d_O i.e. σ = 0.3 d_O
4) dg = 1.18 d_O i.e. σ = 0.5 d_O
5) dg = 1.65 d_O i.e. σ = 0.7 d_O
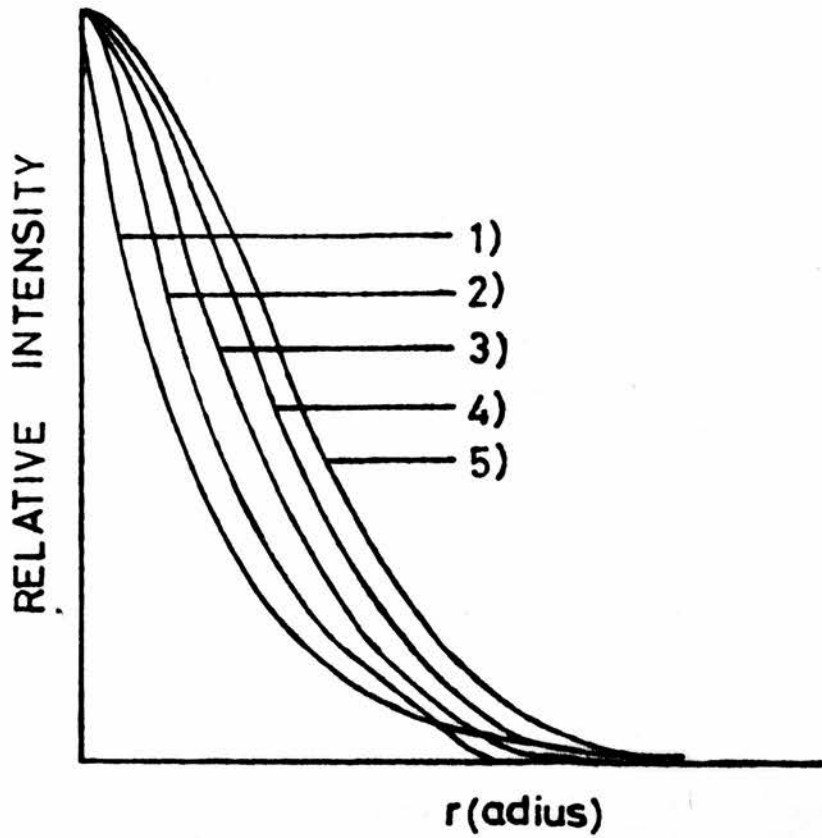
Figure 5.9. Convolutions of an 'exponential decay' profile
(curve 1) of form ∝ exp (- r/E) with gaussians with-

$\sigma = E/4$ curve 2)
$\sigma = E/2$ 3)
$\sigma = 3E/4$ 4)
$\sigma = E$ 5)

The above requirements on d_1, the FWHM of the convolved profile, are met for several HII regions in M83 on the plates listed in Table 4.2, and several of the regions whose profiles are displayed in Figs. 5.1 to 5.6 fall into this category. An examination of these profiles shows that the underlying intrinsic intensity profiles are probably cones or gaussians, though the possibility of them being exponential decays cannot be discounted. There is a noted lack of any regions with probable cylindrical intrinsic profiles. No obvious ring or core/halo structures were seen amongst these regions. A similar examination of the data for the other galaxies studied here (see Table 4.1) threw little further light on this question of morphology since they are all apparently much smaller objects and the seeing is more dominant in the convolutions than it is for the HII regions of M83.

The intrinsic profiles of the smaller regions, in all the galaxies studied, are swamped by the seeing etc., and their intrinsic dimensions will be subject to an assumption about their morphology.

Fig. 5.10 shows the relationships between the FWHM dimensions of the intrinsic profile, do, the convolving gaussian, dg, and the convolution d_1, under the assumptions of the intrinsic profile, Po, being gaussian (curve A), conical (C), cylindrical (E) and an exponential decay (X).

The data used in deriving Fig. 5.10 is tabulated in Table 5.2. It was obtained from a programme to convolve two 2-D functions. The FWHM dimensions of the intrinsic
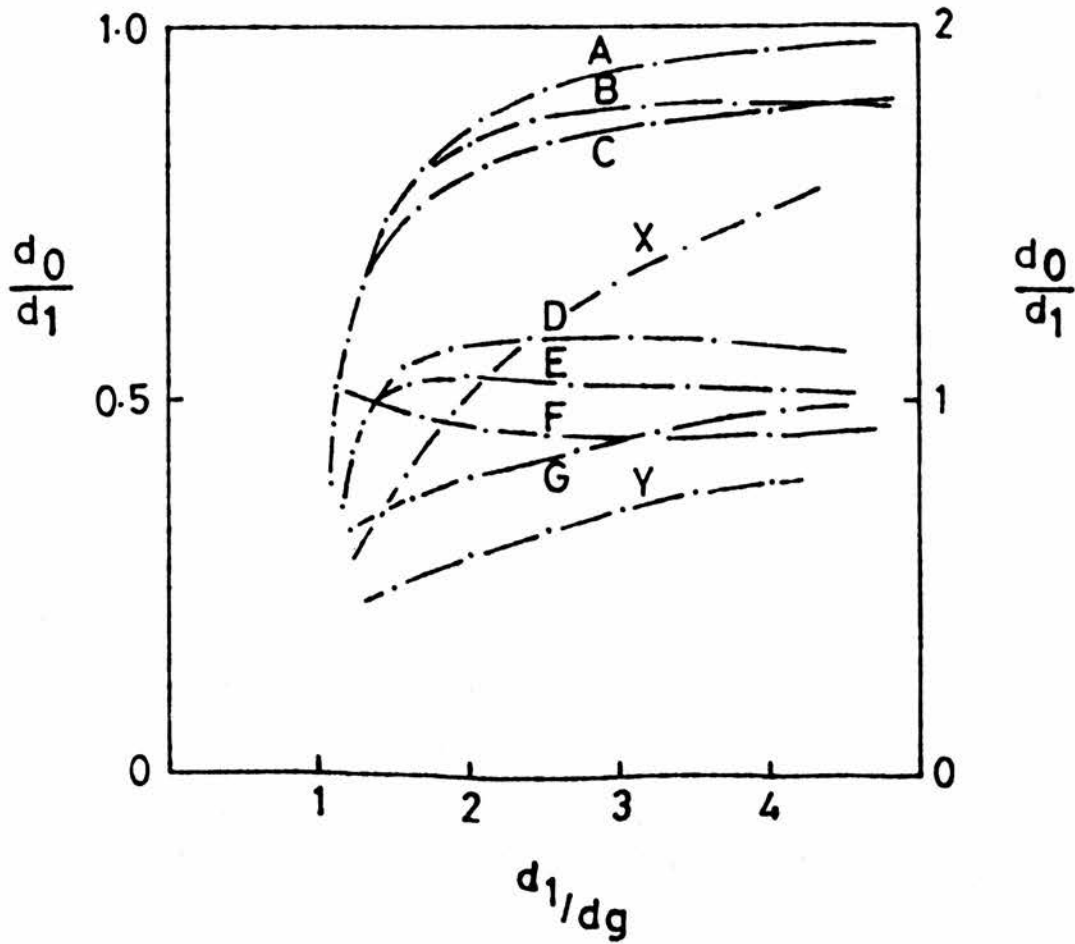
Figure 5.10. <u>Derivation of the FWHM of the intrinsic profile</u>
d_o, d_1, d_g are the FWHM dimensions of the intrinsic,
the convolved and the convolving (gaussian) profiles.

Curve		Intrinsic Profile	Impact	Scale
A		Gaussian	irrelevant	Left
B		Conical	$d_o/2$	Left
C		Conical	0	Left
D		Cylindrical	$d_o/2$	Right
E		Cylindrical	0	Right
X		Exponential decay	0	Left
F	is	C/A	—	Right
G	is	A/E	—	Right
Y	is	X/A	—	Right

Table 5.2

Convolutions with gaussians (2-D)

d_o is the FWHM dimension of the intrinsic profile

dg is the FWHM dimension of the convolving gaussian

d_1 is the FWHM dimension of the convolution

(Zero impact measurements presented here)

Conical Intrinsic Profile

$\dfrac{d_1}{dg}$	$\dfrac{d_o}{d_1}$
8.96	0.947
4.70	0.903
3.25	0.871
2.51	0.844
2.08	0.818
1.79	0.789
1.69	0.756

Cylindrical Intrinsic Profile

$\dfrac{d_1}{dg}$	$\dfrac{d_o}{d_1}$
8.40	1.010
4.10	1.036
2.69	1.052
1.99	1.070
1.61	1.052
1.41	1.010
1.29	0.938
1.22	0.870

Exponential Decay Profile

$\dfrac{d_1}{dg}$	$\dfrac{d_o}{d_1}$
3.36	0.700
2.57	0.610
2.17	0.542
1.92	0.489
1.76	0.447
1.63	0.413
1.53	0.385
1.45	0.362

cone and cylinder profiles were 10 units and 20 units, re-
spectively, on a grid on which the convolutions were per-
formed, so the resolution is a little coarse. However,
the points plotted in Fig. 5.10 show that this coarseness
does not introduce an error of more than about 2% in the
calculation of d_o.

Also shown in Fig. 5.10 by curves B and D is the
effect of measuring the FWHM of the convolution from a
cut through the 2-D profile that does not pass through the
axis of symmetry. (The distance of the plane of the cut
from this axis is the 'impact distance' - see Ch. 4.7).
At impact distances of $d_o/2$ errors of about 10% are induced
in the derived value of d_o, though, since such offsets
were not encountered, the errors from this source are ex-
pected to be less than this.

Curves F and G in Fig. 5.10 show the effects of in-
correctly identifying the morphology of P_o. If P_o is cy-
lindrical, say, and is wrongly assumed to be gaussian,
then curve G shows that the error induced in d_o will be
greater than 10% if $d_o \lesssim 3dg$. Curve F shows that if P_o
is assumed to be gaussian instead of conical, or vice
versa, the error in d_o is always less than 9%. Recall
that a positive identification should be possible if
$d_o \gtrsim 1.8$ dg.

5.4 *Results IV: The Sizes of HII Regions in M83*

Table 5.3 presents the mean FWHM dimensions of the
COSMOS images of the HII regions in M83 as measured on each

Table 5.3

FWHM dimensions of HII Regions in M83

No.	I	PLATES					
		3223	2918	2886	2955	1402	1404
1	127	sat		/109:a		/238e	
2	120	sat		/68:a		/228	
3	50	81:		70a		213e	
4	102	70:	95:	67ea	70ex	194	
6	60	68	92	52a		165	
7	112	80	84	94a		191	135
8	324	sat	106	107a	74f	334	416
9	164	sat	107	93a	81f	291e	277e
11	171	87	101	101a	57f	339	317
12	102	74	107f	78a		263	
13	265	sat	97	86a	68f	236	337
14	229	87	84	90a	63f	186	
16N	80	57:	118:f	104a		204	
16S						156	
17	108	70e		75		224	
18	94	71	79f	81:		231	
19N	90:	89	146f	/89:e	48ex	239	
19S						261	
20	94	103	110ef	75		223	
22	95	81	73f	69		211	
23	91	91	87f	104e		260	
26	90	64	74f	83		/150e	
28	234	83	93f	78	51f	239	250
29	58	74	80x	68		167	
30	58	100	97x	61e		250	
31	70	68	65f	65e		170	
32	95	84	85f	71	58x	252	259f
33	309	sat	156ef	123ea	86ef	372e	458e
34	324	sat	110f	88e	74f	211	308
35	265	88	111f	72a	55f	219	316
37	68	68	176:f	62a	30ex	188	
38	108	52	108ef	70	20:x	167	
39	158	68	90f	74	31x	224	210
40	109	81	79f	97		236	
41	270	104	99f	96	78f	354	366
42	176:	104		70:		303	
43	178	96	96f	87	58x	272	264
44E	270	sat	93	84ea	65f	220	333e
44W						187	
45	159	93	95	82	56f	317	292
46	62	83	89f	56a		144	
47E	68	72	96ef	62e		.168	
47W	68			70:			
48	165	136	118	116	73ef	498	416
49	95	85	87f	103		242	

Table 5.3 cont.

No.	I	3223	2918	PLATES 2886	2955	1402	1404
50	236	89	87f	72	56f	245	254
51	73	99	94:f	82		210	
52	95	110	84f	102	78ex	/265e	
53	167	71	71f	74	62x	226	207
54	162	88:e		93	63x	266e	192
55	147	90:		114	79x	270	307
56N	121	94	93f	91	36:ex	183e	221
56S						204	
57	152	79	80f	80		156f	
58	37	64	73f	75		159	
59	214	78		71	46f	215	287
60N	191	114e		121	49f	216:	
60S						225	
61	249	sat	127f	101	70f	322	
62	209	91e	101f	83	62ef	316e	276e
64	84	108	83f	94		173	
67	204	111	112:f	101	56f	368	328
68	213	91	107f	77	62f	230	239
69	111	81	92:f	82		209	
70	74	70	75f	67		151	
71	89	70	82f	76		241	
76	132	70	91f	73	52x	266	236
78	84	79e	110ef	96		208	
79	38	45		64:		139	
80	118	61		62a	50ex	152	211
81	310	sat	111	86	81f	290	320
83	143	105	135f	109	65f	368e	291
84N						299	
84S	174	sat	124	98	92f		410
84E						205	
85	300	sat	127	108:	84f	308	432
88	255	132:e	124:	89	73f	239	306
89	191	:		83		298:	105:
90	161	94	120f	87	41f	324	339
91	167	60	78f	54	39x	144	182
92	152	75	84f	66	47ex	222	260
95	181	70	80f	73	46f	182	256
96	107	81	100f	65	44x	190	194:
98	44	64	104	71e	43x	142e	
99	117	68	81f	65	52x	220	
100	186	sat	123f	93	80f	318	333e
101	73	59	143:f	61		161	
102	53	76	149f	51		211	
103	200	90	104f	80	54f	192	298
104	94	82e	110f	93	/296		
105	196	90	104f	76	82f	261	255
107	119	75	97f	71	65x	220	
108	158	92	96f	79	55x	273	250
109	199	84	95f	65	48f	208	291
110	175	94	96f	83	68x	270	288e

Table 5.3 cont.

No.	I	PLATES					
		3223	2918	2886	2955	1402	1404
111	185	94	94f	77	53x	247	240
112	100	83	90f	107		269	183:
113	111	113	102f	100		245	192f
114	61	120	88f	83e		339e	
115	91	79	90x	88		268	
118E	77	130e	103ef	91		244:	
118W						217:	
119	170	93	96f	72	55x	212	296ef
120N	72	123	125f	111		145	
120S						96:	
121	93	74e	122f	80e		296	
124	94	73	95x	69		200	
125		77	112ex			181:e	
127	64	77	91x	69		228	
151	83	62	83x	82		157	
152	106	76	80f	61	45x	209	164e
153	78	98	91f	88		211	
155	67	91	100f	101		256	
156	78	76e	93x	80		171e	
157	55	99	92x	76e		234	
300	74	95	108f	95:		207	
302	40	79		59x			
306	35	75e	64x	56x		131e	
310	44	55		58		96	
318	52	62	85x	57x			
320	120	71	88f	79:	45ex		
321	51	82	88x	83			
322		61:e	94f			131	
323	53	57	73:f	66		120	70e
325	62	71		48		120	

plate indicated. As described in Appendix F, an FWHM di-
mension is derived from a profile through the image, and
the values in Table 5.3 are the means of two such measures
made in orthogonal directions.

Column 1 gives the region number as in Table 4.9.
Where a 'region' resolves into two or more entities they
have been unambiguously designated and treated separately.
For instance 'region' number 118 is seen to be two regions
on plate 1402 and the two components have been measured
separately there. Otherwise it has been measured as one
unit.

Column 2 gives the relative intensity difference
between the peak and background intensity levels as assigned
on plate 2886.

Columns 3-8 give the mean FWHM dimensions, d_1, in
microns (10^{-6}m). They are subject to errors of greater
than about 10% - see Appendix F.

Notes

1)   'sat' means that the image appears saturated,
        usually indicated by a flat top to the COSMOS
        profile - although transmission quantization pro-
        duces the same effect.

2)   a colon indicates an undue amount of uncertainty
        in the determination; usually in selecting a
        particular value for the background intensity.

3)   a '/' indicates that the orthogonal directions
        mentioned above were not SN and EW. This occurred
        when the HII region appeared significantly elliptical

on the intensity contour maps, and lay with its principal axes away from the SN and EW directions. The cuts through the profile were than made to coincide more closely with the principal axes and the dimension derived then coincides closely with the mean of the major and minor axes of the ellipse at the Half Maximum intensity level. If d is the mean of two orthogonal chords passing through the centre of an ellipse of eccentricity e, and d_{mm} the mean of the major and minor axes of the ellipse and θ the angle between the chords and the principal axes, then

$$\frac{d}{d_{mm}} = \frac{1}{e^2}(1-\sqrt{1-e^2})(\sqrt{1-e^2\cos^2\theta} + \sqrt{1-e^2\sin^2\theta}).$$

This function has a maximum at $\theta = 45^\circ$ which provided $e < 0.87$, i.e. $a/b < 2$, is less than 1.06. Thus d estimates d_{mm} to better than 6%. irrespective of θ, provided $e < 0.87$. No eccentricity greater than 0.87 was observed in the present data. If the cause of non circularity of HII region images is multiplicity (see Figs. 4.14 to 4.17) then this probably implies limits to the degree of multiplicity and to the size and separation of the components that may still be observed as one unit. Any remaining eccentricity greater than 0.7 is indicated in Table 5.3 by 'e'.

4)   The symbols 'f' and 'x' mean that the background alone and both the peak and background of the

profile lie outside the calibrated range of
intensities. (See Ch. 4.7). The symbol 'a'
has been used for the data of plate 2886 to
indicate regions that lie wholly in the cali-
brated range of intensities. As indicated in
Ch. 4.7 the rest of the HII region data on
plate 2886 is of class F, but only just so.

The data is presented in this rather raw
form since the analysis from here could take
several directions depending upon the morpho-
logy assumed for the intrinsic Hα profiles.
Should it become clear that one such assumption
produces a significantly superior distance in-
dicator, then the dimensions of the HII regions
of M83 under this assumption will also be pre-
sented. (Table 5.12).

5.5   *Results V: Assuming Gaussian Intrinsic Profiles*

Inspection of the Hα profiles displayed in Figs.
5.1 to 5.6 shows that the assumption that the intrinsic
Hα profiles are gaussians is not unreasonable, and from
the simple modelling in Ch. 5.3 it was seen that such pro-
files can arise from quite feasible nebular structures.
The dimensions of the convolved profiles, d_1, are present-
ed in Table 5.3, and reduction to d_0, the FWHM of the in-
trinsic profile - assumed here to be gaussian - is via
equation (3.1)

$$d_0^2 = d_1^2 - d_*{}^2$$

also given as curve A in Fig. 5.10, where the values of d_* (or dg) are given in Table 4.10 (Note: wherein they are labelled d_1).

Fig. 5.11 shows some comparisons of these values of d_o obtained from several pairs of plates. The filled symbols represent the brighter HII regions (defined as I > 120 - see notes to Table 5.3) and the open symbols the fainter ones. Where plotted, those bright regions of class F are distinctively marked.

Only those regions with $d_o \geqslant 2.0$ arcsecs are plotted and used in the following analysis since the errors on d_o are large ($\geqslant$ 50%) when $d_o \leqslant 2''$.

Let us test the null hypothesis that the values of d_o so derived are independent of the plate from which they are measured, i.e. we must test if

$$dy = md_x \qquad (5.2)$$

is a good representation of the data when m = 1. (d_x and d_y represent d_o from plates x and y).

The sources of the data where this has been tested are shown in columns 1 and 2 of Table 5.4. Testing of the hypothesis was done on various subsets of the data, specified by I, and this is indicated in column 3. Column 4 gives the number of points in the data set. Columns 5 and 6 give the optimal value of m and its standard error as determined by the maximum likelihood technique described briefly in Appendix M.

The comparisons of data from similar plates, i.e. UKST or AAT, were done assuming equal errors in each variable, so the exact value is not required (see Appendix M).
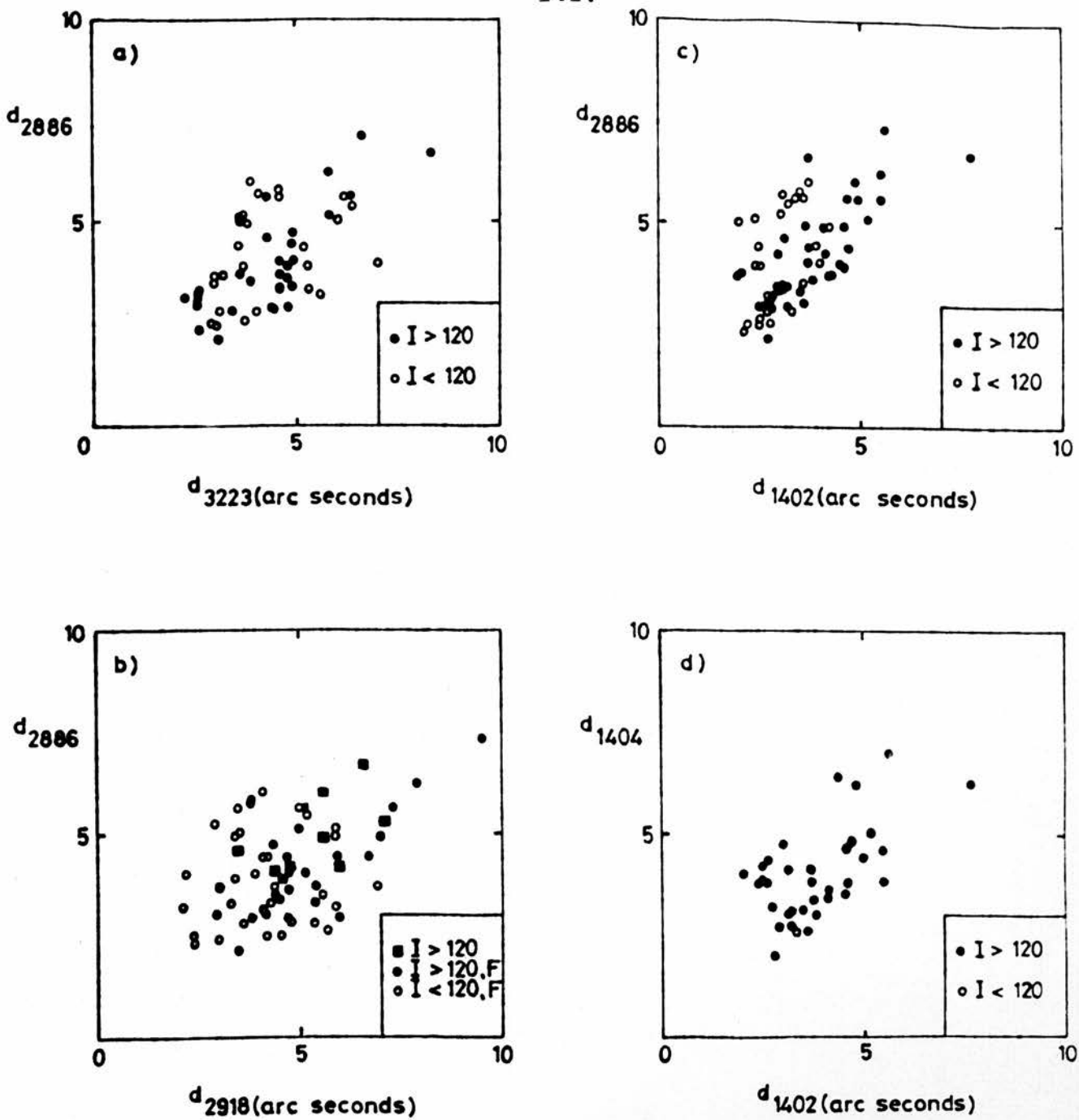
Figure 5.11. Comparisons between the values of d_o from 4 pairs of plates. d_O is the FWHM dimension of the intrinsic HII region profile and is assumed to be gaussian here.

Table 5.4

The values of d_o from COSMOS measures
of plates x and y are fit by $dy=md_x$
(Profile assumed - 'gaussian')

x y (UKST-UKST)		I		n	m	Δm	rms devn.	$\left|\frac{m-1}{\Delta m}\right|$
3223	2886	>120		29	0.89	0.03	0''.57	3.7
3223	2886	<120		29	0.99	0.06	0.90	0.2
3223	2886	all		58	0.93	0.03	1.06	2.1
2918	2886	>120		10	0.93	0.05	0.63	1.5
2918	2886	>120	*	35	0.81	0.03	0.67	7.1
2918	2886	all	*	68	0.86	0.03	0.95	4.2
2955	2886	all	*	34	1.37	0.07	0.77	5.4
3223	2918	>120	*	29	1.07	0.04	0.66	1.8
3223	2918	all	*	67	1.07	0.04	1.04	1.6
3223	2955	all	*	20	0.58	0.04	0.75	10.7
2918	2955	all	*	29	0.61	0.03	0.77	13.1
(AAT-AAT)								
1402	1404	>120		33	1.03	0.05	0.73	0.8

* includes data of class F.

However, an estimate of these errors is given in Column 7 by the rms deviation of the data about the optimal line. Column 8 gives, essentially, the probability that m=1 is an acceptable value - the units are standard deviations.

Table 5.4 shows that, indeed, the same values of d_0 are derived from the two AAT plates, and that the same can be said about the UKST plates if concentration is directed to that data free from calibration problems - this is the rather decimated subset of data used in the first four lines of Table 5.4. From the first two lines it may be deduced that there may still be some saturation affecting the brighter HII regions on plate 3223. (Only six HII regions formed the class 'a' subset of data from plates 3223 and 2918, so no analysis was attempted).

The inclusion of class - F data in the analyses is shown to greatly reduce the acceptability of the null hypothesis.

Maximum likelihood analysis of data sets from dissimilar plate material requires the specification of the respective errors. Appendix F shows that errors on d_1 are typically 10-15% and Table 4.10 shows errors on d to be about 5%. Errors on d_0 can then be expected to be typically 19-27% (or 0".84 - 1".24) for typical UKST images and 16-24% (0".52 - 0".77) for typical AAT images. These figures compare well with the observed errors given in column 7 of Table 5.4, where mean values of 0".8 $\pm$ 0".2 and 0.73 (+0".2?), respectively, would be deduced.

Allowing the errors to vary through such values actually has little significant effect in the analysis -

Table 5.5

The values of d_o from COSMOS measures of plates x and y are fit by $dy=md_x$ (Profile assumed - 'gaussian')

x	y	I	n	m	Δm	$\left\lvert\dfrac{m-1}{\Delta m}\right\rvert$
1402	3223	>120	25	1.18	0.05	3.4
1402	3223	all	58	1.27	0.05	6.0
1402	2918	all	10	1.16	0.05	3.3
1402	2886	>120	34	1.10	0.04	2.9
1402	2886	all	62	1.19	0.04	4.8
1404	3223	all	25	1.29	0.06	5.3
1404	2918	all	10	1.16	0.07	2.4
1404	2886	>120	34	1.07	0.04	1.9

the results in Table 5.5 use errors of 0.8 and 0.7 arcsecs, respectively, for the UKST and AAT data.

It is apparent that the measures of d_o from the UKST material are substantially i.e. about 20%, larger than corresponding measures made from the AAT data, and this effect demands explanation if not correction.

A similar situation was noted by Arp and Bruekel (1973) concerning HII regions in M31, but their offered explanation is not tenable in the circumstances met here. (See Ch. 3.7 also). Their own data, acquired with an interference H_α filter produced a tally of fewer and generally larger HII regions than did that of Baade and Arp (1964) who used a wider $H\alpha$ filter. They explained this as an effect of being able to expose their plates for much longer without hitting sky brightness problems, but thus registering background nebular emissions which blended together small neighbouring HII regions into single larger entities. Their explanation cannot be used here because the same filter was used for acquisition of both sets of data, exposure times are comparable, and the sample of HII regions is the *same* - unrecognised multiplicity affects both sets of data equally.

Sérsic (1979) has attempted to explain such an effect as due to emulsion diffusion and choice of plate scale. If each image on a plate has a size that is partly due to a constant amount, c, of emulsion diffusion, then the image of an object on a plate of small scale will be relatively larger than that of the same object on a plate, of the same emulsion, but of larger scale. (NB. 16" mm^{-1}

is a *larger* plate scale than 67" mm⁻).

The emulsion spread function, that is an integral part of the function f_a described in Ch. 4.7, is expected to fully account for emulsion effects. In practice f_a and the seeing are replaced in the 'deconvolution' process by the empirical intensity profiles of the images of stars.

The results of Table 5.5, which lead to the rejection of the null hypothesis come as something of a surprise and, if unexplained, lead to a serious distance effect in the use of HII region sizes as distance indicators. For if M83 were a calibrator and a galaxy just like M83, but further away, was measured in this scheme, the effectively smaller plate scale for the data of that galaxy would lead to an overestimation of the size of its HII region, and underestimation of its distance, and an overestimation of H_o. (The overestimation of HII region sizes resulting in an overestimation of H_o by a similar amount).

The results of a similar analysis of the XY data are shown in Table 5.6. Data from similar plates were treated as having equal errors and for the UKST-AAT comparisons the calculations were performed on suitable grid points in the error-error plane. Again, the results are practically independent of the exact values of the errors.

As in Table 5.4, the reliable data tends to support the null hypothesis. It is noteworthy that every value of the 'probability' of more than 2 s.d.'s is associated with plate 3223. It is clear that the inclusion of known saturated data encourages the rejection of the null hypothesis, but, not shown, is that most (70-80%) of the data labelled

Table 5.6

The values of d_o from XY measures

of plates x and y are fit by $dy = md_x$

(Profile assumed - 'gaussian')

x	y	I		n	m	Δm	rms devn.	$\left\|\frac{m-1}{m\Delta}\right\|$
3223	2886	>120		18	0.84	0.06	0".70	3.0
3223	2886	>120	*	29	0.81	0.03	0.65	5.7
3223	2886	<120		13	0.99	0.17	1.49	0.1
3223	2886	all		31	0.90	0.07	1.13	1.4
3223	2886	all	*	42	0.85	0.05	1.02	3.0
2918	2886	all		17	1.16	0.08	0.83	2.0
2955	2886	all		18	1.13	0.08	0.75	1.7
3223	2918	all		11	0.77	0.06	0.71	4.1
3223	2918	all	*	20	0.72	0.04	0.76	7.1
3223	2955	all		21	0.71	0.05	0.86	6.1
2918	2955	all		13	1.01	0.06	0.51	0.2
1402	3223	>120		13	1.35	0.07	0.48	4.7
1402	3223	all	*	19	1.36	0.05	0.43	7.8
1402	2918	all		8	1.00	0.09	0.78	0.0
1402	2886	all		18	1.05	0.05	0.56	1.0
1402	2955	all		10	0.92	0.09	0.82	0.8

* contains data recognised as saturated.

'all' is in fact 'bright' (I > 120). It is not clear

also how much of this data on plate 3223 suffers from

saturation. Examination of the intensity profiles has

already led to the identification of some saturated images,

but there may be others undetected.

Although the AAT *vs*. UKST data sets in Table 5.6

are rather small, it seems possible that the systematic

effect seen in Table 5.5 does not affect the XY data, and

that the effect there is due to some part of the COSMOS

data reduction technique.

Possible sources of such an effect are

1)   an incorrect choice of the relationship expected

        to exist between the values of d_o from two plates

        (i.e. eqn. (5.2)).

2)   an incorrect assumption about the form of the in-

        trinsic profile that leads to these values of

        d_o - so far a 'gaussian' assumption has been used.

1)   The choice of equation (5.2) arose from inspection

        of the data plotted out in Fig. 5.11. Equation

        (5.2) is a straight line relation forced through

        the origin. The fitting of a higher order curve

        seems unwarranted, but perhaps the fitting of a

        more general straight line may be profitable. A

        plate scale effect, as postulated by Sérsic, but

        as yet unaccounted for here, may require a relation

        of the form

$$d_y = md_x + k$$

Table 5.7

Values of d_o from COSMOS measures of plates x and y are fit by $dy=md_x+k$ (Profile assumed - 'gaussian')

x	y	I	n	m	k
1402	3223	>120	25	0.94	0.95
1402	3223	all	58	1.12	0.54
1402	2918	all	10	0.83	1.63
1402	2886	>120	34	1.05	0.19
1402	2886	all	62	1.10	0.31
1404	3223	all	25	1.66	-1.44
1404	2918	all	10	0.67	2.56
1404	2886	>120	34	1.07	-0.01

with a non-zero value for k. The constraint of
k=0 was released and values of m and k were de-
duced from the maximum likelihood method outlined
in Appendix M using errors on the variables that
were again allowed to range between 0".5 and 1".3.
The results did not suggest any particularly uni-
versal value for k nor did they produce an homo-
generous set of values for m. The results in
Table 5.7 used δ_{UKST} = 0".9 and δ_{AAT} = 0".7 though
the process is again insensitive to the precise
values.

It seems that k=0 is not an unreasonable con-
straint.

2)   The source of the systematic effect in Table 5.5
may lie, then, in the assumption about the intrin-
sic profiles. Until now we have assumed these to
be gaussian, yet there is evidence to suggest that
this may not be the case.

Table 5.8 shows the results of fitting lines of
the form (5.2) to data sets comprising the values of d_p
for the HII regions on one hand and the (raw) XY measures
on the other. The quantity d_p is most simply thought of
as the COSMOS datum reduced to the level of the plate image
by application of the formula

$$d_p^2 = d_i^2 - d_c^2,$$

where d_c (=25.2μm) is the width of the COSMOS spot.

The result of Table 5.8 is that the eye (my eye)
does not measure the plate images of HII regions (in M83)

Table 5.8

Values of dp and dxy for HII regions
in M83 are fit by dxy = mdp
(Profile assumed - 'gaussian')

Plate	I	n	m
3223	>120	27	0.85 ± 0.02
3223	<120	20	0.92 ± 0.03
3223	all	47	0.88 ± 0.02
2918	all	9	0.87 ± 0.03
2886	>120	27	0.86 ± 0.02
2886	<120	16	0.88 ± 0.04
2886	all	43	0.87 ± 0.02
1402	all	25	0.86 ± 0.03
		Mean	0.87 ± 0.03

at their Half Maximum intensity levels. A similar analysis
of stellar data shown in Table 4.10 showed that the eye
(my eye) <u>does</u> measure the sizes of star images at their
Half Maximum intensity levels. The profiles of HII regions
are therefore probably not starlike (gaussian).

5.6   *What Profile?*

The assumption that the HII regions in M83 have
gaussian intrinsic H_α intensity profiles leads to an appa-
rent systematic difference in their sizes as measured from
UKST and AAT plates (Table 5.5) and there is evidence
(Table 5.8) to suggest that this assumption is incorrect.

Tables 5.9, 5.10 and 5.11 show the results of ana-
lysing the data with the assumptions that the intrinsic
profiles are, respectively, 'conical', 'cylindrical' and
'exponential decays'. As before, the reductions involve
applying the relations depicted in Fig. 5.10 to the raw
data in Table 5.3 using the widths of the star profiles as
given in Table 4.10. As before, the data from similar
plate materials were analysed assuming equal errors in
each observation, while the r.m.s. errors from these com-
parisons were used as representative errors in the maximum
likelihood analysis of the data from different plate types.
The results of the latter again proved insensitive to the
exact values of the respective errors.

The results for the data of similar plates are
practically indistinguishable from those in Table 5.4 -
if anything the 'cylindrical' assumption makes the comparisons

Table 5-9

The values of d_o from COSMOS data
of plates x and y are fit by $dy = md_x$
(Profile assumed - 'conical')

x	y	I	n	m	Δm	rms devn.	$\left\|\dfrac{m-1}{\Delta m}\right\|$
3223	2886	>120	30	0.90	0.03	0".58	3.1
3223	2886	<120	37	0.95	0.05	0.82	1.0
3223	2886	all	67	0.93	0.03	0.73	2.5
2918	2886	all	10	0.93	0.04	0.53	1.6
1402	1404	all	36	1.04	0.04	0.66	0.9
1402	3223	>120	27	1.22	0.05		4.5
1402	3223	all	60	1.31	0.04		7.1
1402	2886	>120	35	1.13	0.04		3.7
1402	2886	all	67	1.23	0.04		5.9
1402	2918	all	11	1.28	0.10		2.8
1404	3223	all	27	1.28	0.04		6.7
1404	2918	all	10	1.16	0.05		3.2
1404	2886	all	39	1.09	0.04		2.4

See notes in text to Tables 5-4, 5-5.

Table 5-10

The values of d_o from COSMOS data of plates x and y are fit by $dy=md_x$
(Profile assumed - 'cylindrical')

x	y	I	n	m	Δm	rms devn.	$\left\|\frac{m-1}{\Delta m}\right\|$
3223	2886	>120	30	0.88	0.03	0".77	4.1
3223	2886	<120	36	0.95	0.04	0.97	1.3
3223	2886	all	66	0.92	0.02	0.90	3.3
2918	2886	all	13	0.90	0.50	0.85	2.1
3223	2918	all	6	1.07	0.13	1.20	0.6
1402	1404	all	37	1.06	0.04	0.75	1.7
1402	3223	>120	35	1.46	0.06		7.8
1402	3223	all	66	1.41	0.04		9.4
1402	2918	all	11	1.37	0.08		4.4
1402	2886	>120	35	1.24	0.04		6.3
1402	2886	<120	34	1.41	0.07		6.2
1402	2886	all	69	1.32	0.04		8.5
1404	3223	all	27	1.33	0.04		7.4
1404	2918	all	11	1.26	0.05		4.9
1404	2886	all	38	1.17	0.04		3.9

See notes in text to Table 5-4, 5-5.

Table 5.11

<u>Values of d_0 from COSMOS data of</u>
<u>plates x and y are fit by $dy = md_x$</u>
(Profile assumed - 'exponential decay')

x	y	I	n	m	Δm	rms devn.	$\left\|\dfrac{m - 1}{\Delta m}\right\|$
3223	2886	>120	20	0.88	0.04	0.40	2.9
3223	2886	<120	24	0.92	0.08	0.69	1.1
3223	2886	all	44	0.90	0.04	0.58	2.3
2918	2886	all	12	0.96	0.06	0.42	0.6
1402	1404	all	23	0.94	0.06	0.58	0.9
1402	3223	>120	18	1.01	0.04		0.2
1402	3223	<120	14	1.27	0.12		2.3
1402	3223	all	32	1.09	0.05		1.7
1402	2886	>120	25	0.97	0.05		0.6
1402	2886	<120	16	1.26	0.12		2.2
1402	2886	all	41	1.04	0.05		0.8
1404	3223	all	20	1.21	0.06		3.5
1404	2886	all	27	0.98	0.04		0.5

worse. However, while the systematic difference between
the AAT and UKST data remains under the 'conical' assumption,
and becomes more pronounced under the 'cylindrical' assump-
tion, it is eliminated to some high degree under the assump-
tion of exponential decays for the intrinsic profiles.
Considering the possible saturation effects on plate 3223
as mentioned earlier, the null hypothesis of chapter 5.5
would be accepted from the results of Table 5.11.

While an exponential decay profile may not be totally
optimal in this sense - it was chosen as representing one
part of the possible spectrum of profiles as described in
Ch. 5.3 - the data here are clearly much better represented
by profiles that are leptokurtotic (i.e. peaky).

The exciting stars have been shown (Ch. 5.2) to
contribute somewhat less than 10% of the Hα flux of the
HII region. If they concentrate towards the centre of the
nebula yet still occupy some considerable part of it, say
one half by radius (Van den Bergh 1964, Lucke and Hodge
1970) then the total Hα profile may be better represented
perhaps by a core-and-halo structure like that in Fig. 5.12.
The nebular contribution in this example is of the 'cylin-
drical' type. A 'cone' in its place would produce another
feasible total profile that is becoming similar in shape
to the exponential decay that proved the best fit to the
M83 data. Both total profiles show a leptokurtotic nature
although the nebular components are at extreme ends of the
range of kurtotis that would quantify the morphological
scheme of Chapter 5.3.

Clearly the modelling could be taken further.
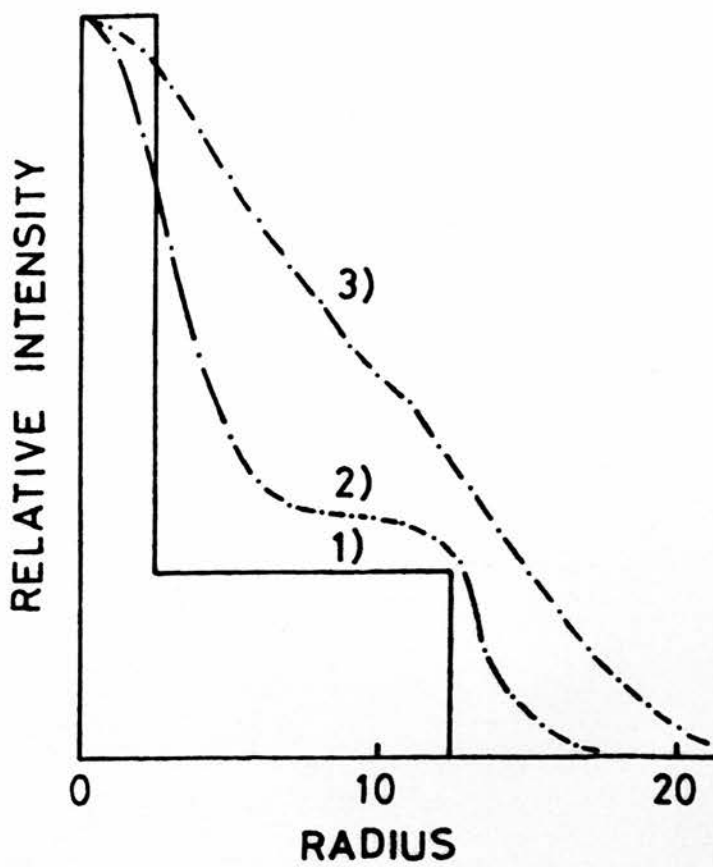
Figure 5.12. Core-halo structure and convolutions with gaussians:

(2) σ gaussian = 2 units
(3) σ gaussian = 4

5.7 *Results V: The Sizes of HII Regions*

If each intrinsic H_α intensity profile has the form

$$I(r) \propto \exp(-r/E)$$

where r is the radius and E the characteristic e-folding dimension, then the FWHM dimension is related to E thus:

$$FWHM \equiv d_o = 2E\ln2 = 1.386E.$$

Assigning a dimension to the HII region based upon a dimension of an H_α profile of this sort is not as straightforward as if the profile had been conical or cylindrical, say. However, from Fig. 5.7d it is seen that the edge of the nebula as defined by its density cut-off lies very close to the point at which $I(r) = 0.01I(o)$, i.e. at $r = 4.61E$. Thus

$$6.65 \, d_o$$

is a good estimate of the diameter of the HII region. Consistent use of any such factor should prove as useful, however.

Table 5.12 gives the diameters of the HII regions in M83 in this scheme. The values given are the means of such values from all the UKST and AAT $H\alpha$ plates. No uncertain, f-class or x-class data was used except where they were the only data available, and contributions to the means of d_o of less than one arc second were given half weight. The number of contributions to each mean dimension is given as the weight (wt). The expected error in the mean values is $(20 \pm 7)\%$ as calculated from those HII regions with weights of 4 or 5.

Table 5.12

The Sizes of HII Regions in M83

No.	Diam. "	Wt.	No.	Diam.	Wt.	No.	Diam.	Wt.
1	10.6	1	41	20.6	4	79	<	3
2	9.3	1	42	18.6	2	80	<	4
3	8.0	1	43	14.1	4	81	16.6	4
4	6.7	1 <	44E	8.6	1	83	20.5	4
6	13.3	1 <	44W	6.0	1	84N	16.6	1
7	11.6	4	45	15.0	5	84S		
8	21.6	4	46	12.6	1 <	84E	7.3	1
9	15.8	4	47E	<	3	85	24.2	3
11	17.4	5	47W	<	1	88	13.7	3
12	11.3	3	48	29.5	5	89	13.3	1
13	14.3	4	49	14.9	3	90	17.3	4
14	12.4	3½	50	12.0	3	91	<	4
16N	7.3	1	51	13.1	3	92	10.0	3
16S	<	1	52	18.8	3	95	10.0	2
17	10.0	2	53	9.6	2	96	9.3	2
18	10.0	1	54	15.0	2	98	18.0	1 <
19N	10.6	1	55	18.0	3	99	8.6	1 <
19S	12.6	1	56N	6.7	2	100	17.7	3
20	13.3	3	56S	7.3	1	101	<	3
22	10.0	2	57	11.6	2	102	9.3	2
23	16.4	3	58	10.6	1 <	103	12.0	4
26	13.3	1	59	11.1	3	104	15.1	3
28	11.1	4	60N	8.6:	1	105	12.1	4
29	10.0	1 <	60S	9.3	1	107	9.3	2
30	15.0	2	61	19.6	2	108	13.0	4
31	<	3	62	16.5	4	109	11.5	3
32	12.6	2	64	19.3	2	110	14.1	4
33	27.9	3	67	21.1	4	111	12.0	4
34	12.6	3	68	11.3	4	112	16.0	3
35	13.1	3	69	10.9	3	113	18.4	3
37	6.0	1 <	70	<	3	114	20.4	3
38	<	3	71	10.6	2	115	13.1	3
39	9.6	2	76	10.6	3	118E	11.3:	1
40	13.3	3	78	12.4	3	118W	8.6:	1

Table 5.12 cont.

No.	Diam. "	Wt.	No.	Diam. "	Wt.
119	12.0	2	300	12.6	2
120N	<	1	302	11.3	1
120S	<	1	306	10.0	1 <
121	12.6	3	310	<	3
124	7.3	1 <	318	<	2
125	10.6	1	320	12.0:	1
127	10.0	2	321	13.0	2
151	12.6	1 <	322	<	2
152	9.3	2	323	<	3
153	13.5	3	325	<	3
155	15.7	3	325	<	3
156	11.3	2	No. of all regions - 94		
157	13.1	3	No. of bright regions - 51.5		

Multiples measured as single entities

No.	Diam.	Wt.	No.	Diam.	Wt.
16	21.3	1	60	26.3	2
19	14.6	1	84	23.3	3
44	15.1	3	118	23.9	2
47	<	2	120	26.3	2
56	16.3	2			

Notes: < in Diam. column indicates Diam < 6"

        < in wt. column indicates that there are more
readings suggesting Diam < 6" than those used
in producing the value of Diam. shown
: uncertain

The data of Table 5.12 is used in plotting the size distribution shown in Fig. 5.12. The data suggest an approximation by a Poisson function

$$ke^{-\mu}\mu^{x}/x!$$

and the upper curve in Fig. 5.12 is such a function with μ = 12.5 (arc seconds) and k such as to normalise the curve. This particular curve is the optimal one of its type in that it minimises the sum of the squares of the deviations from the observed data. The error on μ, defined as that change in the optimal value of μ that increases this sum by 10% is 0.5 arc seconds.

μ should also estimate the peak of the distribution, as indeed it does. The calculation of $\mu_{optimal}$ was repeated with other binning arrangements, including the use of bins 3 arc secs. wide, but the effects were insignificant.

The best fitting Poisson curve to the bright data also has μ = 12''5 $\pm$ 0''5 and is shown by the lower curve in in Fig. 5.12. The agreement between these results gives confidence that a magnitude limited sample of HII regions will be representative in this way.

There are a number (16) of 'faint' regions, and one 'bright' region in the sample measured here that have sizes indeterminately smaller than 6 arc secs, and which cannot be shown in Fig. 5.12. Some fraction of these, indeed of all images, may be stars, but the effect upon the bulk of the distribution by their inclusion will be slight.

Inclusion in the data of those HII regions known to be multiple, but observed to be, and measured as, single
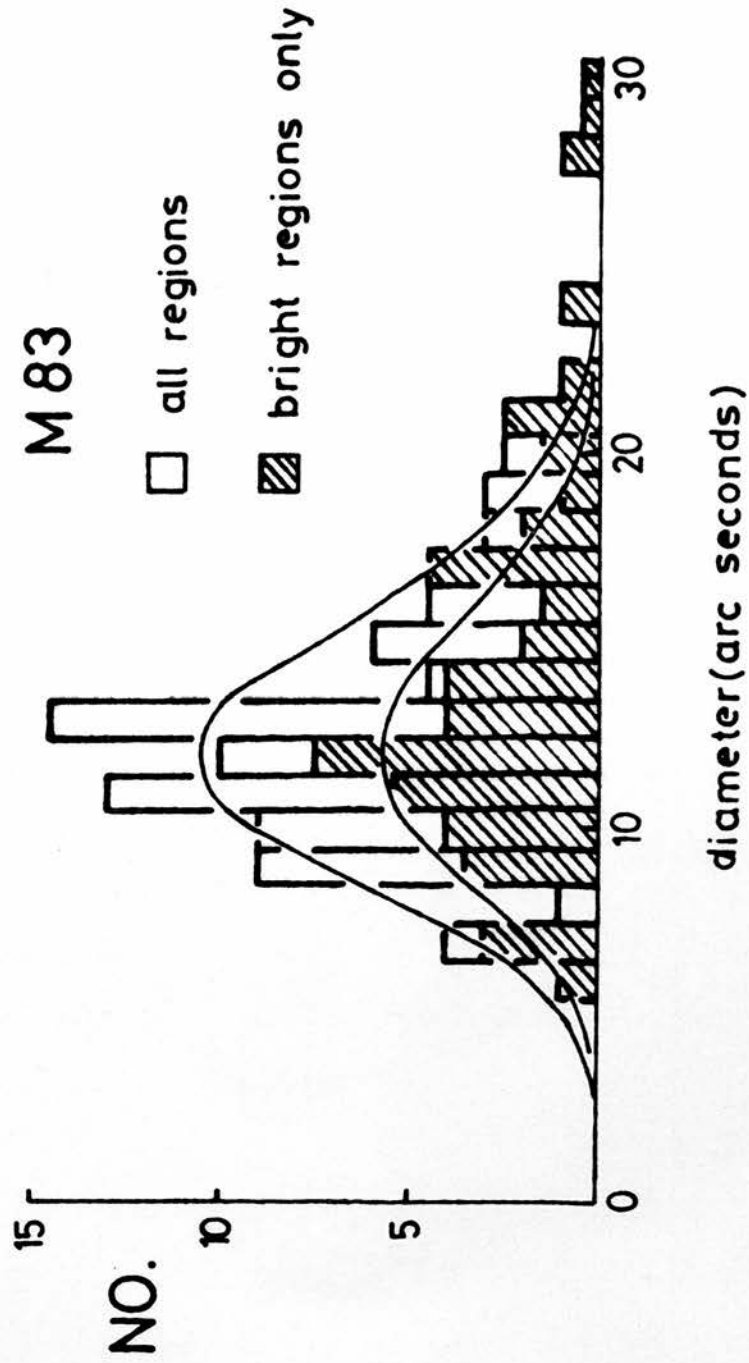
Figure 5.12. The Size Distribution of HII Regions in M83.

entities on some plates has the obvious effect of shifting the distribution to higher diameters. Formally, the optimal values of μ become then

μ = 13.5 $\pm$ 0.5 arc secs, for all data, and

μ = 14.0 $\pm$ 0.5 arc secs, for the bright data only.

This 8 to 12% change in the parameterisation of the distribution should be compared with a change of 3% in $<D>_3$ induced by the same data adjustment. However, the change in μ will be somewhat reduced if the effect of the small regions mentioned above could be quantified.

In the light of this very good approximation of the size distribution for the HII regions of M83, those examined in Chapter 3 may have been better approximated similarly. Note that since an exponential decay is merely a Poisson function with μ = 0, then this has already been done in some cases!

The data for the other galaxies in the present sample (Table 4.1 and Appendix E) have been similarly analysed. Table 5.13 presents the results and Fig. 5.13 the histograms where justifiable.

Many more HII regions were measured in these galaxies than are listed in Table 5.13, as may be deduced from the numbering systems! but proved to have indeterminately small diameters. The values of μ for the best fitting Poisson functions to the size distributions for these galaxies can then only be given upper limits; these may be estimated from the peaks in the distributions.

The bulk of the size distribution for M83 (Fig. 5.12) lies well above the point at which problems of

Table 5.13

Sizes of HII Regions in 9 galaxies

NGC 1097

Region	d_1 μm	diam. "
11	107	21
40	78	11
35	94	16
33	93	16

NGC 1179

Region	d_1 μm	diam. "
7	102	15*
Centre	108	-

NGC 1232

Region	d_1 μm	diam. "	
1	86	12	
2	98	16	
10	85	12	b
16	160	42	*
25	87e	13	b
28	87	13	b
31	138	33	* b
34	87	13	
37	114	22	b
39	140	33	b
40	82	11	b
42	111	21	
46	111	21	b
48	85	12	
49	123	26	
54	93	15	
55	95	15	
101	99	17	b

NGC 1300

Region	d_1 μm	diam. "
2	116	24
17	92	15
18	91	14
19	136	32
20	120	25
22	103	18
U2	101	18

NGC 1313

Region	d_1 μm	diam. "	
1	98	16	
2	140	33	b. sat?
4	101	17	
6	84	12	b
7	174	48	b, sat?
11	121	25	
15	109	20	
155	110	21	
19	186	53	
20	147	37	EW only
21	230	73	b, EW only
22	250	84	EW only
24	90e	14	
25	122	26	sat?
26	124	27	b
27	150:	38:b	
28	204	61	b
29	111:	21:b	
30	138:	33:b	
31	96	16	b
32	110	21	b
41	84	12	b

NGC 1313 cont.

Region	d_1 μm	diam. "	
42	117	24	b
44	82	11	
45	83	11	
54	132	30	
56	83	11	
61	166	45	b
62	109	20	
68	83	11	b
71	101	17	b
73	199	59	b, sat?
74	206	62	b, sat?
75	118	24	b, sat?

NGC 1365

Region	d_1 μm	diam. "	
3	88	13	
5	118	24	
10	101e	17	
12	98	16	b
13	100	17	b
23	94	15	
24	89	13	
26	121e	25	b
30	88	13	b,P3
33	106	19	
37	83	11	b, P8
45	/97	16	
46	83	11	
47	94:	15:	
56	83	11	
57	103	18	b
59	172	47	b
60	153	39	b
65	83	11	b
66	124	26	b
67	121	25	b
68	152	38	b
70	102	17	
U1	99	16	
11	81 ∿	10.5	b, P4

NGC 1566

Region	d_1 μm	diam. "
11	109	18
14	106	17
15	104	16

NGC 2442

Region	d_1 μm	diam. "
1	115e	24

NGC 2997

Region	d_1 μm	diam. "	
1	111	21	
6	103e	18	b
7	83	11	b
11	88e	13	
27	114	22	b
34	86	12	b
41	91	14	
64	128	28	b
79	99	17	
81	95	15	
105	88	13	b

Note * - profile unusual.

Pn - refers to the numbering system of Pagel
et al. (1979)
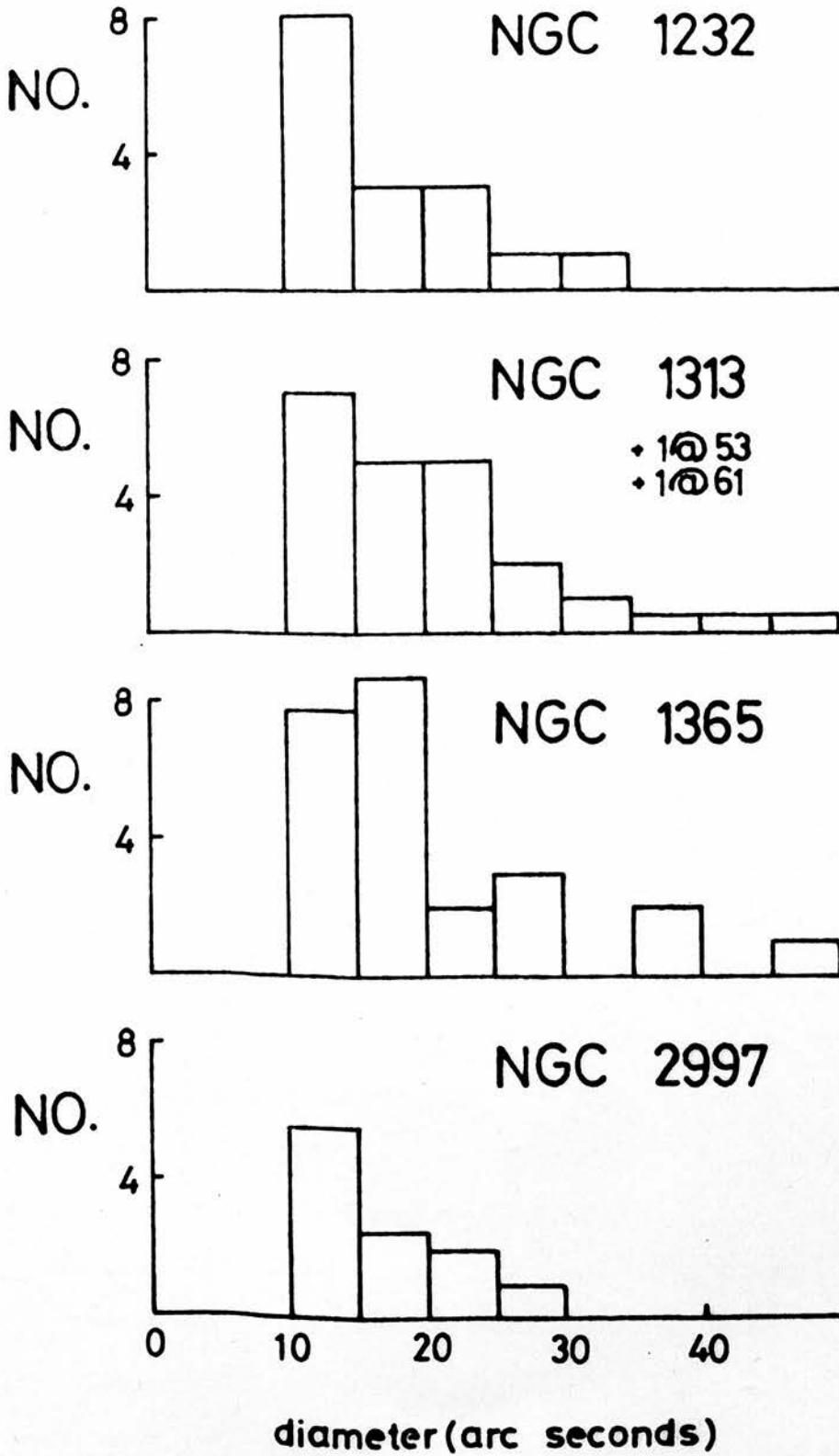
b - the brighter half of those tabulated.

Figure 5.13.   The size Distributions of HII Regions in 4 spiral
galaxies.

completeness in the sampling of small HII regions occur,
but the presence of the 17 small regions mentioned previously
does provoke the thought that the distribution may, in rea-
lity, turn upwards towards zero. Such bimodality in the
HII region size distribution was already encountered as
a possibility in the analysis of the HII region data for
M31 (Ch. 3.7). Such may, however, reflect the difference
between HII regions previously divided by the concept of
'giant' HII region (Mezger 1970). This term was invoked
to differentiate between those distant, radio-bright (Galac-
tic) HII regions that define the spiral arms, and those that
are radio weak - and 'local' in the prevailing context -
and which do not define spiral arms. The optically identi-
fiable galactic HII regions fall mainly into this second
group.

From the maps in Figs. 4.8 to 4.13 the HII regions
in M83 measured here are mainly 'giants', if their arm-
tracing is definitive, and so the distribution in Fig. 5.12
refers principally to 'giants'. The preponderence of
fainter regions amongst those described previously as 'in-
determinately small' may indicate that while the fainter
regions do weakly follow the distribution for the brighter
regions (as the difference of the two sets of data in Fig.
5.12 shows) there may be a considerable quantity of small,
faint HII regions in any galaxy. While the data of Chapter
3 indicates that galaxies with well defined spiral arms
have HII region size distributions that can be well approxi-
mated by Poisson functions with $\mu > 0$, those galaxies
studied therein that do not have well defined spiral arms,

like the Magellanic Clouds (although see Schmidt-Kaler 1977), have size distributions for their HII regions better approximated by Poissons with $\mu = 0$. A correlation between μ and morphological class amongst spiral (and irregular) galaxies may exist, but requires more data to define.

5.8   Discussion

A simple HII region size distribution can be de-
rived from the spectral type - Strömgren radius tabulation
of Osterbrock (1974), the spectral type - stellar mass
tabulation of Conti (1975) and the mass function for early
type stars of Lequeux (1979). The results shown in Table
5.14 can be well fit by an exponential decaying from zero
diameter with an e-fold of about 65 pcs.

While these calculations are for single star excita-
tions in uniform media of density 1 cm^{-3} and support the
speculation above regarding the underlying numbers of
fainter 'non-giant' HII regions, they cannot be expected
to represent the 'giants' of M83. A typical giant HII
region in M83 has a diameter of 225 pcs (≡12.5 arc secs
at 3.70 Mpc, de Vaucouleurs 1979) and a mean electron den-
sity of 500 cm^{-3} (Dufour et $al.$ 1980, Brand et $al.$ 1980).
If the formulation for Strömgren spheres used above
(Osterbrock 1974) is applicable to giant regions also, the
numbers of equivalent O-stars required to maintain a
giant HII region is of the order of $10^5 - 10^6$, many orders
of magnitude greater than the largest collections of such
stars seen more locally (e.g. Lucke and Hodge 1970 for the
LMC, Meaburn 1979, LMC, van den Bergh 1964, M31).

Typical large O-associations contain perhaps 10^3
O-stars spread over hundreds of parsecs (Lucke and Hodge
1970, van den Bergh 1964). (In passing, this makes the
theoretical Hα profile in Fig. 5.11 more appropriate). It
is more reasonable, then, to consider giant HII regions

Table 5.14

A Simple Theoretical Strömgren Sphere
Size Distribution

(1) Size (pcs)	(2) Sp. Type	(3) $\dfrac{M_\ast}{M_\odot}$	(4) $N(M_\ast)$ (kpc^{-2})
216	O5	60	1.05
148	O6	37	2.6
112	O7	28	4.7
102	O8	23	6.9
68	O9	19	10.5
58	O9.5	18	12.3

Columns (1) & (2) Osterbrock (1974) ($N_e = 1$ cm^{-3})

(2) & (3) Conti   (1975) ZAMS

(3) & (4) Lequeux   (1979) (⊙n'h'd)

as aggregates of smaller regions than as single entities excited by a large number of stars. This view has already been expressed by Shields and Searle (1978), for instance, and was found necessary in Ch. 5.2 to explain the constancy of the [NII]/Hα line ratio across the faces of such nebulae.

The computation of a size distribution for giant HII regions then requires the numbers of such stellar associations, their total membership and average densities.

Such data is sparse. Lucke (1974) has presented data for the LMC, but includes stars as late as about A5 in his totals.

The calculation of a theoretical size distribution for giant HII regions would be of some interest in testing theories of O-star formation against observations such as these.

The giant HII regions in any galaxy are clearly more amenable to observation than the others. If their size distribution in M83 is to yield a characteristic parameter it is surely the value of μ, the mean of the best fitting Poisson curve - μ is well estimated by the peak in the distribution. Comparison with data for other galaxies is hardly possible because of the little amount of similar data available, and because of the possible differences in the definition of 'diameter'. However, the data for M33 as presented by Boulesteix et al. (1974). (Ch. 3.8) is perhaps the most useful in this context. They measured the HII regions by eye and reduced these dimensions by equation (3.1) using seeing (d_g) of 4 arc

secs. The HII region size distribution they derived peaks at (12 ± 2) arc secs. (and is remarkably Poissonian!). The position of the peak of the distribution as derived using the assumption of exponential decay profiles can be calculated: This 12 arc secs refers, in the terminology thus far established, to d_0 under a gaussian assumption. With dg = 4" this derived from a profile of FWHM $d_1 = \sqrt{12^2 + 4^2}/$ 0.87 (see Table 5.10) i.e. from $d_1 = 14\overset{''}{.}54$. The value dg = 4" refers to the FWHM of the star profile (Table 4.10) so $d_1/dg = 3.63$, and so, from Fig. 5.10, d_0 (expl. decay assumption) = $10\overset{''}{.}44$, which with the definition of 'diameter' as in Ch. 5.7, gives a size of $69\overset{''}{.}4$. If M33 and M83 can be compared directly via this property, then the distance to M83, $\Delta(M83)$, is given by

$$\Delta(M83) = \frac{69.4}{12.5} \quad \Delta(M83)$$

$$= 4.00 \text{ Mpc or } 4.55 \text{ Mpc}$$

according to the distance to M33 being 720 kpc (de Vaucouleurs 1978d) or 820 kpc (Sandage and Tammann 1974a). The recessional velocity of M83 of 337 km s^{-1} thus implies respective values of H_0 of 84 and 74 kms^{-1} Mpc^{-1}, with associated errors of 22% from the parameter estimation.

6. CONCLUSION

The sizes of HII regions in external galaxies have an important part to play in the determination of the Hubble Constant. The measurement of these sizes from photographic plates was, in the past, followed by reduction to their intrinsic sizes by application of equation (3.1), i.e. assuming their intrinsic forms to be gaussian, like the star profiles. It has been seen here, for M83, that this assumption leads to an apparent systematic effect in the results from different plate materials - HII regions being calculated to be larger from a plate of smaller scale. Such an effect propagates through the distance scale to H_o.

This systematic effect vanished when the analysis was made with the assumption that the intrinsic intensity profiles of the HII regions in M83 were exponential decays. Since giant HII regions are such complex units it is not expected that this, or any other, form of profile will be totally suitable for all regions. However, if the sizes of HII regions are to be used as distance indicators, they must, principally, be free from systematic effects - individual mismatchings will hopefully produce only random errors.

A better understanding of the contribution of the exciting stars to the 'Hα' flux from HII regions would help in the modelling techniques that have been probed here. Again, more detailed information about each and every HII region would be of importance in reducing the random error

element. Future work of this kind must first ascertain the correct assumption about the intrinsic Hα intensity profile - the assumption of a universal intrinsic profile cannot yet be made.

To continue to respond to the stated aims of this work as outlined in Ch. 4.1.:

3) The advantage of machine measurements over eyeball techniques is clear - no information as to which is the correct intensity profile to use can be forthcoming from the latter.

4) Once the correct profile is ascertained the results from all UKST Hα and AAT Hα plates proved to be in good agreement. There is no set of standard conditions to which future work needs referring. The use of red (R) plates is not recommended at this stage. Analysis of the data from plate UKST R1350 gave

$$d_o \text{ (R1350)} = (0.89 \pm 0.04) \, d_o \text{ (mean Hα)}$$

where d_o is the FWHM of the intrinsic (exponential decay) profile and "mean Hα" refers to the mean dimension from all the Hα plates, UKST and AAT, as given in Table 5.12.

5) The size distribution of HII regions in M83 is well approximated, where the data is well determined, by a Poisson function of mean 12.5 arc secs ($\equiv$207 pcs at 3.41 Mpc or 235 pc at 3.88 Mpc). The 'bright' subset of this data gives the same result, which gives encouragement that a brightness limited sample will

be representative of the whole population. The 'population' in this sense is the 'giant' HII regions. A correlation between the parameterization of this best fitting Poisson function and the galaxy type may exist, but more data of a similar nature is required. The size distributions for the other galaxies in the present sample may also be fit by Poisson functions, but with the parameter, μ, close to zero it is ill-determined - there are numerous completeness problems in sampling the small, non-giant HII regions. Theoretical size distributions for giant HII regions are hampered by ill-known distributions and star densities for O-associations. Their construction and comparison with observational data of this kind should prove useful in studies of galactic structure and star formation.

6) We have seen how an exponential decay might well describe the intrinsic intensity profile of the HII regions in M83, how such may yet be the superposition of stellar and nebular components and how this latter may still take many forms defined on a sequence enumerated by kurtosis. Further close examination of each HII region and more specific modelling of the total 'Hα' output is required before a more specific statement can be made about the physical structure of an HII region. Only then may a more accurate determination of its size be made.

ACKNOWLEDGEMENTS

APPENDIX A

The Principle of the Uniformity of Nature (PUN), the Distance Scale hierarchy and the "Spread-the-Risks" philosophy

Edwin Hubble (1936, p. 23) wrote that speculations about the universe that survived the tests of astronomical exploration were those that "... *were based on the principle of the uniformity of nature - the assumption that any large sample of the universe is much like any other. The principle was applied to stars ... Since the stars were ... far away ... they must necessarily be very bright. The brightest object known was the Sun. Therefore, the stars were assumed to be like the Sun, and distances could be estimated from their apparent faintness.*"

Similarly, one must assumed, until it is known otherwise that "*Objects which share some observable characteristic properties (say, the period and light curve for cepheids) are identical in all their other properties.*" (de Vaucouleurs 1977a). The whole idea being that such properties of objects nearby are measured in some fundamental way and compared with the same properties of more distant objects to determine the distance of the latter. Then by adopting the latter group as calibrators for some other property, the cycle can be repeated to reach out further into the Universe.

Blindly assuming the PUN, though, is risking the possibility of unseen factors affecting the measured properties. Such factors include chemical composition,

age and evolution, for instance. The possibility of a distance determination based on several indicators being biased in the same direction by all such effects is thought to be small by those advocating the above mentioned philosophy, and they encourage the use of many indicators at all levels in the hierarchy. (de Vaucouleurs 1976, 1977a, van den Bergh 1975a, b, 1976). Their stance is typified by the case of the cepheids as primary distance indicators. Sandage and Tammann (1974a) used cepheids as their sole primary indicator. They run the risk of the cepheids in the calibrating domain (the Galaxy) being different from those elsewhere; and there is substantial evidence that this is the case (Arp and Kraft 1961, Gascoigne and Kron 1965, Gascoigne 1969, Martin *et al*. 1979). Those in the "spread-the-risks" group use novae, RR Lyrae stars, bright stars and others. (*op. cit.*)

Cepheids are undoubtedly important indicators because of their brightness and P-L-? relation, but using them alone could systematically affect the distance scale.

APPENDIX B

The error in the HII region distance to a galaxy

From eqn (3.9) in chapter 3.2

$$\log R = \frac{b - \log \alpha + 5a + ma}{1 + 5a} \ . \qquad (3.9)$$

If a and b have associated errors ϵ_a, ϵ_b, then

$$\log R + \Delta \log R = \frac{b + \epsilon_b - \log \alpha + (5+m)(a+\epsilon_a)}{1 + 5a + 5\epsilon_a}$$

$$= \frac{[b - \log \alpha + (5+m)a] \left[1 + \dfrac{\epsilon_b + (5+m)\epsilon_a}{b - \log \alpha + (5+m)a}\right]}{[1+5a] \left[1 + \dfrac{5\epsilon_a}{1 + 5a}\right]}$$

$$\div \log R \left[1 + \frac{\epsilon_b + (5+m)\epsilon_a}{(1+5a)\log R}\right]\left[1 - \frac{5\epsilon_a}{1+5a}\right]$$

so $\Delta \log R$
$$\approx \frac{\epsilon_b + (5+m)\epsilon_a - 5\epsilon_a \log R}{1 + 5a}$$

$$= \frac{\epsilon_b + \epsilon_a(5+m - 5 \log R)}{1 + 5a} \qquad \text{which}$$

from (3.8)
$$= \frac{\epsilon_b + M\epsilon_a}{1 + 5a} \qquad \text{and which is}$$

$$= \frac{\Delta \log D}{1+5a} \qquad \text{from (3.6)}$$

Dr. Brand kindly assisted me with this calculation.

APPENDIX C

Data Handling and Computer Programming

In its mapping mode COSMOS (chapter 4.2) produces transmission values for every measured position of a plate. With a datum point every eight microns, coverage of an area one inch square requires 100K of storage capacity. Thus it is convenient to use magnetic tape as storage and to read and manipulate the data sequentially. The magnetic tapes produced by COSMOS were taken to the SRC's laboratories at Daresbury and the computing was done on their ICL 1906A and IBM 360/195 computers via a GPO telephone link to ROE. Amongst the available peripherals was an FR80 graphical device which produced the originals of many of the figures shown herein.

Programs were written in FORTRAN. The data is arranged into blocks of 1024 representing a 128 x 8 grid on the plate as shown:

897	898	.	.	.	.	.	1024
769	.	.	.	.	.	.	896
.	.	.	.	.	.	.	.
129	130	.	.	.	.	.	256
1	2	3	.	.	.	127	128

Normally North is up and East to the left.

If the above was the first block of data, the next block would be for a similar area north of block 1 and the next north of that and so on, until the end of that column. Subsequent 'columns' of data are for areas sequentially to the right. The columns are separated by end-of-column blocks, a header block contains "housekeeping" information e.g. plate

number, tape number, step size... etc., and an "end-of-tape" block completes the tape.

It was convenient to work with areas 2 columns (256 steps) by 32 blocks (256 steps), being defined by the location of the bottom left hand corner within the measured area. Thus, as in Fig. E-6, say, (8,7) means 8 columns in from the left and 7 x 16 blocks up from the bottom.

When larger areas have been used for display here, the 256 x 256 array was maintained and the data suitably compressed.

The programs have many common features - the ability to initialise I/O devices, read the relevant blocks into arrays and to convert the transmissions into relative intensities via the calibrations described in paragraph 4-4.

Identification of stars and HII regions is made by comparing the Hα plate with a suitable continuum plate and their positions in the COSMOS (x,y) frame can then be easily determined. For M83 equatorial coordinates of four stars in the field were determined and these may be used to determine accurate coordinates within the field.

The contour program

For each specified intensity contour level, I_c, the intensities of each group of four grid points forming a square are compared with I_c. If all these are greater or less than I_c no contour passes through that square. Otherwise, the intersection of contour and sides is determined by a linear weighting scheme, and the intersections joined by a straight line.

The profile program

The end points of a cut line are specified and the positions on that line of points an integral number of step sizes from one end are calculated. The intensity value assigned to each of these points is then a weighted combination of those at the grid points surrounding it. Some of these programs are based on pre-existing routines of Dr. Zealey.

APPENDIX D

Identification of HII Regions

In chapter 4 it is postulated that HII regions and stars have different intensity profiles when measured on photographic plates. To see whether one could make such a distinction 'at-a-glance' a program was written to present an intensity picture of an area of plate. An example of such a display is shown in fig. D-1. It is part of M83 as it appears on plate AAT 1402. The difference between HII regions of the size and type present in this frame and the object labelled as and previously identified as a star is quite striking, as is the multiplicity in region 84.

Although the technique was not adopted as routine here it may prove useful in the future.
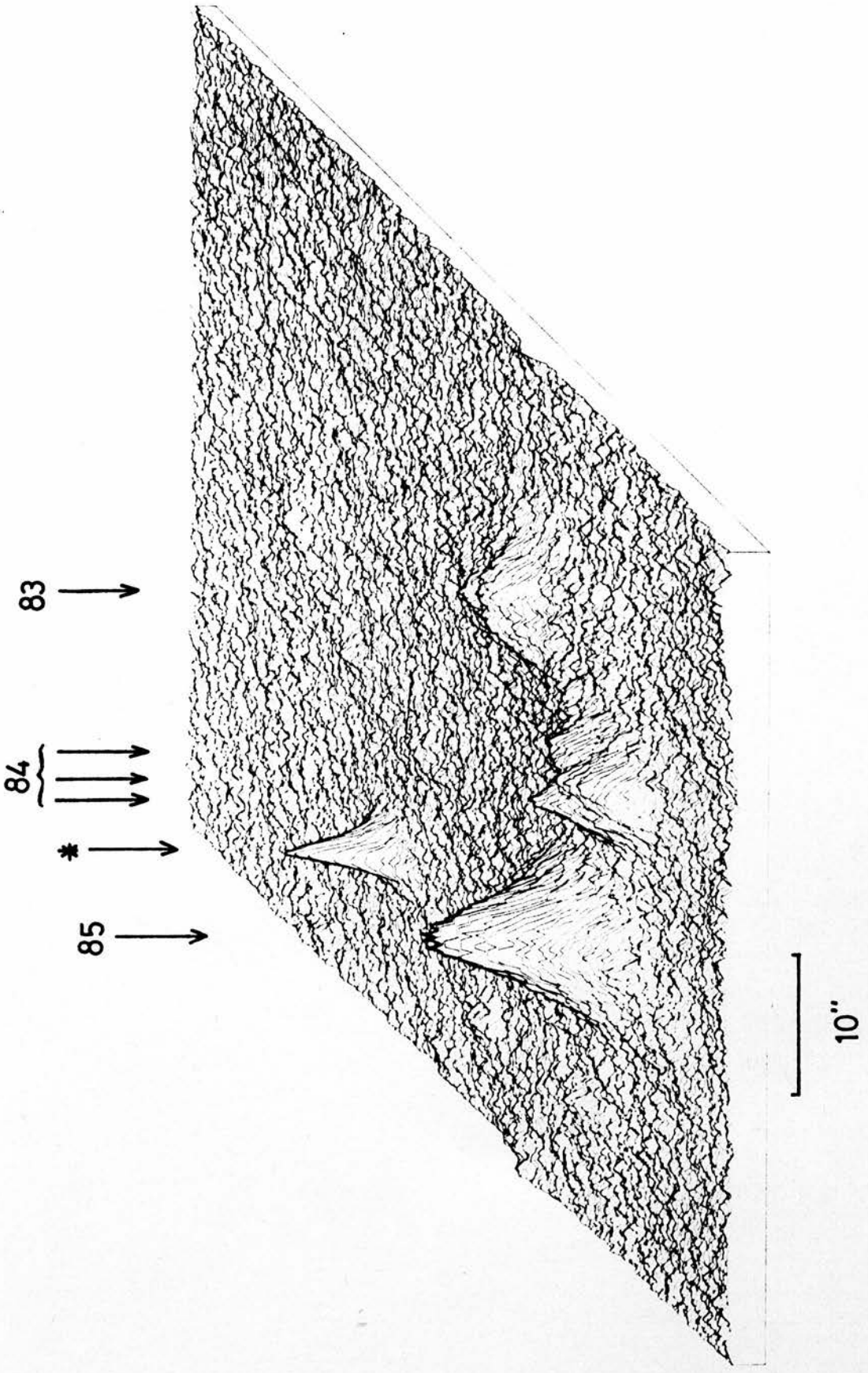
Figure D-1: Intensity Relief map of part of M83 on plate AAT 1402.

APPENDIX E

Presented here are intensity contour maps of the galaxies in Table 4.10, except for M83. Marked on them are most of the stars and HII regions listed in the accompanying tables. The maps have North to the top and East to the left. Contouring was done with constant increments of relative intensity. The positions in the tables are given in mms from the nominal galactic centre, with X and Y increasing to the West and North respectively. (1mm = 67.15 arc secs).
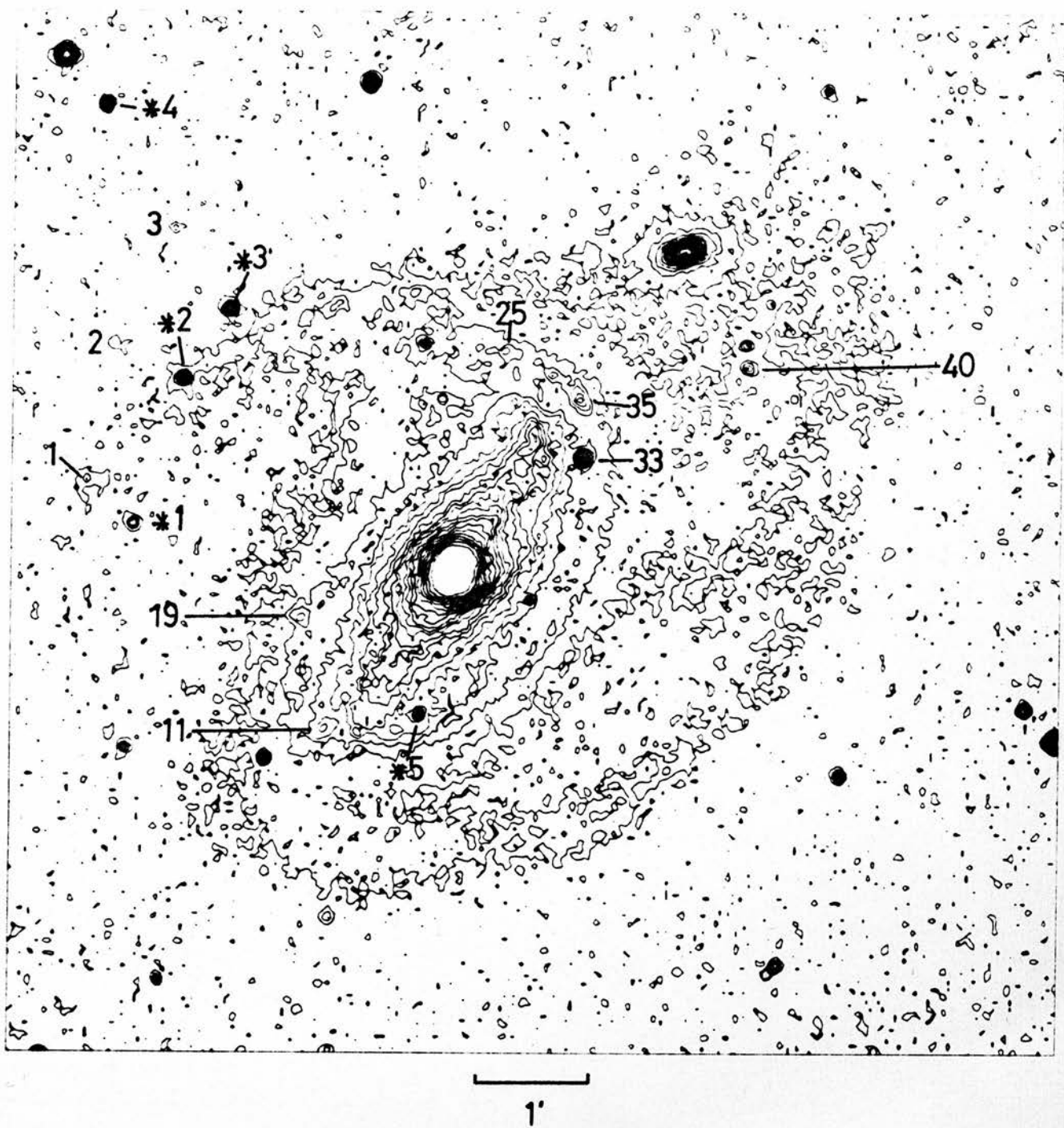
Figure E-1. NGC 1097 on UKST plate Hα 2579.
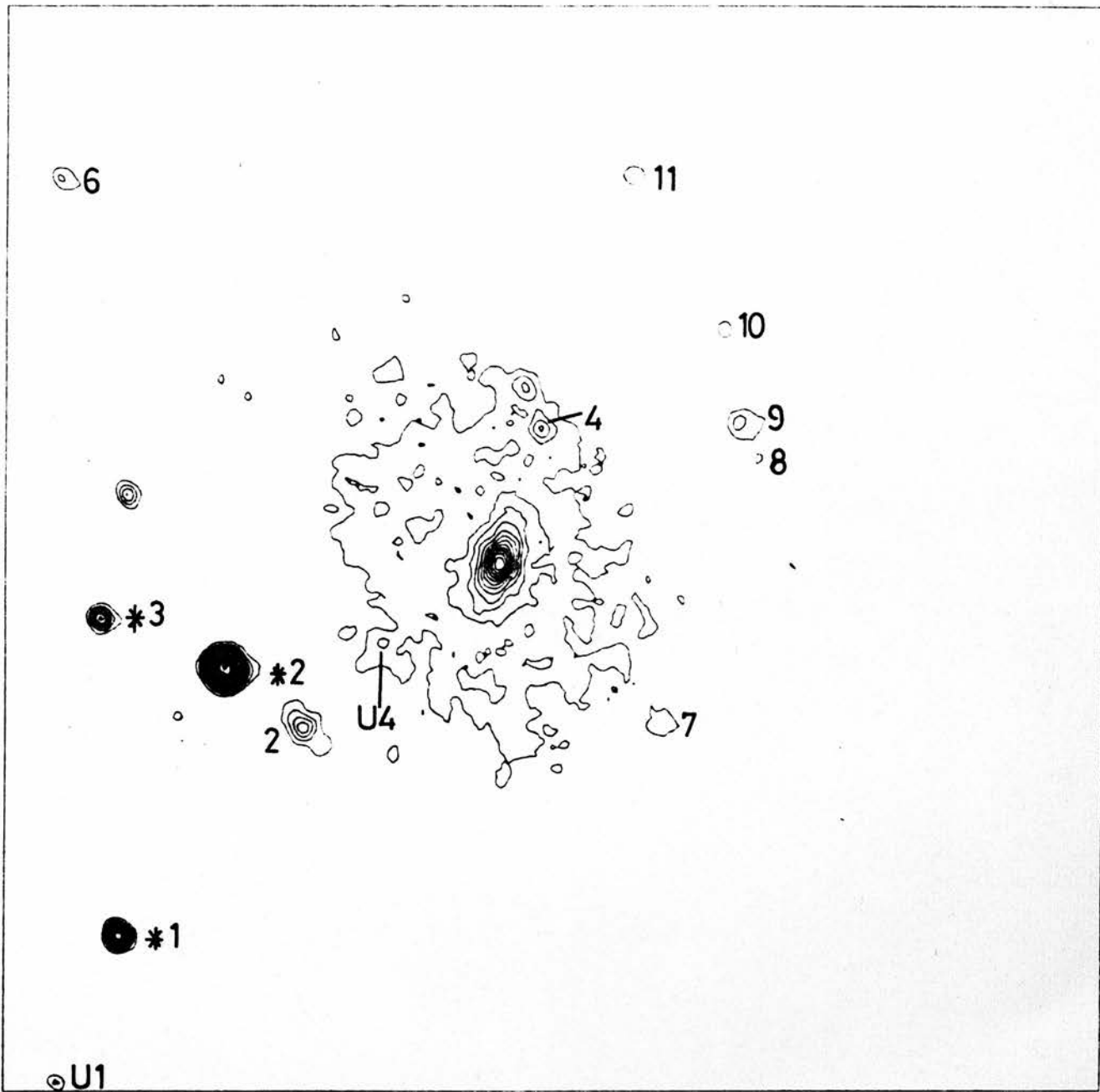
Figure E-2. NGC 1179 on UKST plate Hα 2600.
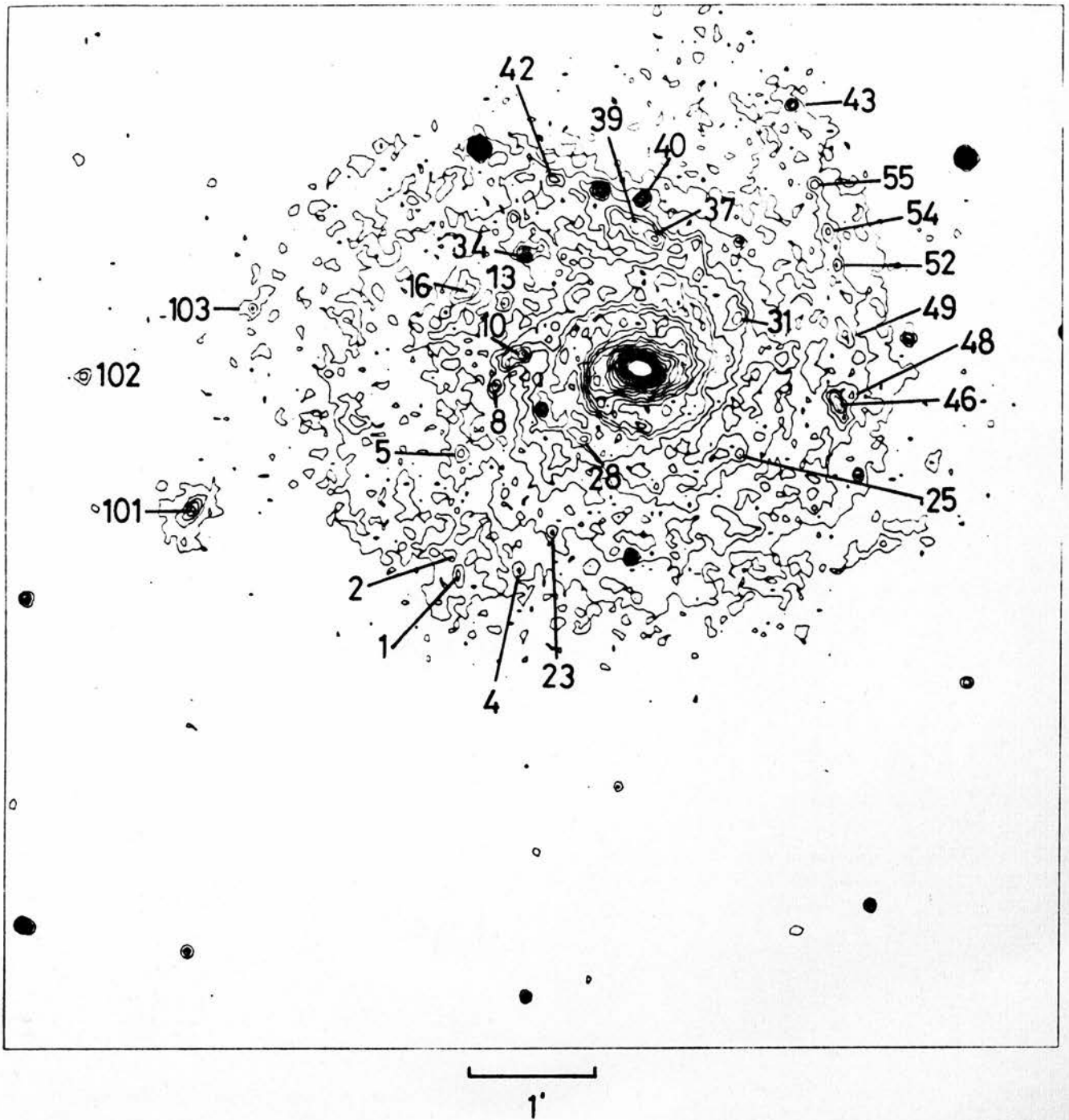
Figure E-3. NGC 1232 on UKST plate Hα 2600.
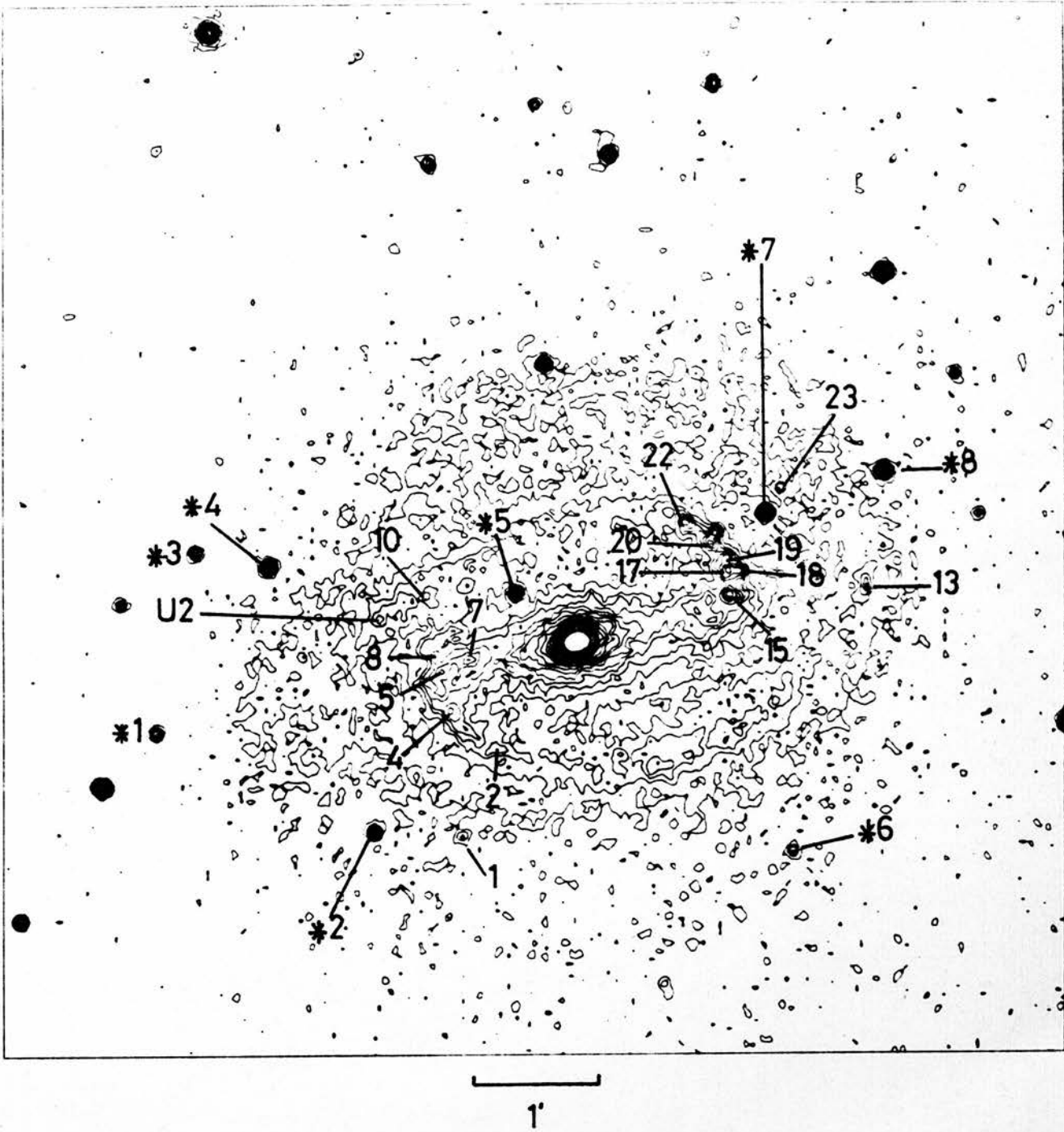
Figure E-4. NGC 1300 on UKST plate Hα 2600.
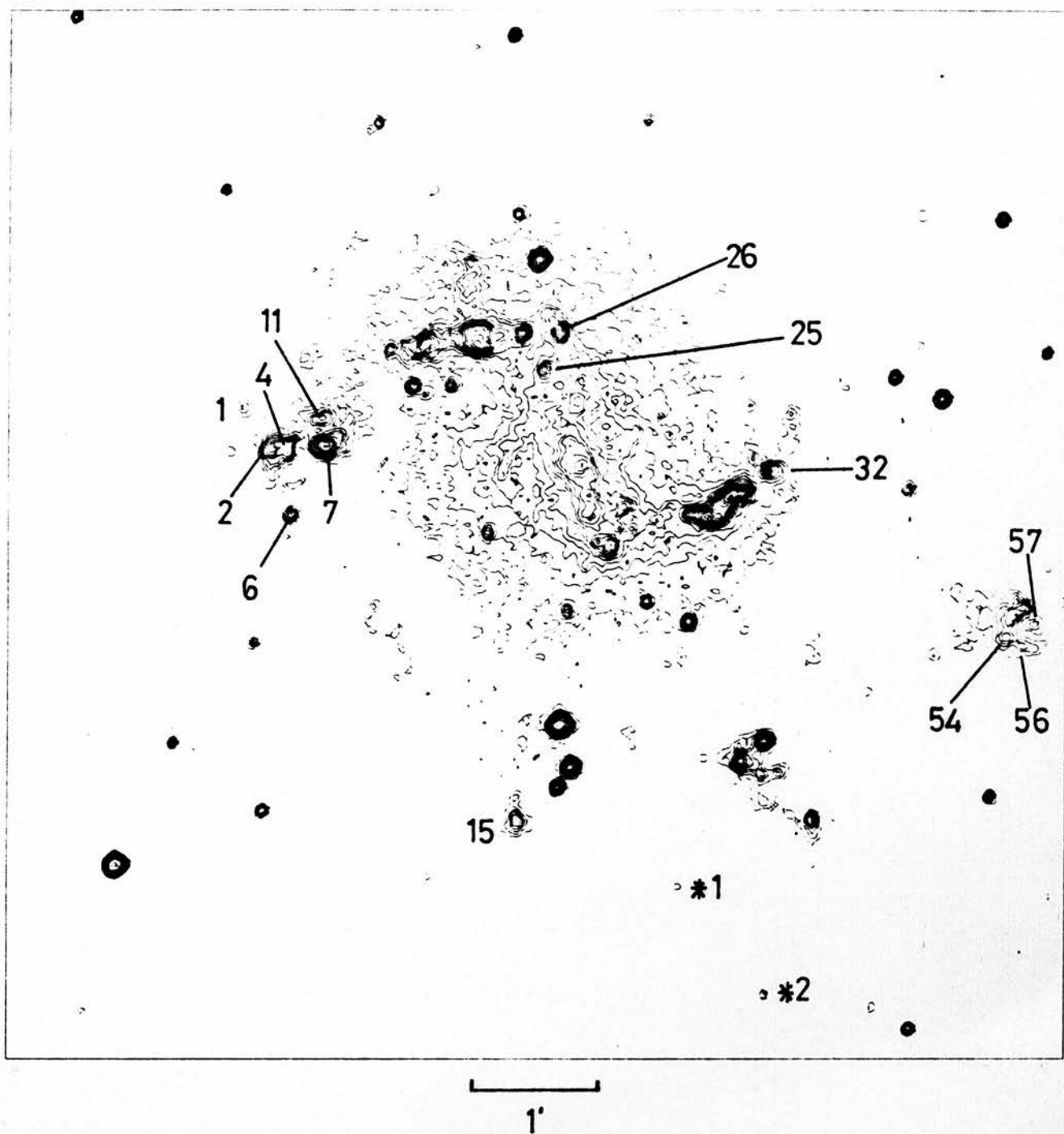
Figure E-5. NGC 1313 on UKST plate Hα 2595.
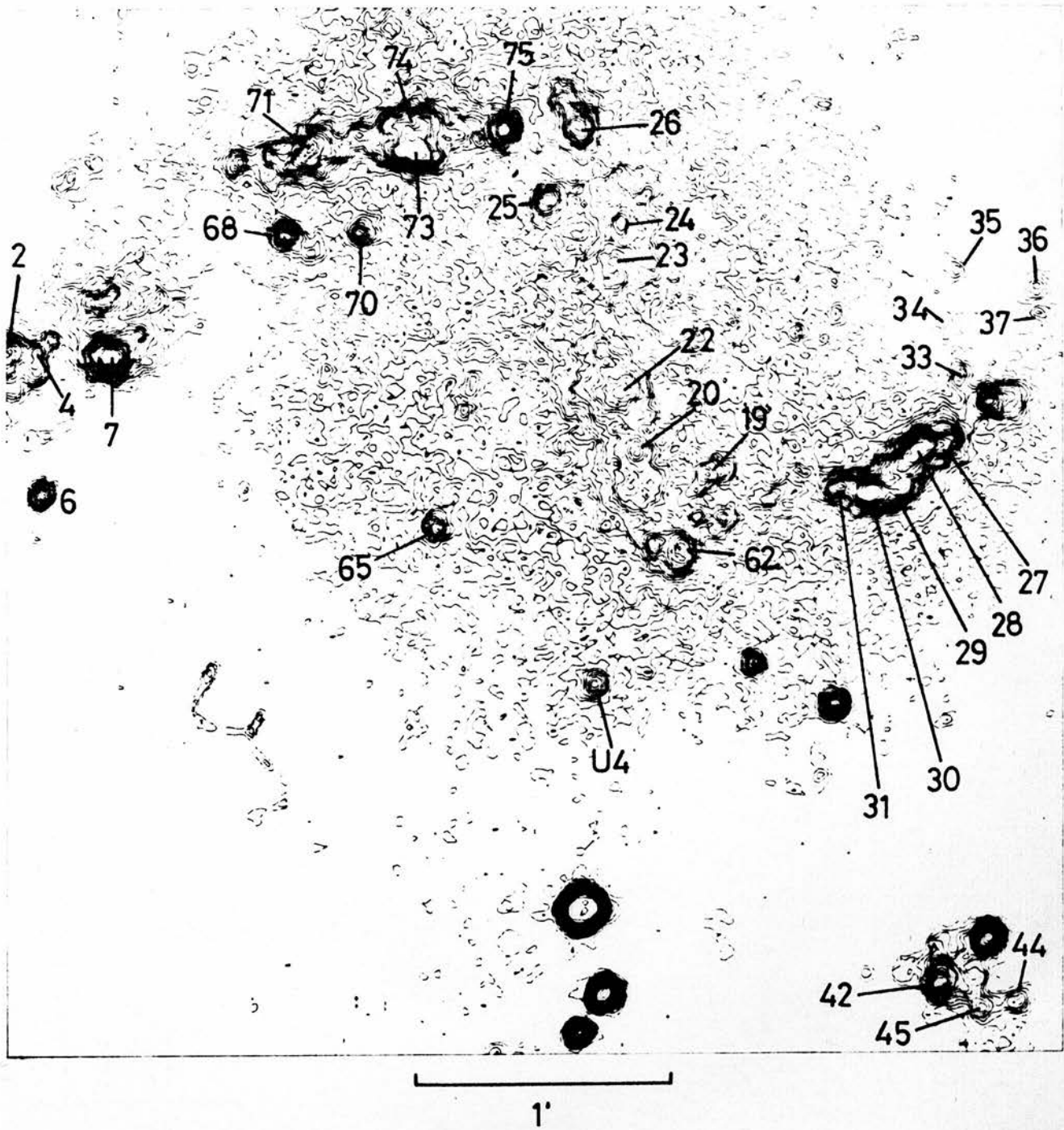
Figure E-6. NGC 1313 on UKST plate Hα 2595.
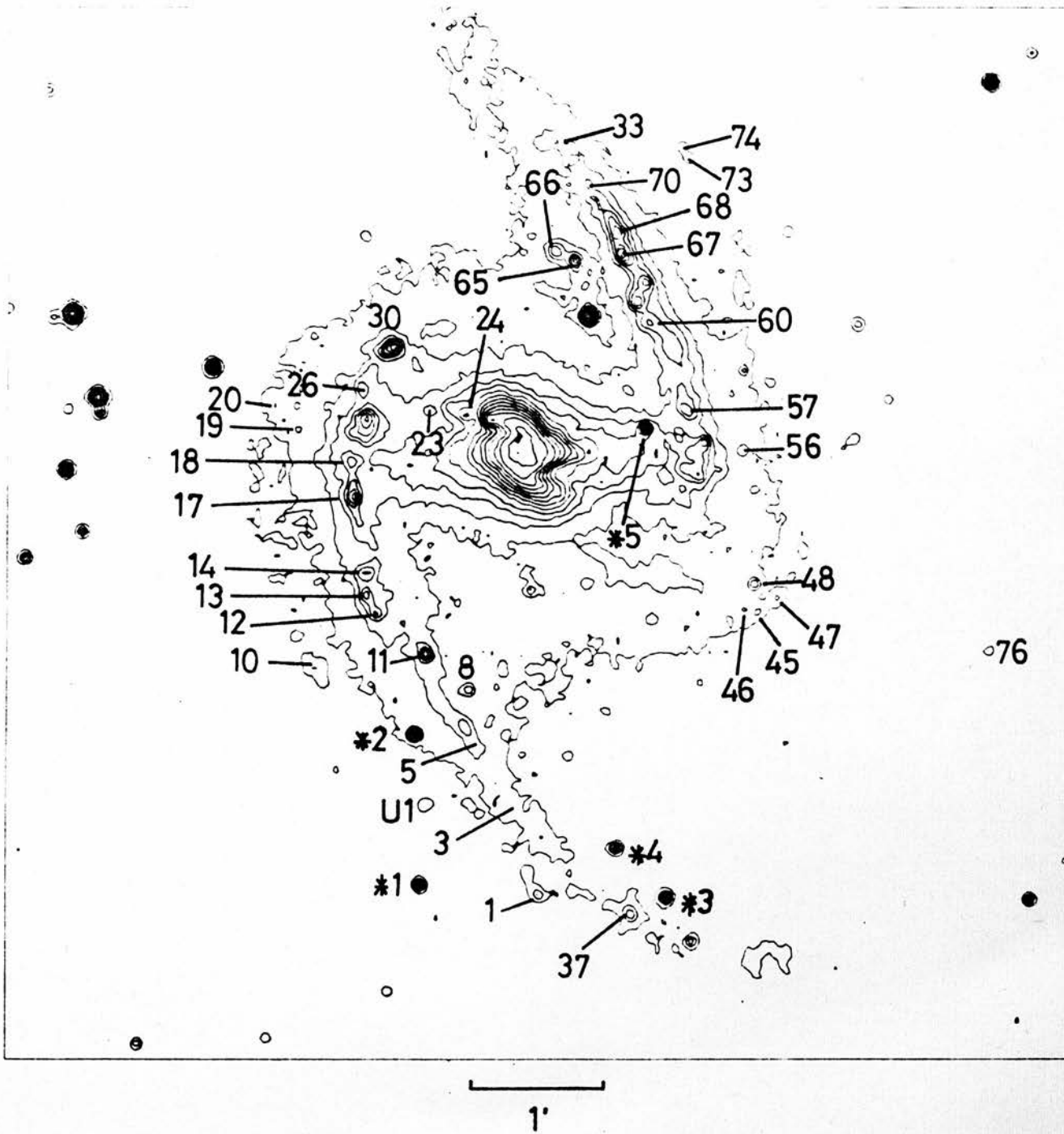
Figure E-7. NGC 1365 on UKST plate Hα 2606.
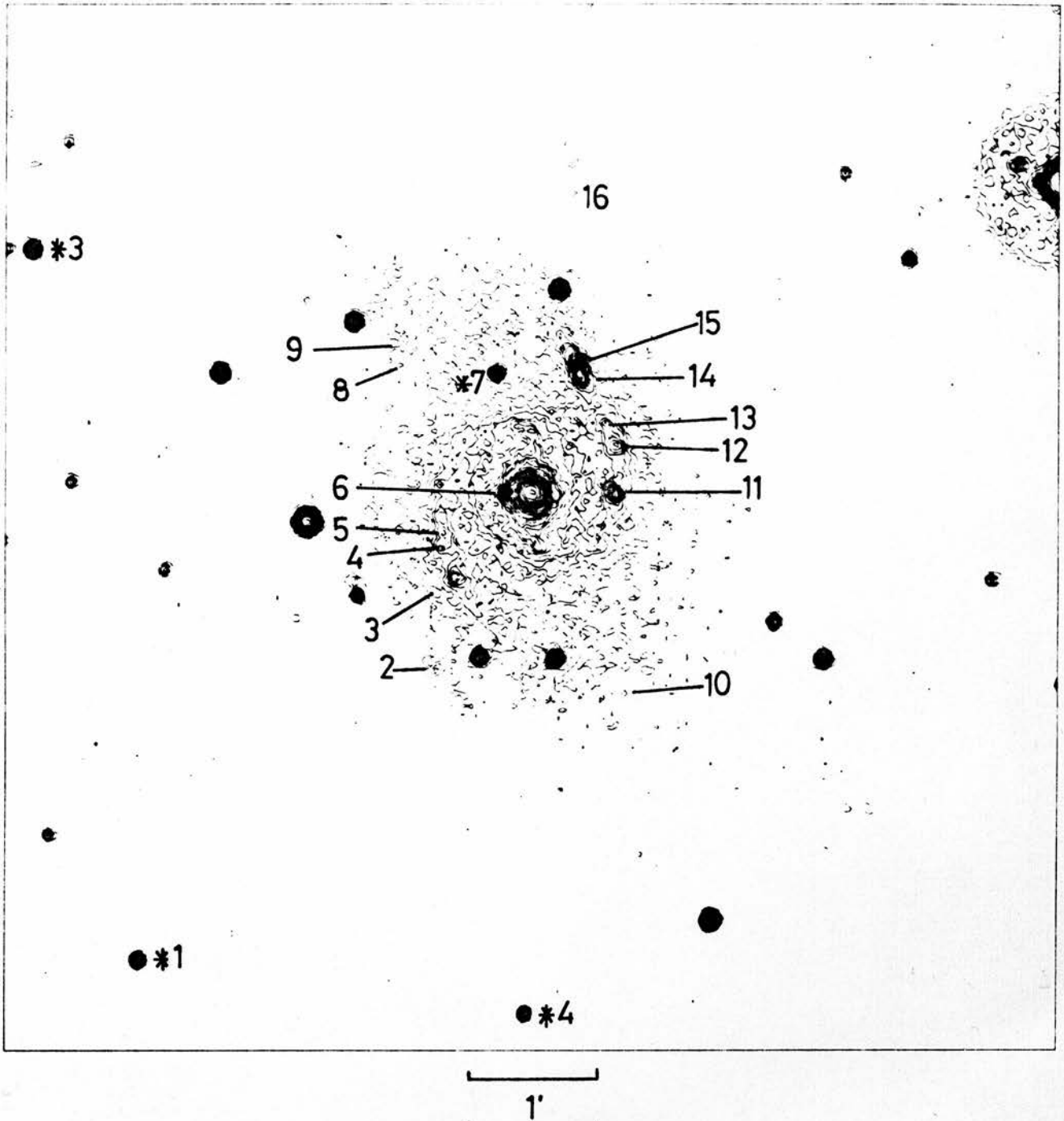
Figure E-8. NGC 1566 on UKST plate Hα 2683.
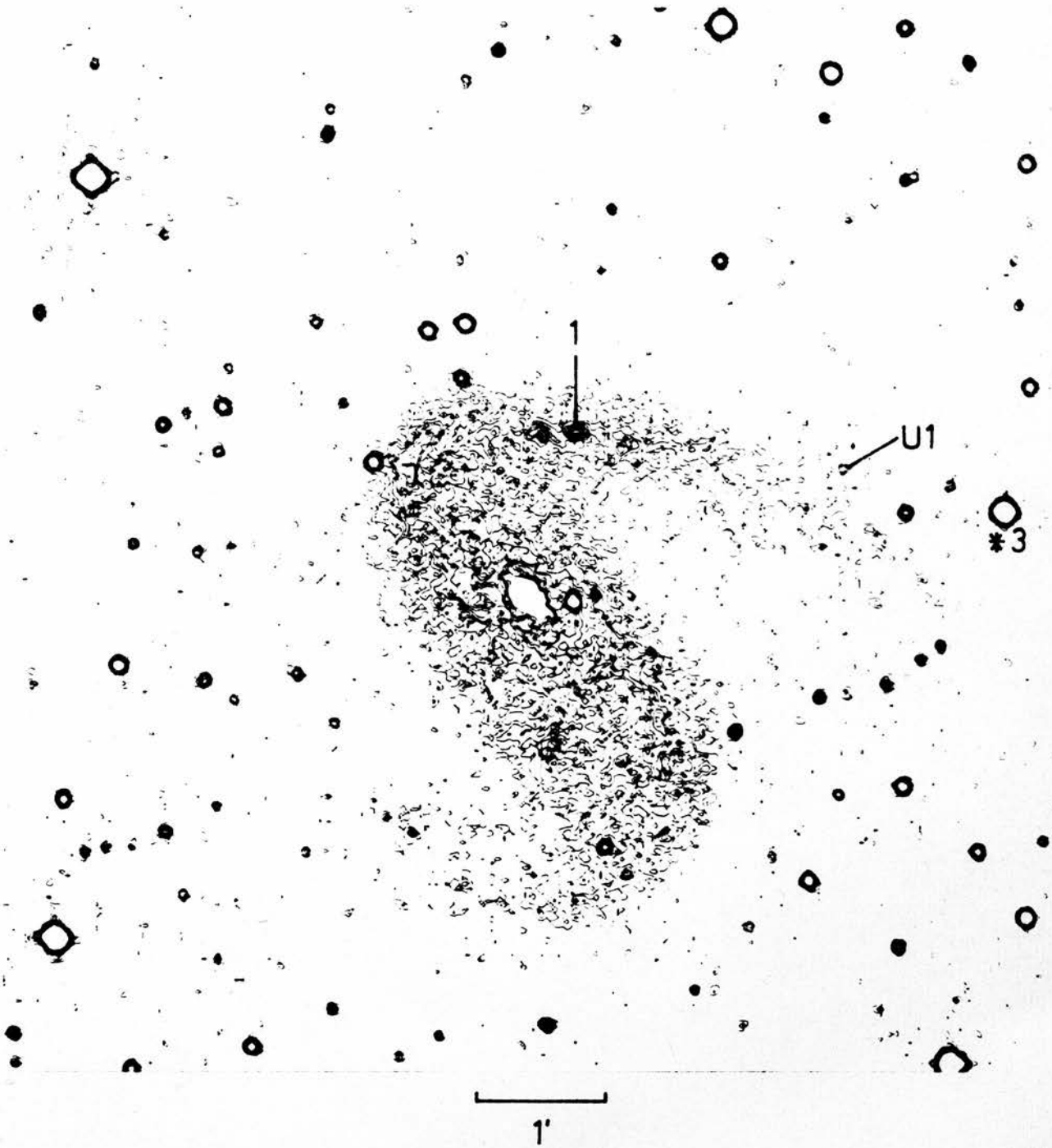
Figure E-9.   NGC 2442 on UKST plate Hα 2871.
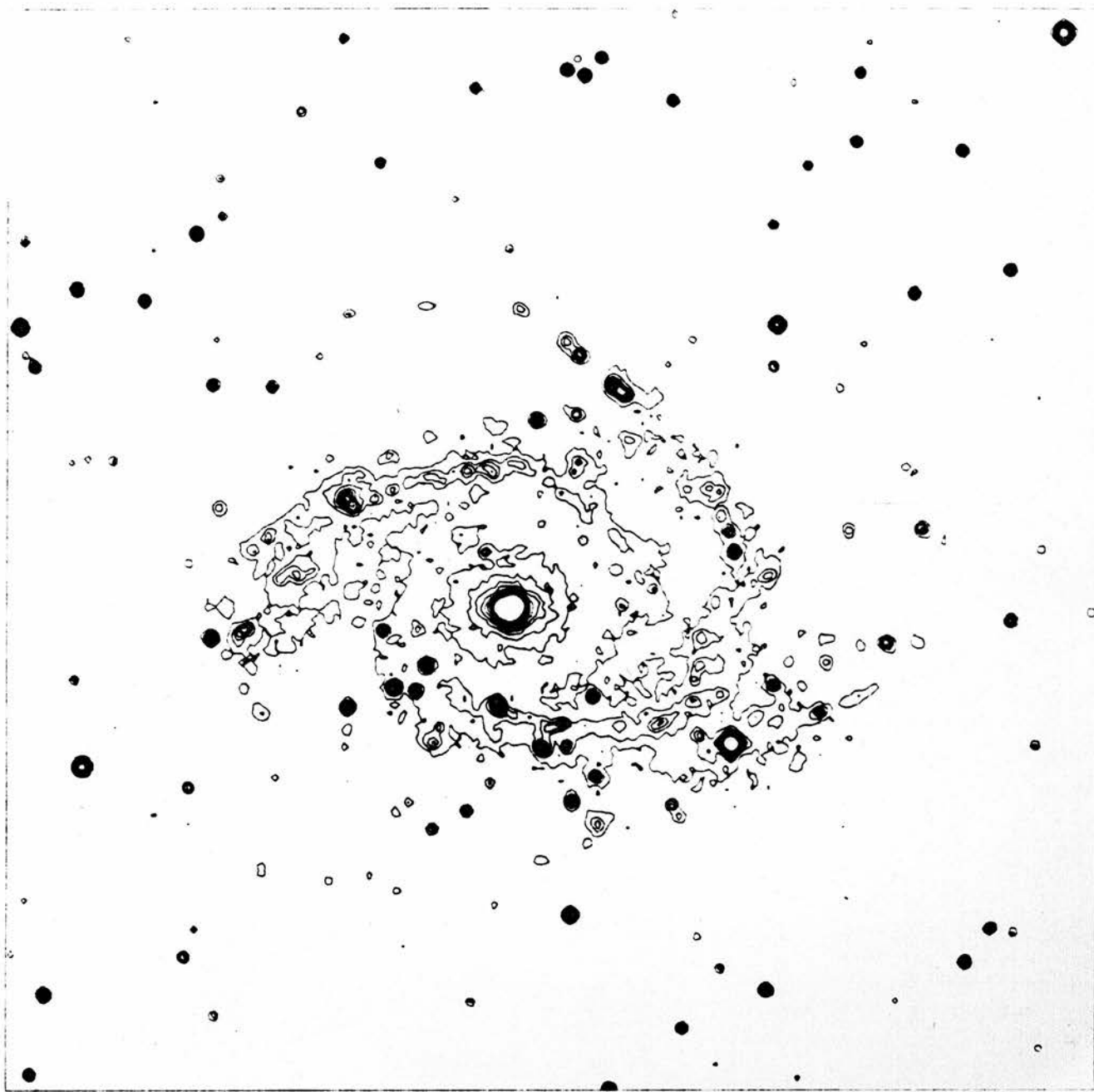
Figure E-10. NGC 2997 on UKST plate Hα 2937.
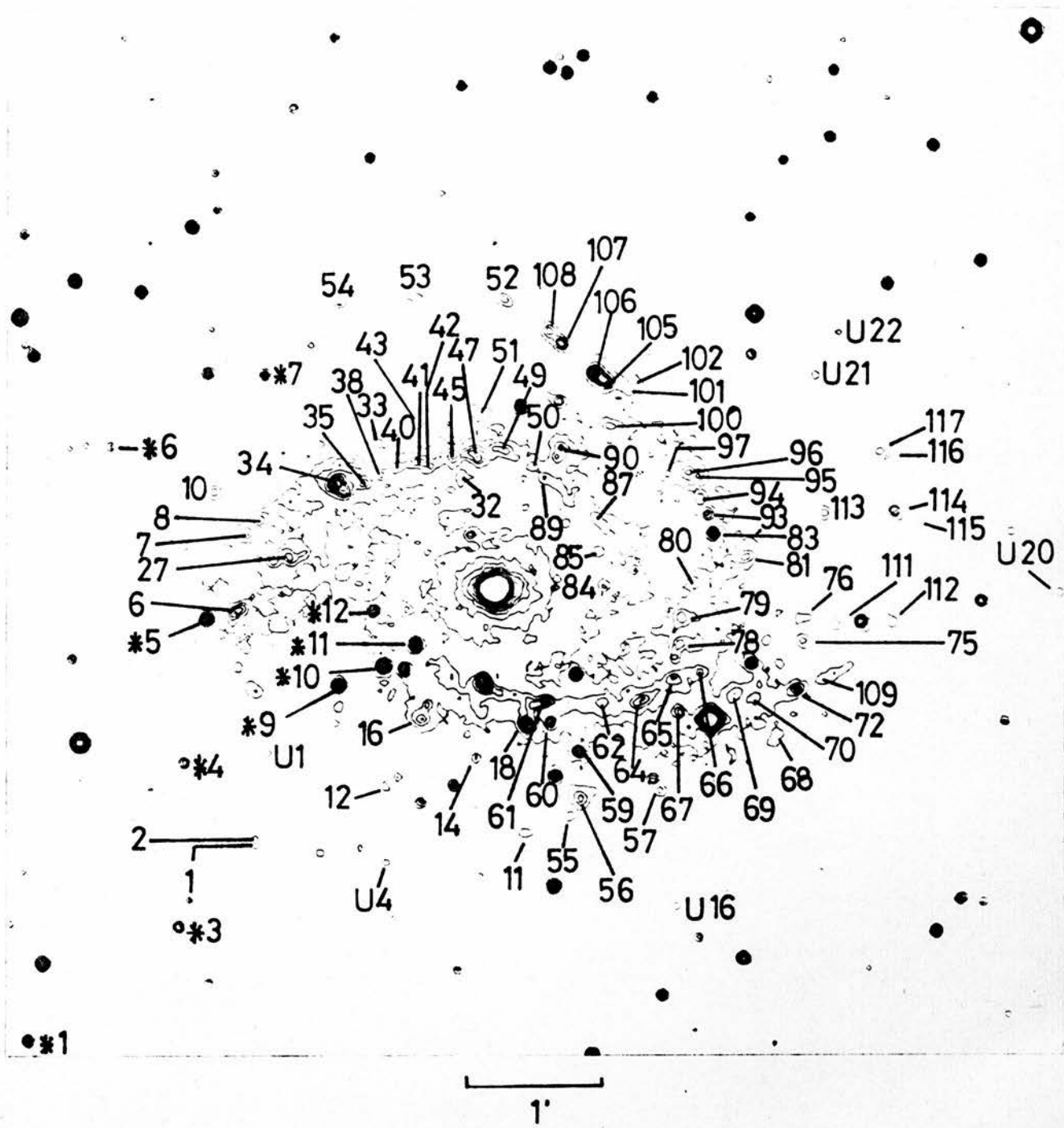
Figure E-11. NGC 2997 on UKST plate Hα 2937.

Table E-1

Positions of HII regions and stars in the field of NGC 1097

No.	X	Y	No.	X	Y
1	-2.78	0.67	25	0.26	1.70
2	-2.67	1.74	26	-0.32	2.17
3	-2.19	2.65	27	-0.98	2.04
4	-0.96	-3.79	29	0.64	-2.05
5	-1.19	-3.46	30	1.10	-2.10
6	-0.97	-2.74	31	1.10	-1.95
7	-1.00	-2.57	33	0.99	0.86
8	-1.18	-2.81	35	0.96	1.31
9	-1.24	-2.95	37	1.46	1.38
10	0.50	-2.16	39	2.62	1.32
11	-1.00	-1.26	40	2.26	1.58
12	-0.75	-1.30		Stars	
13	-0.42	-1.29	*1	-2.50	0.34
14	-0.92	-1.22	*2	-2.11	1.47
15	-0.77	-1.10	*3	-1.75	2.03
16	-0.68	-0.91	*4	-2.74	3.62
17N	-1.12	-0.81	*5	-0.27	-1.16
17S	-1.14	-0.89			
18N	-1.14	-0.52			
18S	-1.12	-0.81			
19	-1.20	-0.40			
20	0.57	0.93			
21	0.50	0.90			
22	-0.25	1.26			

Table E-2

Positions of HII regions and stars in the field of
NGC 1179 and in the field of NGC 2442

No.	X	Y	No.	X	Y
	NGC 1179			NGC 2442	
2	-0.74	-0.61	1	0.33	1.26
U1	-1.66	-1.95	U1	3.04	0.70
U4	-0.42	-0.28		Stars	
4	0.14	0.50	*1	1.16	-0.04
6	-1.64	1.45	*2	3.80	-0.49
7	0.59	-0.59	*3	3.69	0.65
8	0.94	0.39			
9	0.87	0.52			
10	0.82	0.88			
11	0.48	1.46			
	Stars				
*1	-1.43	-1.40			
*2	-1.04	-0.38			
*3	-1.49	-0.19			

Table E-3

Positions of HII regions in NGC 1232

No.	X	Y	No.	X	Y	No.	X	Y
1	-1.38	-1.62	31	0.75	0.39	101	-3.46	-1.10
2	-1.47	-1.45	32	0.46	0.74	102	-4.30	-0.05
3	-1.58	-1.44	34	-0.78	0.94	103	-2.99	0.48
4	-0.94	-1.58	35	0.77	0.98			
5	-1.38	-0.66	37	0.10	1.01			
7	-2.42	-0.04	39	-0.18	1.19			
8	-1.10	-0.15	40	0.02	1.32			
9	-0.99	0.06	41	-0.31	1.39			
10	-0.90	0.11	42	-0.70	1.48			
11	-1.42	0.04	43	1.17	2.06			
12	-1.50	0.44	104	1.20	0.91			
13	-1.04	0.50	U1	2.54	-2.46			
16	-1.36	0.58	44	1.87	-1.37			
19	-1.77	1.31	U2	2.26	-0.74			
20	-0.02	-1.80	46	1.53	-0.28			
21	-0.38	-1.54	47	1.63	-0.22			
22	-0.04	-1.47	48	1.66	0.07			
23	-0.68	-1.28	49	1.58	0.25			
25	0.78	-0.68	50	2.06	0.23			
26	0.14	-0.92	105	3.28	0.29			
27	-0.02	-0.79	52	1.51	0.81			
28	-0.43	-0.54	53	1.49	0.94			
29	-0.76	-0.33	54	1.45	1.07			
30	0.00	-0.45	55	1.34	1.42			

Table E-4

Positions of HII regions in NGC 1300

No.	X	Y	No.	X	Y
U1	-2.18	-0.13	18	1.24	0.52
U2	-1.51	0.18	19	1.13	0.63
U3	-1.43	0.07	20	1.01	0.75
1	-0.90	-1.50	22	0.81	0.91
2	-0.60	-0.83	23	1.54	1.19
4	-1.00	-0.53	30	2.76	0.98
5	-1.06	-0.24	31	2.57	2.06
7	-0.86	-0.14	32	-1.17	0.43
8	-1.11	-0.13			
9	-0.95	0.02		Stars	
10	-1.18	0.34	*1	-3.24	-0.70
U4	0.30	0.88	*2	-1.55	-1.47
U5	0.35	0.88	*3	-2.94	0.70
U6	0.84	-0.89	*4	-2.38	0.59
11	1.88	-0.55	*5	-0.48	0.37
12	1.51	-0.47	*6	1.65	-1.64
13	2.22	0.40	*7	1.43	0.98
14	2.46	0.60	*8	2.37	1.30
15	1.16	0.34			
16	1.22	0.34			
17	1.14	0.54			

Table E-5

Positions of HII regions and stars in the field of NGC 1313

No.	X	Y	No.	X	Y	No.	X	Y
1	-2.59	0.44	24	0.00	0.64	54	3.29	-1.35
2	-2.40	0.10	25	-0.30	0.74	56	3.50	-1.40
3	-2.69	0.09	26	-0.17	1.01	57	3.50	-1.25
4	-2.25	0.14	27	1.24	-0.22	59	3.44	-1.14
5	-2.20	0.20	28	1.16	-0.24	60	3.36	-1.05
6	-2.22	-0.41	29	1.06	-0.43	61	0.24	-0.04
7	-1.97	0.14	30	0.98	-0.41	62	0.13	-0.62
8	-1.86	0.22	31	0.86	-0.38	63	-0.06	-0.54
9	-1.79	0.32	32	1.44	-0.06	U3	0.52	-1.09
10	-1.77	0.38	33	1.33	0.05	U4	0.11	-1.12
11	-2.00	0.35	34	1.27	0.24	64	-0.10	-1.16
13	-1.45	0.90	35	1.31	0.45	65	-0.71	-0.54
14	-0.56	-2.82	36	1.62	0.39	66	-0.60	-0.07
15	-0.47	-2.74	37	1.62	0.28	67	-0.58	0.03
15S	-0.45	-2.78	38	0.80	1.11	68	-1.30	0.58
16	-0.50	-2.60	39	1.44	-2.64	69	-1.20	0.53
U2	1.62	-2.72	41	1.79	2.72	70	-1.02	0.61
17	0.28	-0.52	42	1.23	-2.31	71	-1.20	0.94
18	0.40	-0.52	44	1.52	-2.40	73	-0.78	0.72
19	0.34	-0.32	45	1.40	-2.42	74	-0.80	1.04
20	0.06	-0.26	46	1.38	-2.31	75	-0.46	1.00
21	0.00	-0.07	47	0.95	-2.28	76	-0.86	1.56
22	0.02	0.11	49	0.82	-1.22	77	-1.01	1.60
23	-0.04	0.47	51	1.74	-1.46	*1	0.75	-3.29
						*2	1.44	-4.14

Table E-6

Positions of HII regions and stars in the field of NGC 1365

No.	X	Y	No.	X	Y	No.	X	Y
1	0.13	-3.46	26	-1.24	0.46	U5	0.79	0.44
3	-0.18	-2.60	27	-1.41	0.52	59	1.13	0.80
4	-0.19	-2.49	28	-1.16	0.62	60	0.95	0.97
5	-0.35	-2.30	29	-1.60	0.86	65	0.38	1.44
8	-0.40	-1.86	30	-1.00	0.78	66	0.24	1.52
9	-1.54	-1.79	32	-0.60	0.94	67	0.75	1.50
10	-1.60	-1.69	U3	-1.22	1.64	68	0.71	1.68
U1	-0.73	-2.77	33	0.12	2.38	69	0.33	2.05
U2	-1.43	-2.50	37	0.79	-3.62	70	0.48	2.06
11	-0.74	-1.59	42	2.02	-2.27	71	0.43	2.24
12	-1.13	-1.29	43	0.97	-1.33	72	0.23	2.38
13	-1.20	-1.14	44	0.48	-1.05	73	1.25	2.26
14	-1.04	-1.15	45	1.80	-1.28	74	1.20	2.34
15	-1.20	-0.97	46	1.69	-1.25	76	3.58	-1.58
16	-1.26	-0.58	47	1.94	-1.24	77	2.44	0.06
17	-1.30	-0.38	48	1.77	-1.06		Stars	
18	-1.31	-0.11	49	0.58	-0.27	*1	-0.78	-3.39
16N	-1.36	-0.51	50	1.21	-0.31	*2	-0.82	-2.22
17N	-1.30	-0.26	51	1.34	-0.10	*3	1.10	-3.48
19	-1.73	0.15	52	1.22	-0.15	*4	0.74	-3.09
20	-1.91	0.34	54	1.28	-0.03	*5	0.92	0.16
23	-0.72	0.30	55	1.38	0.06			
24	-0.44	0.26	56	1.67	-0.01			
25	-0.24	0.22	57	1.23	0.30			

Table E-7

Positions of HII regions and stars in the field of NGC 1566

No.	X	Y	No.	X	Y
1	-3.88	2.55		Stars	
U1	-4.06	2.95			
2	-0.74	-1.40	*1	-3.05	-3.66
3	-0.84	-0.77	*3	-3.87	1.90
4	-0.70	-0.41	*4	-0.05	-4.06
5	-0.69	-0.31	*7	-0.27	0.93
6	-0.19	-0.01	*5	-0.39	-1.28
7	-1.86	3.62			
8	-1.02	1.01			
9	-1.09	1.17			
10	0.71	-1.55			
11	0.64	-0.01			
12	0.64	0.37			
13	0.55	0.55			
14	0.37	0.88			
15	0.34	1.01			
16	0.31	2.33			
17	2.53	-2.91			

Table E-9

The field of NGC 2997

No.	X	Y	No.	X	Y	No.	X	Y
1	-1.86	-2.02	35	-1.02	0.82	62	0.82	-0.90
2	-1.90	-1.82	36	-1.23	0.97	63	1.01	-0.82
U1	-1.75	-1.29	38	-0.90	0.87	64	1.11	-0.88
6	-2.00	-0.18	40	-0.76	0.94	65	1.35	-0.71
7	-1.91	0.43	41	-0.61	0.98	66	1.58	-0.66
8	-1.81	0.52	42	-0.51	0.95	67	1.41	-0.98
9	-1.79	0.56	43	-0.62	1.28	68	2.15	-1.20
10	-2.19	0.75	44	-0.42	1.01	69	1.81	-0.85
11	0.23	-1.90	45	-0.33	1.03	70	1.99	-0.86
U4	-0.12	-2.24	46	-0.22	1.04	72	2.32	-0.80
205	-0.22	-1.97	47	-0.14	1.01	73	2.19	-0.53
12	-0.86	-1.54	49	0.09	1.06	75	2.36	-0.42
14	-0.14	-1.39	50	0.27	0.94	76	2.34	-0.23
U9	-1.23	-1.31	51	-0.07	1.36	77	1.36	-0.55
15	-1.22	-0.93	52	0.06	2.26	78	1.41	-0.44
16	-0.58	-1.03	53	-0.66	2.29	79	1.42	-0.24
18	0.24	-1.06	54	-1.23	2.22	80	1.52	0.03
19	0.29	-0.91	U16	1.39	-2.48	81	1.91	0.24
26	-1.37	-0.07	55	0.58	-1.78	82	1.95	0.26
27	-1.61	0.25	56	0.66	-1.64	83	1.66	0.42
29	-0.38	0.55	57	1.26	-1.58	84	0.81	0.00
32	-0.28	0.82	59	0.63	-1.27	85	0.75	0.29
33	-1.18	0.75	60	0.41	-1.06	209	1.75	-0.45
U11	-1.59	0.68	61	0.39	-0.88	210	1.72	-0.33
34	-1.24	0.81				211	1.81	0.18

Table E-9 (cont.)

Positions of HII regions and stars in the field of NGC 2997

No.	X	Y	No.	X	Y
87	0.75	0.55	113	2.53	0.58
89	0.36	0.85	114	3.07	0.58
90	0.47	1.02	115	3.22	0.48
93	1.62	0.56	116	3.01	1.02
94	1.56	0.69	117	2.94	1.05
95	1.54	0.86	U21	2.45	1.65
96	1.46	0.89	U22	2.62	1.98
97	1.30	0.87		Stars	
100	0.86	1.23	*1	-3.60	-3.54
101	1.00	1.54	*2	-2.43	-2.63
102	1.06	1.60	*4	-2.40	-1.35
105	0.83	1.60	*5	-2.23	-0.23
106	0.73	1.68	*6	-2.98	1.10
107	0.50	1.90	*7	-1.78	1.66
108	0.40	2.00	*9	-1.22	-0.75
109	2.51	-0.73	*10	-0.88	-0.62
110	2.60	-0.68	*11	-0.62	-0.44
111	2.61	-0.29	*12	-0.95	-0.18
112	3.04	-0.26			
U20	4.34	-0.03			

APPENDIX F

FWHM

For a regular singularly peaked profile as shown
in Fig. F-1 the Full Width at Half Maximum is a relatively
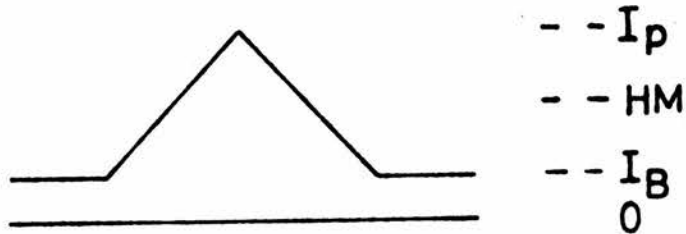simple quantity to determine.

Fig. F-1   A 'normal' profile

I_p is the peak intensity, I_B the intensity of the
background, HM lies at a level halfway between, and FWHM is
the width at that level.

A typical difficult case for determination is shown
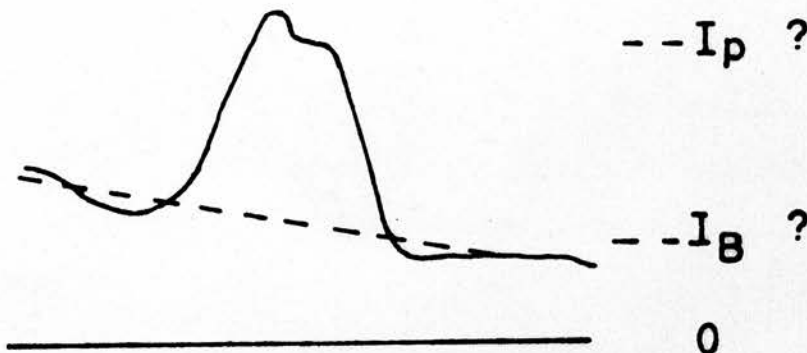in Fig. F-2.

Fig. F-2   A 'difficult' profile

The choices of background are indicated around the
point I_B. The range of values of the HM intensity is, at
least, half that of I_B. The selection of the peak intensity,

I_p, is often confused by the occurrence of one pixel with transmission one less than those surrounding it. This quantization of the transmission levels is exaggerated on the intensity scale, and the effect upon HM is serious. To determine the likely errors involved, region 61 in M83 as seen on AAT 1402 (Fig. 5-2) was chosen for its typification of the above problems.

Possible allocations of relative intensity to the parameters I_p and I_B are

EW I_p = 2456 unambiguously

I_B = 636 or 522

NS : I_p = 2457 or 2349

I_B = 804 or 628 or 716

giving in their various combinations FWHM's of

EW : 321, 360 (μm)

NS : 328, 359, 340, 343, 384, 363 (μm)

with an average of 350 $\pm$ 32 (half range)

So, roughly a 10% error in a single FWHM determination may be expected for a region like this. Although with fainter regions ($\#$ 61 is one of the brightest in M83) the transmission quantization problem is reduced, the background problem remains and overall errors cannot be expected to be less than 10%.

APPENDIX G

Star Profile Data .$\overset{(+)}{.}$.

... in the fields of

a) NGC 1097 on Hα 2579

$\star$	I	I_B	d_1
1	175	192	54
2	261	191	67
3	266	191	69
4	248	186	64
5	162	262	51
		Mean	61 ± 8

b) NGC 1313 on Hα 2595

$\star$	I	I_B	d_1
1	77	260	70
2	128	260	54
		Mean	62 ± 8

c) NGC 1300 on Hα 2600

$\star$	I	I_B	d_1	d_p	d_{xy}	$R_{p,xy}$
1	103	162	56	50	57	-0.13
2	106	163	62	57	63	-0.10
3	91	163	61	56	52	0.07
4	179	163	70	65	78	-0.18
5	146	188	65	60	57	0.05
7	174	176	68	63	75	-0.17
			64	59	64	-0.08
		Means	±5	±5	±11	±0.11

(†) See key to table 4.10 for explanation of symbols.

d)   NGC 1365 on Hα 2606

*	I	I_B	d_1	d_p	d_{xy}	$R_{p,xy}$
1	128	146	63	58	65	-0.11
2	158	160	68	63		
3	133	155	63	58	70	-0.19
4	113	.148	63	58	67	-0.14
5	121	220	73	69	65	0.06
			66	61	67	-0.10
		Means	±5	±5	±5	±0.11

e)   NGC 1566 on Hα 2683

*	I	I_B	d_1	d_p	d_{xy}	$R_{p,xy}$
1	169	63	71	66	83	-0.23
3	83	63	82	78	85	-0.09
4	93	66	72	67	88	-0.27
5	170	70	77	73	85	-0.15
7	150	72	71	66	—	—
			75	70	85	-0.18
		Means	±5	±5	±2	±0.08

f)   NGC 2442 on Hα 2871

*	I	I_B	d_1
1	162	200	67
2	79	140	51
3	175	135	67
			62
		Mean	±9

g) <u>NGC 2997 on Hα 2937</u>

*	I	I_B	d_1	d_p	d_{xy}	$R_{p,xy}$
1	31	19	51	44	63	-0.36
3	39	19	48	41	63	-0.42
4	30	20	47	40	67	-0.50
5	60	22	61	56	70	-0.22
6	20	19	<u>45</u>	<u>37</u>	<u>65</u>	<u>-0.55</u>
			50	44	66	-0.41
		Means	±6	±7	±3	±0.13

APPENDIX M

Maximum Likelihood Techniques
of Statistical Analysis

If data pairs x_i, y_i $i = 1, \ldots, n$ are assumed to obey a relation

$$y = mx + c, \qquad\qquad (M.1)$$

optimal values of m and c can be determined by maximum likelihood techniques as described by Kendall and Stuart (1967, chapter 29). In the illustrative problem of fitting a straight line of the form of (M.1) this is achieved by minimising the sum of squares of the perpendicular drops from the observed data points to the line; this being true if the observed quantities have equal associated error distributions.

In this case the solutions are

$$m = \frac{-b + \sqrt{b^2 + 4}}{2} \qquad \text{where}$$

$$b = \frac{n\Sigma y^2 - n\Sigma x^2 - (\Sigma y)^2 + (\Sigma x)^2}{\Sigma x \Sigma y - n\Sigma xy}$$

and $c = \frac{1}{n}(\Sigma y - m\Sigma x).$

If c is predetermined or forced,

$$b = \frac{\Sigma y^2 - \Sigma x^2 + nc^2 - 2c\Sigma y}{c\Sigma X - \Sigma xy}$$

and m is as above.

In all cases the sum of squares of these perpendicular drops is

$$S^2 = \frac{\Sigma y^2 - 2m\Sigma xy - 2c\Sigma y + m^2 \Sigma x^2 + 2cm\Sigma x + nc^2}{1 + m^2}$$

and the rms deviation is $S/\sqrt{n}$.

In the more general case of the observed quantities having error distributions with variances λ_x, λ_y then, in the line fitting illustration, the distances to be minimised are no longer the perpendicular drops, but will have a direction specified by the ratio of the error variances λ_y/λ_x. The case $\lambda_x = 0$ is seen to identify with the 'least squares' approach, where all the error is assumed to lie in y, and the 'vertical' drops are the ones involved in the minimisation.

Transforming the data

$$x_i \rightarrow x_i/\sqrt{\lambda_x}$$

$$y_i \rightarrow y_i/\sqrt{\lambda_y}$$

gives the new variables equal error variances and the formulae above can be applied.

Of particular interest in Ch. 5 here is the evaluation of the error on m. In the case of c being forced equal to zero,

$$(\Delta m)^2 = \left(\frac{\partial m}{\partial b}\right)^2 (\Delta b)^2$$

$$= \frac{m^2}{1+m^2} (\Delta b)^2 \quad , \text{ where}$$

$$(\Delta b)^2 = \Sigma\left(\frac{\partial b}{\partial x}\right)^2 (\Delta x)^2 + \Sigma\left(\frac{\partial b}{\partial y}\right)^2 (\Delta y)^2$$

$$= [4(\Sigma xy)^2(\Sigma x^2 + \Sigma y^2) + (\Sigma x^2)^3 + (\Sigma y^2)^3 -$$

$$\Sigma x^2(\Sigma y^2)^2 - \Sigma y^2(\Sigma x^2)^2] \; \Delta^2/(\Sigma xy)^4$$

if $\Delta x = \Delta y = \Delta$

REFERENCES

Anthony-Twarog, B.J. and Demarque, P., 1977. *Astr. and Ap. 57*, 471.

Arp, H.C., 1955. *A.J. 60*, 317.

Arp, H.C., 1956. *A.J. 61*, 15.

Arp, H.C. and Bruekel, F., 1973. *Ap. J. 179*, 445.

Arp, H.C. and Kraft, R.P., 1961. *Ap. J. 133*, 420.

Baade, W. and Arp, H.C., 1964. *Ap. J. 139*, 1027.

Baade, W. and Swope, H., 1963. *A.J. 68*, 435.

Balick, B. and Sneden, C., 1976. *Ap. J. 208*, 336.

Barry, D.C., 1974. *A.J. 79*, 616.

Bertiau, F.C., 1958. *Ap. J. 128*, 533.

Blaauw, A., 1963. "Basic Astronomical Data" (S & SSIII) p. 383 (Univ. of Chicago Press).

Boeshaar, G.O. and Hodge, P.W., 1977. *Ap. J. 213*, 361.

Bottinelli, L. and Gouguenheim, L., 1976. *Astr. and Ap., 51*, 275.

Boulesteix, J., Courtes, G., Laval, A., Monnet, G. and Petit, H., 1974. *Astr. & Ap., 37*, 33.

Brand, P.W.J.L. and Zealey, W.J., 1975. *Astr. and Ap., 38*, 363.

Brand, P.W.J.L., Zealey, W.J. and Coulson, I.M., 1980. Submitted.

Brandt, J.C., Roosen, R.G., Thompson, J. and Ludden, D.J., 1976. *Ap. J., 208*, 109.

Buscombe, W. and de Vaucouleurs, G., 1955. *Observatory, 75*, 170.

Campbell, C.T., Rodgers, A.W. and Whiteoak, J.B., 1960.
  M.N.R.A.S., *121*, 103.

Churchwell, E., 1975. See Wilson and Downes 1975, p. 245.

Clube, S.V.M., 1974. *Observatory*, *94*, 126.

Clube, S.V.M. and Dawe, J.A., 1980a. *M.N.R.A.S.*, *190*,
  575.

Clube, S.V.M. and Dawe, J.A., 1980b. *M.N.R.A.S.*, *190*,
  591.

Clube, S.V.M. and Jones, D.H.P., 1971. *M.N.R.A.S.*, *151*,
  231.

Conti, P.S., 1975. See Wilson and Downes 1975, p. 207.

Corbin, T.E., Smith, D.L. and Carpenter, M.S., 1975.
  B.A.A.S., *7*, 337.

Courtès, G. and Cruvellier, P., 1965. *Ann. d'Ap.* *28*,
  683.

Cunningham, A.A., 1968. *Ap. J.* *151*, 945.

Dainty, J.C., 1975. "Laser Speckle and Related Phenomena",
  ed. J.C. Dainty. Springer-Verlag. Berlin.

Davies, R.D., Elliot, K.H. and Meaburn, J., 1976. *Mem.
  R.A.S. 81*, 89.

Deharveng, L., 1974. *Astr. & Ap. 35*, 63.

De Vaucouleurs, G., 1976. *I.A.U. Colloq. 37*, 69.

De Vaucouleurs, G., 1977. "Systematic Errors....",
  preprint of Univ. of Texas/McD. Obs.

De Vaucouleurs, G., 1978a, *Ap. J. 223*, 351.

De Vaucouleurs, G., 1978b, *Ap. J. 223*, 730.

De Vaucouleurs, G., 1978c, *Ap. J. 224*, 14.

De Vaucouleurs, G., 1978d, *Ap. J. 224*, 710.

De Vaucouleurs, G., 1979a. *Ap. J.*, *227*, 380.

De Vaucouleurs, G., 1979c. *Ap. J.*, *84*, 1270.

De Vaucouleurs, G., 1979d. *I.A.U. Symp. 84*, 203.

Dufour, R.J., Talbot, R.J., Jensen, E.B. and Shield, G.A.,
  1980. *Ap. J.*, *236*, 119.

Garrison, R.F. and Walborn, N.R., 1974. *J.R.A.S. Can.*
  68, 117.

Gascoigne, S.C.B., 1969. *M.N.R.A.S. 146*, 1.

Gascoigne, S.C.B. and Kron, G.E., 1965. *M.N.R.A.S. 130*,
  333.

Georgelin, Y.P., 1971. *Astr. & Ap. 11*, 414.

Georgelin, Y.P. and Georgelin, Y.M., 1970a. *Astr. &*
  Ap. Suppl. 3, 1.

Georgelin, Y.P. and Georgelin, Y.M., 1970b. *Astr. & Ap.*
  6, 349.

Georgelin, Y.P. and Georgelin, Y.M., 1976. *Astr. & Ap.*
  49, 57.

Georgelin, Y.P., Georgelin, Y.M. and Sivan, J.-P., 1979.
  I.A.U. Symp. 84, 65.

Grubb Parsons Ltd., 1977. Document OL 121 589/77.

Gum, C.S., 1955. *Mem. R.A.S. 67*, 155.

Gum, C.S. and de Vaucouleurs, G., 1953. *Observatory,*
  73, 152.

Hanson, R.B., 1975. *A.J. 80*, 379.

Hawley, S.A., 1978. *Ap. J. 224*, 417.

Henize, K.G., 1956. *Ap. J. Suppl. 2*, 315.

Hertzsprung, E., 1913. *A.N. 196*, 201.

Hiltner, W.A., Morgan, W.W. and Neff, J.S., 1964. *Ap. J.*
  141, 183.

Hodge, P.W., 1969c. *Ap. J. Suppl. 18*, 73.

Hodge, P.W., 1976a. *R.G.O. Bull No. 82*, p. 169.

Hodge, P.W., 1976b. *Ap. J. 205*, 728.

Hodge, P.W., 1977. *Ap. J. Suppl. 33*, 69.

Hodge, P.W. and Wallerstein, G., 1966. *P.A.S.P. 78*, 411.

Holmberg, E., 1964. *Ark. Astr. 3*, 387.

Hubble, E., 1929a. Mt. Wilson Comm. No. 105 (*Proc. Nat. Acad. Sci. 15*, 168).

Hubble, E., 1929b. *Ap. J. 69*, 103.

Hubble, E., 1932. *Ap. J. 76*, 106.

Hubble, E., 1936. "The Realm of the Nebula", Oxford Univ. Press, London.

Humason, M.L., Mayall, N.V. and Sandage, A.R., 1956. *A.J. 61*, 97.

Humphreys, R.M. and Davidson, K., 1979. *Ap. J. 232*, 409.

Jaakkola, T. and Le Denmat, G., 1975. *M.N.R.A.S. 176*, 307.

Johnson, H.L., Hoag, A.A., Iriarte, B., Mitchell, R.I. and Hallam, K.L., 1961. *Lowell Obs. Bull. 5*, 133.

Kafatos, M., 1976. *B.A.A.S. 8*, 542.

Kayser, S.E., 1967. *A.J. 72*, 134.

Kendall, M.G. and Stuart, A., 1967. "The Advanced Theory of Statistics" Vol. 2, 2nd ed. Griffin and Co. Ltd., London.

Kennicutt, R.C., 1979a. *Ap. J. 228*, 394.

Kennicutt, R.C., 1979b. *Ap. J. 228*, 696.

Kennicutt, R.C., 1979c. *Ap. J. 228*, 704.

Kennicutt, R.C., Balick, B. and Heckman, T. , 1980.

    P.A.S.P. 92, 134.

Kodak 1973. "Plates and Films" (P-315).

Kukarkin, B.V., 1975. *I.A.U. Symp. 67*, p. 511.

Leavitt, H.S., 1908. *H.A. 60*, 87.

Leavitt, H.S., 1912. *Harvard Obs. Circ. 173*.

Lemke, D., 1975. See Wilson and Downes 1975, p. 372.

Lequeux, J., 1979. *Astr. & Ap. 80*, 35.

Lucke, P.B., 1974. *Ap. J. Suppl. 28*, 73.

Lucke, P.B. and Hodge, P.W., 1970. *A.J. 75*, 171.

Madore, B.F., 1976. *M.N.R.A.S., 177*, 157.

Marsalakova, P., 174. *Ap. & Sp. Sci. 27*, 3.

Martin, W.L., Warren, P.R. and Feast, M.W., 1979.

    M.N.R.A.S. 188, 139.

McLaughlin, D.B., 1945. *P.A.S.P. 57*, 69.

Meaburn, J., 1969. *Ap. & Sp. Sci. 3*, 600.

Meaburn, J., 1979. *Astr. & Ap. 75*, 127.

Melnick, J., 1977. *Ap. J. 213*, 15.

Melnick, J., 1978. *Astr. & Ap. 70*, 157.

Melnick, J., 1979. *Ap. J. 228*, 112.

Menon, T.K., 1964. *Proc. XII Gen. Ass. I.A.U. Hamburg*,

    p. 455.

Mezger, P.G., 1970. *I.A.U. Symp. 38*, p. 107.

Mineur, H., 1944. *Ann. d'Ap. 7*, 160.

Monnet, G., 1971. *Astr. & Ap. 12*, 379.

Murdin, P.G. and Sharpless, S., 1968. See Terzian

    1968a, p. 249.

Murray, C.A. and Harvey, G.M., 1976. *R.G.O. Bull. No.*

    182, p. 15.

Osterbrock, D.E., 1974. "Astrophysics of Gaseous Nebulae".
    W.H. Freeman and Co., San Francisco.

Pagel, B.E.J., Edmunds, M.G., Blackwell, D.E., Chun, M.S.
    and Smith, G., 1979. *M.N.R.A.S.*, *189*, 95.

Pagel, B.E.J., Edmunds, M.G., Fosbury, R.A.E. and Webster,
    B.L., 1978. *M.N.R.A.S. 184*, 569.

Peimbert, M., 1966. *Ap. J.*, *145*, 75.

Pel, J.W., 1980. *NASA Tech. Memo. 80625* ("Current Prob-
    lems in Stellar Pulsation Instabilities"), p. 1.

Pellet, A., Astier, N., Viale, A., Courtès, G., Maucherat,
    A., Monnet, G. and Simien, F., 1978. *Astr. & Ap.
    Suppl. 31*, 439.

Perrenod, S.C., Shields, G.A. and Chaisson, E.J., 1977.
    Ap. J. 216, 427.

Pratt, N.M., 1977. *Vistas in Astr. 21*, 1.

Reynolds, R.J., 1976a, *Ap. J. 203*, 151.

Reynolds, R.J., 1976b, *Ap. J. 206*, 679.

Robinson, L.B. and Wampler, E.J., 1972. *P.A.S.P. 84*, 161.

Rosino, L., 1964. *Ann. d'Ap. 27*, 498.

Rosino, L., 1973. *Astr. & Ap. Suppl. 9*, 347.

Sandage, A.R., 1962. *I.A.U. Symp. 15*, p. 359.

Sandage, A.R., 1970. *Ap. J. 162*, 841.

Sandage, A.R., 1972. *Q.J.R.A.S.*, *13*, 202.

Sandage, A.R., 1975, see Sandage *et al.*, 1975, p. 24.

Sandage, A.R., Sandage, M. and Kristian, J., 1975.
    "Galaxies and the Universe" *(S. & S.S.IX)*, Univ.
    of Chicago Press.

Sandage, A.R. and Tammann, G.A., 1968. *Ap. J. 151*, 531.

Sandage, A.R. and Tammann, G.A., 1971. *Ap. J. 167*, 293.

Sandage, A.R. and Tammann, G.A., 1974a. *Ap. J. 190*, 525, *(S. & T. I)*.

Sandage, A.R. and Tammann, G.A., 1974b. *Ap. J. 191*, 603, *(S. & T. II)*.

Sandage, A.R. and Tammann, G.A., 1974c. *Ap. J. 194*, 223, *(S. & T. III)*.

Sandage, A.R. and Tammann, G.A., 1974d. *Ap. J., 195*, 559, *(S. & T. IV)*.

Sandage, A.R. and Tammann, G.A., 1975a. *Ap. J. 196*, 313, *(S. & T. V)*.

Sandage, A.R. and Tammann, G.A., 1975b. *Ap. J. 197*, 265, *(S. & T. VI)*.

Sandage, A.R. and Tammann, G.A., 1976b. *Ap. J. 210*, 7, *(S. & T. VII)*.

Sandage, A.R. and Wallerstein, G., 1960. *Ap. J. 131*, 598.

Sarazin, C.L., 1977. *Ap. J. 211*, 772.

Schmidt-Kaler, Th., 1977. *Astr. & Ap. 54*, 771.

Searle, L., 1971. *Ap. J. 168*, 327.

Sérsic, J.L., 1959. *Observatory, 79*, 54.

Sérsic, J.L., 1960. *Zs. f. Ap. 50*, 168.

Sérsic, J.L., 1979. Cordoba preprint "The HII Regions as Distance Indicators".

Sharpless, S., 1959. *Ap. J. Suppl. 4*, 257.

Shields, G.A. and Searle, L., 1978. *Ap. J. 222*, 82I.

Smith, H.E., 1975. *Ap. J. 199*, 591.

Talbot, R.J., Jensen, E.B. and Dufour, R.J., 1980. *Sky and Telescope 60*, 23.

Talbot, R.J., Jensen, E.B. and Shields, G.A., 1979. *Ap. J. 229*, 91.

Tammann, G.A. and Sandage, A.R., 1968. *Ap. J. 151*, 825.

Terzian, Y., 1968a. "Interstellar Ionized Hydrogen", W.A. Benjamin Inc. N.Y.

Terzian, Y., 1968b. See Terzian 1968a, p. 283.

Van Altena, W.F., 1974. *P.A.S.P. 86*, 217.

Van Bueren, H.G., 1952. *B.A.N. 11*, 385.

Van den Bergh, S., 1960a. *Pub. D.D.O. 2*, 159.

Van den Bergh, S., 1960b. *Ap. J. 131*, 215.

Van den Bergh, S., 1964. *Ap. J. Suppl. 9*, 65.

Van den Bergh, S., 1975a. See Sandage *et al.*, 1975, p. 507.

Van den Bergh, S., 1975b. "Structure and Evolution of Galaxies". NATO Advanced Study Institutes Series. ed. G. Setti. D. Reidel Publ. Co. Dordrecht, Holland. p. 247.

Van den Bergh, S., 1977. *I.A.U. Colloq. No. 37*, p. 13.

Van den Bergh, S., 1980. *Ap. J. 235*, 1.

Van Herk, G., 1965. *B.A.N. 18*, 71.

Véron, P. and Sauvayre, A., 1965. *Ann. d'Ap. 28*, 698.

Walborn, N.R., 1978. *I.AU. Symp. No. 80*, p. 5.

Walker, M.F., 1961. *Ap. J. 133*, 438.

Waymann, P.A., Symms, L.S.T. and Blackwell, K.C., 1965. *Roy.-Obs. Bull. No. 98*.

Wilson, T.L., 1975. See Wilson and Downes 1975, p. 424.

Wilson, T.L. and Downes, D., 1975. "HII Regions and Related Topics". Springer-Verlag, Berlin.

Woolley, R., Harding, G.A., Cassells, A.I. and Saunders J., 1965. *Roy. Obs. Bull. No. 97*.